Titanium Dioxide Nanomaterials for Photovoltaic Applications

Yu Bai,[†,‡] Iván Mora-Seró,[§] Filippo De Angelis,[‖] Juan Bisquert,[§] and Peng Wang*,[†]

[†]State Key Laboratory of Polymer Physics and Chemistry, Changchun Institute of Applied Chemistry, Chinese Academy of Sciences, Changchun 130022, China

[‡]Institute of Chemistry and Energy Material Innovation, Academy of Fundamental Interdisciplinary Sciences, Harbin Institute of Technology, Harbin 150080, China

[§]Photovoltaic and Optoelectronic Devices Group, Departament de Física, Universitat Jaume I, 12071 Castelló, Spain

[‖]Istituto CNR di Scienze e Tecnologie Molecolari, c/o Dipartimento di Chimica, Università di Perugia, via Elce di Sotto 8, I-06123 Perugia, Italy

CONTENTS

1. INTRODUCTION: PROPERTIES OF TIO₂ NANOMATERIALS

The continuous increase of the world's population, together with the substantial development of industry has brought about imperious demand for larger energy consumption. At present, most of the energy production is made from the combustion of fuels, such as oil, natural gas, and coal. However, the depletion of fossil resources, the commensurate increase in noxious gas emissions, and the other associated environmental pollutions have put forward an urgent demand for developing sustainable energy technologies. Among all of the renewable energy technologies, including hydro, solar, wind, geothermal heat, and biomass, photovoltaic (PV) technology which converts solar energy into electricity is expected to be the most promising strategy for sustainable energy supply. Solar photovoltaics is now, regarded as the third most important renewable energy source in terms of globally installed capacity and by the end of 2012 the world's cumulative solar PV capacity has passed the 100 GW milestone.

So far, the solid-state junction devices based on silicon material have dominated PV solar energy converters. However, the light-induced degradation of silicon materials limits the device stability while the relatively high cost of PV electricity production hinders its effective competition with fossil energy. One attractive alternative to crystalline silicon PV devices is cells made from mesoscopic inorganic semiconductors, which can be easily prepared and offer the prospect of very low cost fabrication. In these devices, the inorganic semiconductors mainly function as electron acceptor and provide direct or tortuous path for electron transport while in some cases they may also act as the scaffold for the adsorption of light harvesters. Of the many semiconductor metal oxides, TiO₂ nanomaterial appears to be a distinguishing candidate because of its high chemical and optical stability, nontoxicity, low cost, and corrosion resistance. There are four commonly known

polymorphs of TiO_2 found in nature, i.e., anatase (tetragonal), rutile (tetragonal), brookite (orthorhombic), and TiO_2 (B) (monoclinic).[1,2] Besides, two additional high-pressure forms have been synthesized from the rutile phase including TiO_2 (II) with a PbO_2 structure[3] and TiO_2 (H) with a hollandite structure.[4] Rutile TiO_2 has a tetragonal crystal structure and contains six atoms per unit cell as shown in Figure 1.[5] Rutile is
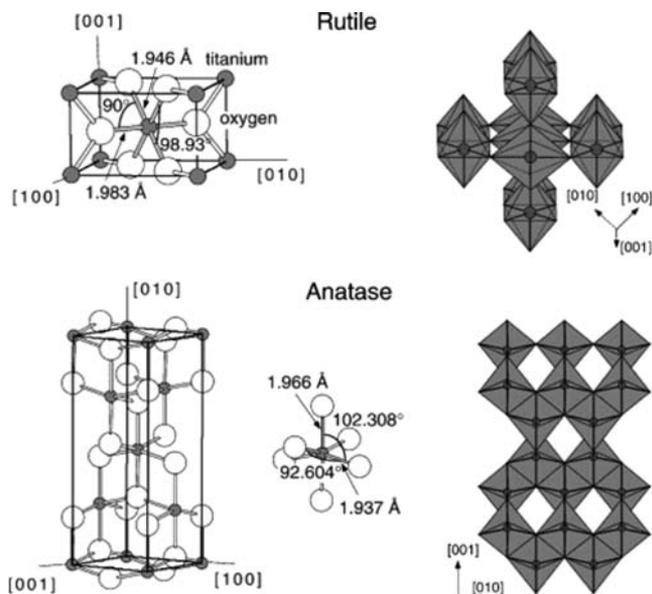
Figure 1. Representations of the TiO_2 anatase and rutile forms. Reprinted with permission from ref 5. Copyright 2003 Elsevier.

the most thermodynamically stable polymorph of TiO_2 at all temperatures, exhibiting lower total free energy than metastable phases of anatase and brookite. Anatase TiO_2 has a crystalline structure that corresponds to the tetragonal system but the distortion of the TiO_6 octahedron is slightly larger for the anatase phase. The anatase structure is preferred over other polymorphs for solar cell applications because of its potentially higher conduction band edge energy and lower recombination rate of electron−hole pairs.[6]

The physical and chemical properties of TiO_2 nanocrystals are affected not only by the intrinsic electronic structure, but also by their size, shape, organization, and surface properties. Interesting morphologies and properties have recently attracted considerable attention and many nanostructured TiO_2 materials, such as nanotubes, nanorods, nanofibers, nanosheets, and interconnected architectures, have been fabricated and applied in PV devices. Generally, it is crucial to maximize the specific surface area of TiO_2 so as to facilitate the reaction at the interface between TiO_2 and the interacting media. Besides large surface area, the TiO_2 nanomaterials should also feature high electron mobility so that electrons injected in the TiO_2 can be collected effectively. As defects in the TiO_2 nanomaterials may act as electron traps and exist in grain boundaries at the contacts between nanosize particles, the use of a network structure consisting of TiO_2 single-crystal-like nanowires instead of TiO_2 nanoparticles is expected to induce a great improvement for rapid electron transportation. However, such proposition is not proven yet and the nanoparticulate TiO_2 continues to provide optimal results in PV devices, despite the presence of disorder. Besides, the properties of TiO_2 also strongly relay on the modifications of the TiO_2 material host

(e.g., organic molecules, ions, and inorganic materials) and on the interactions of TiO_2 materials with the environment. The surface modification not only affects the interfacial energy offset but also has significant impact on the charge separation, transport, and recombination processes. In recent years, the ever increasing growth of research activities in nanoscience and nanotechnology continually brings on new physical and chemical properties of TiO_2 nanomaterials and provides new opportunities for the development of TiO_2-based solar cells. We believe that a new and comprehensive review of TiO_2 nanomaterials for PV application would promote further research of PV field and develop efforts to tackle the ever increasing global energy challenge.

For the present paper, we aim to offer a brief review on the application of titanium dioxide nanomaterials in photovoltaic devices, including dye-sensitized solar cells, polymer-inorganic hybrid solar cells, quantum dot-sensitized solar cells, inorganic solid-state solar cells and perovskite solar cells. In each section, a short introduction is given, including the configuration and the working principle of the solar cell. Besides addressing the benefits of using nanostructured TiO_2 materials, more emphasis is given to the modulation of properties and the charge transfer kinetics at the TiO_2 interface in these devices. We summarize the important findings and select examples representing recent research progress and hope that this writing will provide reader comprehensive overview of the application of titanium dioxide nanomaterials in renewable energy technology research.

2. APPLICATION IN DYE-SENSITIZED SOLAR CELLS (DSCS)

2.1. Fundamentals of DSCs

One important application of TiO_2 nanomaterials in PV fields is DSCs. Photoelectrochemical solar cells based on sensitized metal oxides were initially studied by Gerischer and co-workers.[7] In 1991, O'Regan and Grätzel[8] reported the first breakthrough by taking advantage of the large surface area within a mesoporous TiO_2 film, and at present the power conversion efficiency (PCE) of up to 12.3% has been achieved based on a liquid cobalt(II/III)-based electrolyte and a porphyrin sensitizer.[9] At the heart of the device is the mesoporous metal oxide layer composed of a network of TiO_2 nanoparticles (NPs) which have been sintered together to establish electronic conduction. This mesoporous titania architecture has been proved to provide a 100-fold enhancement in surface area per micrometer thickness when compared with a flat film, thus providing larger accessible surface area for sensitizer adsorption. A schematic representation of the DSC is shown in Figure 2. Photoexcitation of the dye molecule leads to
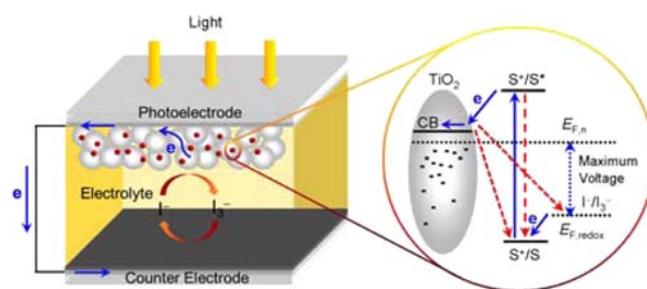
Figure 2. Operating principle and energy level scheme of dye-sensitized solar cells.

B

dx.doi.org/10.1021/cr400606n | *Chem. Rev.* XXXX, XXX, XXX−XXX
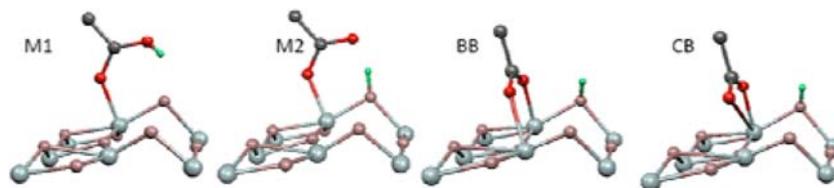
Figure 3. Schematic representation of monodentate (M1), dissociative monodentate (M2), bridged bidentate (BB), and bridged chelated (CB) adsorption modes for a carboxylic acid on the (101) TiO$_2$ surface. Reprinted with permission from ref 22. Copyright 2012 Royal Society of Chemistry.

electron transfer from the dye's excited state into the conduction band (CB) of the TiO$_2$, leaving the dye in its oxidized state.[10−13] Electrons injected in the TiO$_2$ are collected at the conducting glass surface through transport across the disordered network of TiO$_2$ NPs. The oxidized dye is regenerated by electron donation (usually iodide ions, I$^-$) in the electrolyte that is infiltrated into the porous films and the generated triiodide ions (I$_3^-$) are reduced at the counter electrode. In addition to these forward electron transfer and transport processes, there are also several competing loss pathways, including the excited-state decay of dye molecules, charge recombination of injected electrons with dye cations and with oxidative species in the electrolyte.

In DSCs, the working process can be regarded as a competition of these forward and loss pathways. Besides the physical and chemical properties of TiO$_2$ nanocrystal itself, the interaction of TiO$_2$ with surrounding environment such as sensitizers and electrolytes also has significantly impact on the TiO$_2$/dye/electrolyte interfacial properties, charge transfer kinetics, and thus the PV performance. In recent years, extensive efforts have been taken to investigate the interfacial interactions and the correlated charge transfer processes. These researches give people intrinsic understanding of the charge transfer in DSCs and provide clues for further improving device performance by interfacial engineering.

2.2. Interaction of Sensitizers with TiO$_2$

Dye-TiO$_2$ interactions rule the primary charge generation event in DSCs, i.e. electron injection from the dye excited state into the CB of the TiO$_2$, and thus exert a direct influence on the short-circuit photocurrent density (J_{sc}). The opposite process, i.e., the parasitic recombination between injected electrons and oxidized dyes, which occurs after the electron injection, is also entirely dependent upon the dye−TiO$_2$ interactions. This process may affect the J_{sc} and, by reducing the electron density in the TiO$_2$, the open-circuit voltage (V_{oc}). Dye−TiO$_2$ interactions also lead to shifts in the energy of the TiO$_2$ CB, thus directly affecting the V_{oc} as well as indirectly influencing the kinetics of electron injection and recombination by shifting the semiconductor CB energy levels.

The formation of a compact dye monolayer on the TiO$_2$ surface can insulate the TiO$_2$ surface from approach of the electrolyte and suppress the recombination between injected electrons and oxidized species in the electrolyte. As the dye may also constitute a binding site for oxidized species in the electrolyte, the location of these binding sites and the dye adsorption mode further shed light into reasons of the vastly different efficiencies for very similar dyes. As such, an understanding of dye−TiO$_2$ interactions from an in-depth and atomistic perspective is important to the full exploitation and optimization of DSCs.

The primary dye−TiO$_2$ interactions are mediated by the dye adsorption mode on the semiconductor surface. A crucial characteristic for efficient dyes is the presence of suitable functional groups which can strongly bind to the surface of semiconducting metal oxides. To ensure ultrafast electron injection, the anchoring group should coincide or be very close (conjugated) to the dye acceptor unit, where the photoexcited electrons are spatially confined. This promotes electronic coupling between the donor levels of the excited dye and the delocalized acceptor levels of the semiconductor CB, assisting the charge injection process.[14] The orientation and packing of adsorbed dyes on the semiconductor surface are strictly dependent upon the binding motif and affect the rate and effectiveness of parasitic recombination reactions.[15,16] Moreover, the sensitizer's anchoring group should provide stable grafting of the dye onto the semiconductor surface, thus leading to long-term device stability.[17−19] The main information available on dye anchoring on the TiO$_2$ surface is reviewed in section 2.2.1, while the implications of dye−TiO$_2$ interactions on the DSCs operational mechanism are reviewed in section 2.2.2.

2.2.1. Anchoring of Sensitizers on TiO$_2$ Surface. The anchoring mechanism of the largely employed carboxylic acid group to the TiO$_2$ surface can be exemplified referring to the coordination modes of the carboxylate fragment (COO$^-$) to metal ions. There are basically three typical coordination schemes, including monodentate chelating, bidentate chelating, and bidentate bridging.[20] An empirical rule, derived by Deacon and Philips,[21] correlates the difference between the asymmetric and symmetric IR stretching frequencies ($\Delta\nu_{as}$) of COO$^-$ to the type of coordination: if $\Delta\nu_{as}$ for the adsorbed species is larger than that measured for the neat salt a monodentate coordination (either M1 or M2 in Figure 3) is hypothesized;[22] if $\Delta\nu_{as}$ is comparable or smaller than that of the corresponding salt, a bidentate (either bridged bidentate BB or chelating bidentate CB in Figure 3) bonding mode is hypothesized. Thus, the disappearance of the carbonyl stretching of the free dye and the appearance of the carboxylate symmetric and asymmetric stretching in the 1300−1650 cm^{-1} region, are a diagnostic for dye adsorption mode. However, realistic dyes often show a plethora of overlapping absorptions in the interesting range, which may hinder a precise identification and/or assignment of the diagnostic carboxylic modes. Most IR spectral assignments for dyes on TiO$_2$ are thus based on the comparison between experimental data and DFT-calculated IR spectra. These techniques give structural details about the adsorption modes and provide information on the relative orientation of the molecules anchored onto the oxide surface.

The binding mode of the prototypical [Ru(NCS)$_2$(dcbpy)$_2$] dye (known as N3) on TiO$_2$ was investigated by Shklover et al.[23] Based on structural analyses, various dye adsorption modes were modeled and corresponding surface area occupations were

C

estimated. It was concluded that binding via two or three carboxylic groups would be favored over a single anchoring, while binding via four carboxylic groups was impeded by planarity of the TiO$_2$ surface. The adsorption mode of the doubly protonated N3 dye (also known as N719) was further investigated by DFT calculation by De Angelis et al.,[24] while the electronic properties of the N3/TiO$_2$ interface were previously investigated at the DFT level by Persson et al.,[25] using a model geometry. Binding of the N719 dye on TiO$_2$ was found to occur in a dissociative fashion, involving carboxylic groups residing on different bipyridine ligands.[24] De Angelis et al.[26] performed ab initio molecular dynamics simulations and suggested that N719 adsorbed onto the TiO$_2$ surface via three anchoring carboxylic groups out of the four dye carboxylic groups (Figure 4). The simulation of the tetrabutyl ammonium
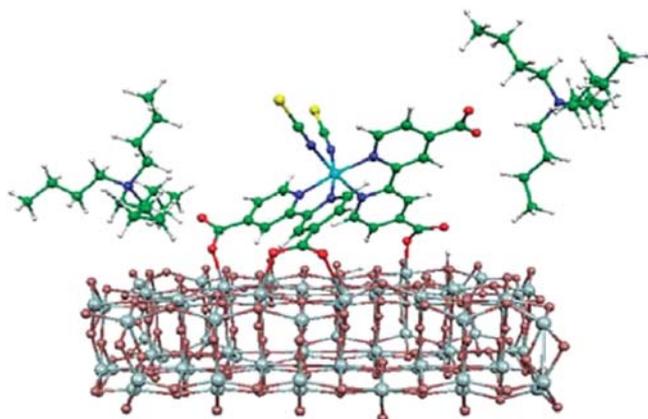
Figure 4. Optimized geometrical structure of the N719 dye adsorbed on TiO$_2$ along with its two TBA counterions. Reprinted with permission from ref 26. Copyright 2010 American Chemical Society.

(TBA) counterion position revealed one strongly bound TBA, which was close to the TiO$_2$ surface, and one loosely bound TBA, suggesting a partial negative charge for the N719-adsorbed dye.

The anchoring of the N3 dye as a function of protonation of the carboxylic groups was investigated by Schiffmann et al.[27] by combining IR experiments and DFT calculations. It was demonstrated that the dye binding mode on TiO$_2$ can be significantly affected by the initial dye protonation. When four protons was considered in the system, the most stable adsorption mode was calculated to occur via three anchoring carboxylic groups (G in Figure 5a), in agreement with the three anchoring adsorption mode proposed in ref 26. When no protons were considered, the most stable adsorption mode was shown to correspond to binding via two carboxylic groups residing on different bipyridine ligands (I$_2$ in Figure 5a), closely resembling the one previously suggested in ref 24.

Despite the calculated dye adsorption energetics, Schiffmann et al.[27] suggested that solvent molecules could displace one carboxylic group, favoring two-anchoring modes. This is also supported by the similarity between the DFT-calculated IR spectrum of N3 adsorbed on mesoporous TiO$_2$ and the experimental one (Figure 5b). Labat et al.[28] also found that N3 dye binded to TiO$_2$ surface via two carboxylic groups residing on different bipyridine ligands although they did not consider three anchoring structures. Martsinovich et al.[29] investigated the N3 dye adsorption on the rutile (110) surface rather than on the anatase (101) surface as from previous studies. On the
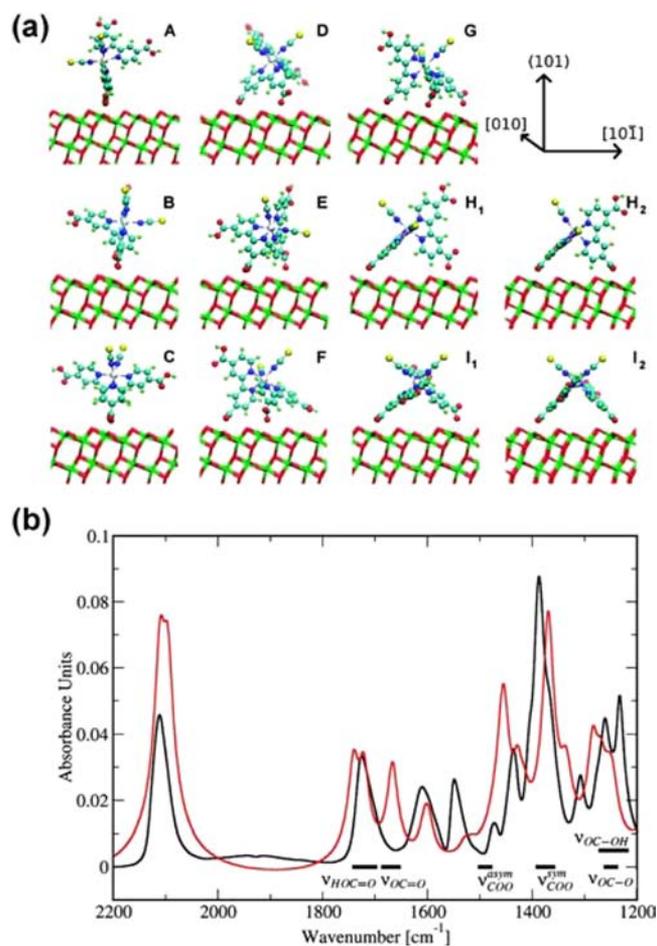
Figure 5. (a) Different possible orientations and coordination patterns of the stable 2-fold and 3-fold anchored dyes bound to the anatase (101) surface. (b) The experimental IR spectrum of the N3 dye adsorbed on anatase nanocrystals in EtOH (black) and the computed IR spectrum (red) for the fully protonated configuration I$_1$ on the anatase (101) surface. Reprinted with permission from ref 27. Copyright 2010 American Chemical Society.

basis of the calculated adsorption energies, it is impossible to identify a single adsorbed structure, while it seems that several configurations with similar stabilities may coexist or convert into one another.

The photoelectron spectroscopy (PES) can provide information on the molecular and electronic structures at the dye/TiO$_2$ interface, along with basic indications of the dye coverage and of the distance of selected atoms from the surface.[30−34] Also the measurement of the adsorbed dye monolayer depth compared to the molecular dimensions can give qualitative information about the angle formed by the main axis of the adsorbed dyes with respect to the TiO$_2$ surface. By measuring the ratio between the 1s peaks of the nitrogen atoms of the triphenylamine (TPA) donor and of the cyanoacrylic acid acceptor in typical push−pull organic dyes, Rensmo and co-workers[30] successfully estimated the relative distance of the dye atoms from the surface. As shown in Figure 6a, the N1s core level is originated by two signals separated by 1.3 eV, arising from the TPA nitrogen (399.8 eV) and the cyano group (CN) nitrogen (398.5 eV) atoms. The intensity ratio of the two signals measured at different photon energies is clearly suggestive of a dye orientation with the TPA moiety pointing away from the surface, while the CN group is close to the TiO$_2$
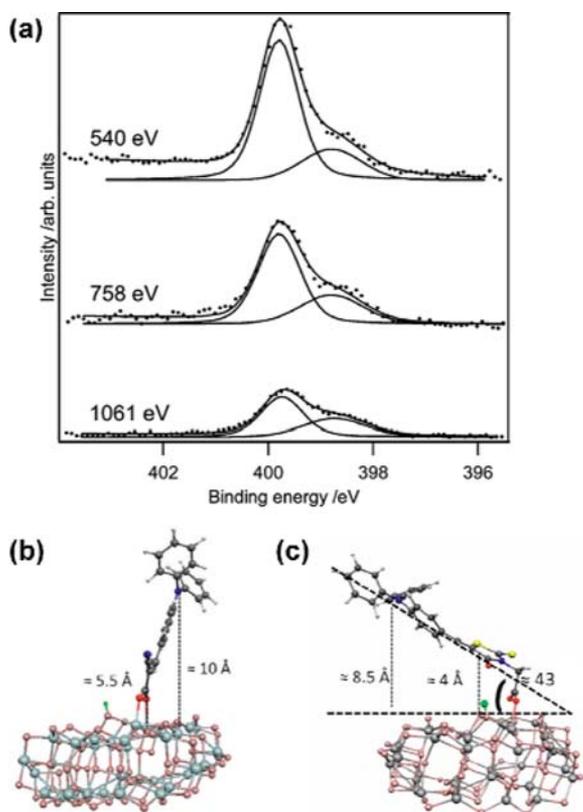
Figure 6. (a) N1s core level spectra of D5 adsorbed onto nanostructured TiO$_2$ measured at three different photon energies. Reprinted with permission from ref 30. Copyright 2010 American Chemical Society. (b) and (c) Optimized molecular structures of the more stable BB adsorption modes for the L0 and rh-L0 dyes. Reprinted with permission from ref 16. Copyright 2011 Royal Society of Chemistry.

surface. Pastore et al.[16] investigated the adsorption mode of two dyes (L0 and rh-L0) on TiO$_2$ as models of the systems having TPA donor groups and cyanoacrylic and rhodanine-3-acetic acid acceptor moieties. As illustrated in Figure 6b,c, structural optimization of the dye adsorbed on TiO$_2$ models revealed a preference for the bridged bidentate adsorption mode in both cases, although different binding modes were quite close in energy for the rh-L0 dye. The mostly employed cyanoacrylic acid anchoring group induces a perpendicular dye orientation with respect to the TiO$_2$ surface for the cyanoacrylic acid L0 dye, while the rh-L0 dye, bearing a rhodanine-3-acetic acid acceptor, forms an angle of ~40° with the average TiO$_2$ plane.

Besides, the techniques of X-ray reflectometry (XRR),[35] X-ray photoelectron spectroscopy (XPS),[36−39] and neutral impact collision ion scattering spectroscopy (NICISS)[40] are also applied to unravel the orientation, morphology, and thickness of dye molecules adsorbed on the titania surface. The implications of different dye adsorption modes on the photovoltaic performances are discussed in the next section.

2.2.2. Influence of Sensitizer Adsorption Behavior. Understanding the adsorption behavior of sensitizers on the TiO$_2$ surface, such as dye orientation and molecular packing is important for obtaining valuable insight into the charge transfer processes occurring in DSCs. In this section, we will shortly review the effect of dye interaction with TiO$_2$ in the fundamental operational DSC processes, i.e., electron injection from the dye excited state into the TiO$_2$ unoccupied states,

recombination between injected electrons and oxidized dye molecules, and recombination between injected electrons and oxidized species in the electrolyte. The effect of dye adsorption on the electronic properties of TiO$_2$ is also briefly reviewed.

A large number of theoretical investigations have been specifically devoted to the effect of the dye anchoring and spacer groups on determining the efficiency of the electron injection and the minimization of parasitic recombination processes.[16,41−52] The effect of the anchoring group on the electron injection dynamics in dye-sensitized semiconductor surfaces was pioneered by Persson and co-workers in a series of papers.[25,41−44] These researchers exploited the News-Andersson model framework to estimate the lifetime of an electron initially residing on the dye LUMO when it comes into contact with the manifold of unoccupied semiconductor states. The main finding of these studies is that a conjugated anchoring group, e.g., a perylene dye featuring a double bond connecting the donor and acceptor moieties, exhibits a much stronger interfacial coupling and a shorter electron injection time than the same system with a non conjugated anchoring group. These results are in excellent agreement with the time-resolved spectroscopic results by Szarko et al.,[53] who found a sizable dye-semiconductor coupling for the conjugated perylene dye, as signaled by the broader and partly unstructured steady-state absorption spectrum measured for the dye anchored to the semiconductor compared to the dye in solution.

An interesting contribution to the "anchoring group" issue came from the Troisi group,[52] who systematically investigated the electron injection time for different dyes. They set up a new computational strategy, which allows one to compute the injection time by simply investigating the TiO$_2$/anchoring group interface, without needing to compute the entire dye-semiconductor system. The authors investigated a series of possible anchoring groups (as shown in Figure 7) in
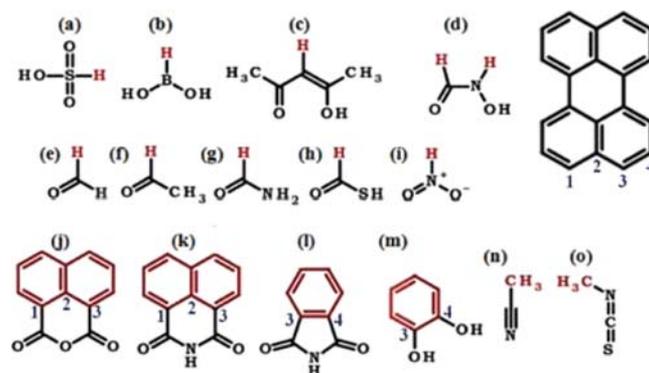
Figure 7. (a−o) Molecules with model anchoring groups studied in ref 48. Reprinted with permission from ref 52. Copyright 2012 American Chemical Society.

combination with a perylene donor moiety. The authors investigated the attachment chemistry and computed the binding energies of 15 different anchoring groups on both anatase (101) and rutile (110) surfaces. Based on periodic DFT calculations, most of the groups were found to have multiple stable adsorption modes, with a total of 35 adsorption modes on anatase (101) and 26 adsorption modes on rutile (110). For each anchoring group and observed adsorption geometry, the authors computed the electron injection time for a perylene molecule bearing the selected group on anatase (101) and rutile (110). Based on this data, various interesting alternatives to the

most common carboxylic or phosphonic acid anchoring are spotted out by this computational investigation, such as acetylacetone (c) and hydroxamic acid (d) anchors, which both display good computed binding and injection characteristics. For a given dye and/or anchoring group, it is also found that the dissociative bridged bidentate adsorption mode induces a higher interfacial coupling and a shorter electron injection times than the monodentate adsorption. For the N3 dye on the TiO$_2$ rutile (110) surface, Martsinovich et al.[29] found that the injection time significantly shortened for the bridged bidentate adsorption modes as well as by increasing the number of sensitizer carboxylic groups anchoring to TiO$_2$.

To discuss the impact of dye adsorption mode on the recombination reactions[54,55] it is worthwhile to recall that the kinetics of recombination between the injected electrons and the oxidized dye are strongly dependent upon the electron density in the conduction band/trap states, electrolyte composition[56–58] as well as the spatial separation of the charge hole localized on the oxidized dye, which can be assimilated to the HOMO of the neutral dye, and the TiO$_2$ surface.[59] Solely on the basis of the discussed results, that is of the different charge injection mechanisms, it is not straightforward to hypothesize a different location of the injected electrons as one should take into account the complex dynamics of the delocalization of the electrons into the oxide bulk as well as their relaxation pathways to the CB edge.[60] One can however speculate that for those dyes featuring weak electronic coupling with the semiconductor CB, such as for the rh-L0 dye in Figure 6c, the prevalence of a nonadiabatic electron injection mechanism implies an exponential dependence of the electron transfer rate upon the dye donor/semiconductor acceptor states; that is, the electronic coupling is determined by the tunneling probability, with the associated exponential decay. It can therefore be conceived that a high probability of electron injection would correspond to semiconductor CB states localized close to the dye LUMO, i.e. CB states localized at the semiconductor surface rather than within the bulk, from which a faster recombination with oxidized dyes can be expected. One can furthermore elaborate that the different orientation of the dyes with respect to the TiO$_2$ surface, determined by the possibly different anchoring unit, results in a different dye HOMO/TiO$_2$ CB separation even considering the same nature of the CB states involved in the electron injection for the L0 and rh-L0 dyes. Looking at the bidentate structures reported in Figure 6b,c, and considering the TPA donor unity, the dye HOMO/TiO$_2$ distance can be roughly estimated to be 8–10 Å for L0 and 6–8 Å for the rh-L0 dye. By extrapolating this data for the longer D5L2A1 and D5L2A3 dyes examined by Wiberg et al.,[15] a dye HOMO/TiO$_2$ separation of 14–16 and 9–11 Å for the two dyes is calculated respectively. This data might account for the measured differences in the recombination rates, whereby a closer proximity of the hole localized on the dye to the semiconductor surface would lead to higher recombination rates.[61] A similar argument, i.e., the different distance of the dye HOMO from the TiO$_2$ surface, was also exploited to explain the different recombination kinetics of the ruthenium C101 dye on TiO$_2$ anatase nanoparticles with preferential (101) and (001) facets.[62]

While the origins of the inhibited recombination dynamics can be rather complicated and are still not well understood, recent exploratory researches provide us some information on the association between the electron recombination kinetics and molecular assemblies on titania surface.[37–39,63–65] In most cases, the assemblies of sensitizers on titania surface are proposed to form a blocking layer, thus inhibiting the charge recombination and benefiting the V_{oc}. Wang and co-workers measured the thickness of dye assemblies on titania by employing the XPS technique and found that there was a positive correlation between the electron lifetime and molecular coating thickness.[37–39] The thicker molecular coating on titania induces longer tunneling distance between titania electrons and oxidative species and consequently offers longer electron lifetimes of the mesoporous titania film. XPS measurements reveal that the branched sensitizers are likely to form thicker coatings on titania surface, presumably because they tend to anchor on the surface of titania with a relatively smaller tilt angle with respect to the substrate normal.[37,38] These thick molecule coatings effectively hinder the leakage of electrons and make a decisive contribution to the improved photovoltage as well as the higher charge collection efficiency. Besides the thickness of dye coatings, the internal structure of self-assembling sensitizer layers is of crucial important to the charge transfer process in the device. The sensitizers with three-dimensional (3D) steric encumbrance are likely to form powerful porous photoactive layers on the surface of TiO$_2$ nanocrystals.[63,66] Although this kind of assemblies may exhibit thinner compact layer thickness, it can significantly hinder the charge recombination if the resultant micropores are smaller than the oxidative species in the electrolyte.[63]

Recently, two organic sensitizers (C257 and C258, as shown in Figure 8a) with cyclopentadithiophene-benzothiadiazole unite as the chromophoric core have been synthesized and applied in DSCs in conjunction with a cobalt electrolyte.[64] Solar cells based on C258 sensitizer exhibit relatively low incident photon-to-current efficiency (IPCE) height and V_{oc} as compared with the C257-based cell and this inferior photovoltaic performance is attributed to the fast charge recombination of photogenerated titania electrons with the oxidized dye molecules and/or Co(III)–bpy ions in the electrolyte. Contrary to the above-mentioned results, XPS measurement showed that there was not a positive correlation between the dye layer thickness and the electron lifetime (Figure 8b). This phenomenon was explained by the postulation that the C258 sensitizer formed an organic layer with more penetration channels (Figure 8c), allowing the Co(III)–bpy ions to penetrate and thus to be in proximity with the surface of titania. In the development of low energy gaps of organic dyes, it is quite common to meet the aggregation induced carrier photogeneration troubles. Good dye-bath solvent, in which the interactions between dye segments and solvent molecules are energetically favorable, can prevent the aggregation of dye molecules on the surface of titania,[38,39,67–69] thus improving the electron and hole injection yields in the device. However, the application of a good solvent also diminishes dye loading amount and brings forth some pinhole defects in the dye layer on the titania surface (Figure 9a). These defects may act as penetration channels for ions in the electrolyte, speeding up the interfacial charge recombination and deteriorating the photovoltaic performance of DSCs.

To obtain optimized molecular assemblies on titania surface, the molecules, which feature a high capacity of considerably slowing down the interfacial charge recombination, are used for pinhole defect filling (Figure 9a). Recently, three fillers have been tested by measuring the dark currents and it was found that filler III featured the strongest ability of controlling the interfacial charge recombination (Figure 9b,c).[66] The filler III
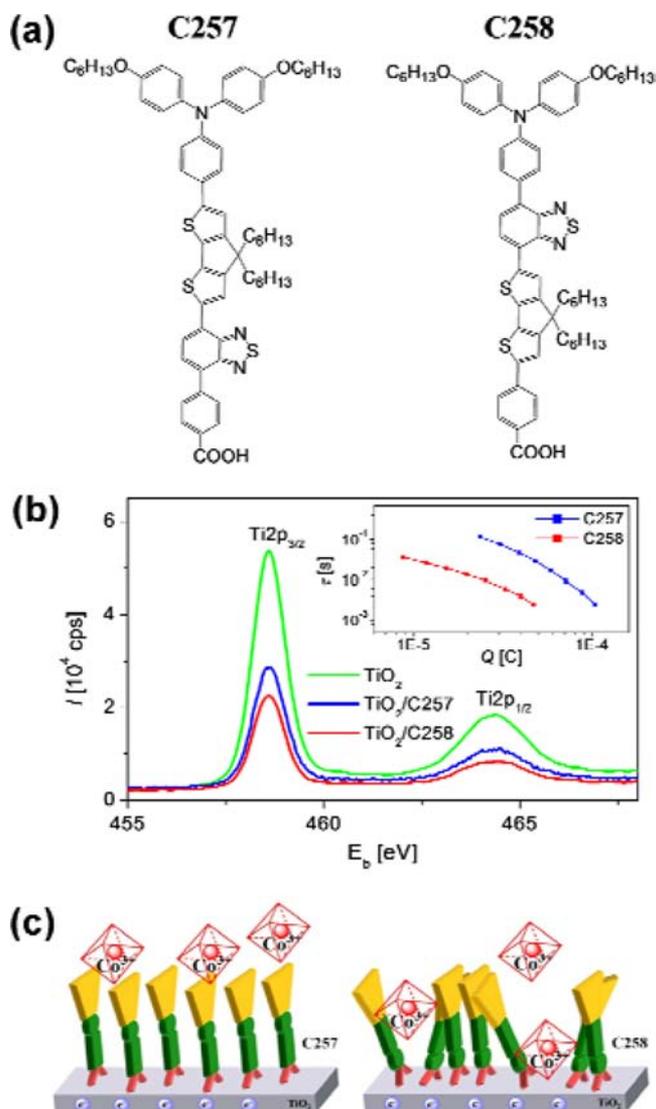
Figure 8. (a) Molecule structures of the C257 and C258 dyes. (b) Signal intensities of the Ti2p$_{3/2}$ and Ti2p$_{1/2}$ photoelectrons emitted from the bare and dye-grafted mesoporous titania films. The inset shows the electron lifetime for the C257 and C258 grafted titania films. (c) Schematic of the self-assembled dye layer of C257 and C258 on titania surface. Reprinted with permission from ref 64. Copyright 2013 Royal Society of Chemistry.

Figure 9. (a) Pictorial illustration for self-organized molecules on titania with dyes dissolved in a good solvent (upper) and pinhole defect filling with a suitable filler (bottom). (b) Molecular structures of three pinhole defect fillers. (c) J−V characteristics in the dark for cells employing the bare and grafted titania films with fillers I−III in combination with a Co−phen electrolyte. Reprinted with permission from ref 66. Copyright 2013 Royal Society of Chemistry.

grafted on the titania surface forms the molecule layer with the largest thickness and smallest mass density than the other two fillers, implying that the molecule with a bulkier 3D character tends to form a thicker coating layer with a larger porosity. The close relation between the filler layer thickness and the recombination hindering ability of fillers further confirms that the resulting porous but thick coating can strongly restrain the charge recombination through elongating the electron tunnelling distance. Taking advantage of the dark current controlling power, the filler III was cografted with C258 dye to remove the penetration channels for the Co(III)−bpy ions.[64] As shown in Figure 10, the device performance was greatly improved due to enhanced V_{oc} and J_{sc}, achieving an unprecedented PCE of 11.2% for DSCs with metal-free organic dyes under AM 1.5 full sunlight. These findings suggest the importance of sensitizer-titania interfacial microstructure upon charge recombination

and hold significance for further surface engineering to optimized charge transfer kinetics.

The energetics of the TiO$_2$ CB are known to depend on several factors, such as the local pH,[70−72] the concentration of potential determining ions,[72,73] and the nature of the electrolyte solvent.[73,74] However, the role of surface adsorbed molecules in determining the TiO$_2$ CB energetics is much less clear.[16,75−80] Some researcheres investigated the correlation between the dye protonation state and the DSCs performance,[76−78] showing that dyes carrying a higher number of protons led to higher J_{sc} but lower V_{oc}. An interesting correlation between the dipole moment of coadsorbing species, mainly substituted benzoic acids, and the corresponding V_{oc} was observed by Rühle et al.,[79]
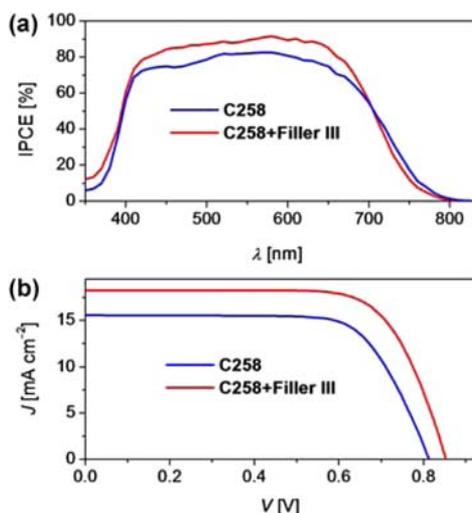
Figure 10. (a) Photocurrent action spectra and (b) J–V curves of cells made with C258 and via cografting C258 with filler III. Reprinted with permission from ref 64. Copyright 2013 Royal Society of Chemistry.

who pointed out a linear relation between the dye coverage (N), the molecular dipole moment (μ), the component normal to the surface (θ is the molecule tilting angle) and the potential shift (ΔV) at the interface

$$\Delta V = \frac{N\mu \cos\theta}{\varepsilon\varepsilon_0} \tag{1}$$

where ε is the dielectric constant of the monolayer and ε_0 is the dielectric permittivity of vacuum.

Study on solid-state DSCs has clearly shown an over 100 mV TiO$_2$ CB shift between a heteroleptic ruthenium dye and an organic dye, and this phenomenon is interpreted in terms of a dipole-induced TiO$_2$ CB shift in opposite direction.[81] Such shifts are generally more difficult to be observed in DSCs based on a liquid electrolyte,[82] in which the high ion strength and the effect of thermal motion hinder the role of interface dipoles. When a dye binds to a semiconductor surface, two effects might be at work: (i) the electrostatic (EL) effect, due to the dye dipole moment, and (ii) the effect of the charge transfer (CT) between the dye and the semiconductor which may accompany the dye-semiconductor bond formation. Ronca et al.[83] recently employed charge displacement analysis to investigate the influence of the adsorption of several prototypical organic dyes and coadsorbents on TiO$_2$ models, quantifying and rationalizing the effects of EL and CT contributions to the TiO$_2$ CB energetics. It was found that the CT effect contributed a large fraction of the calculated CB shift, and the CT contribution was subtly modulated by the dye donor groups. For undissociated monodentate dye adsorption, a CT of ca. 0.10−0.15 electrons was calculated for a dye coverage of ~1 molecule nm^{-2}, inducing a CB shift of 0.02−0.06 eV. The EL contribution to the total CB shift was nicely correlated with the electrostatic potential generated by the adsorbed dye.

The electronic properties of N719 adsorbed onto anatase were recently investigated by using X-ray absorption spectroscopy (XAS) and XPS techniques.[36] It was reported that adsorption of dye molecules can induce additional electronic states between dye molecules and TiO$_2$ surface. The electronic interactions between dye molecules and TiO$_2$ were proposed not only to occur through the covalent bonding of the anchoring groups but also through the aromatic electron

density of the bipyridine groups and the d states found in TiO$_2$, because the electronic structure around the pyridine structures was slightly modified after dye adsorption as revealed by the carbon K-edge X-ray absorption near-edge structure spectra. For the dye coated TiO$_2$, the Ti 2p spectrum was slightly shifted to lower binding energy compared to the uncoated TiO$_2$, indicating that the adsorption of the dye on TiO$_2$ led to a change of the surface dipole and/or a movement of the Fermi level position in the band gap. This picture is also in line with earlier DFT calculations for N3/N719 on TiO$_2$,[77,84] which clearly showed a strong admixture of dye/semiconductor states.

2.3. Interaction of Coadsorbents with TiO$_2$

Dye aggregation, a common phenomenon upon adsorption of dye molecules to TiO$_2$ surface,[85−88] is generally considered as an undesired phenomenon in DSCs. The aggregation leads to deactivation of dye excited state via quenching processes and provokes losses of absorbed photons in the device. Prohibition of aggregation by coadsorption of dye molecules with nonchromophoric adsorbates is recognized as an effective method to improve the device efficiency.[89−94] Generally, the cografting of coadsorbents increases the electron injection yield and results in improved device photocurrent, although the competitive adsorption between coadsorbents and sensitizers may lead to reduced dye coverage.[87,92,93,95,96] However in some cases, the effect of coadsorbent is more complex and can be closely related with the sensitizer structure. In research based on Ru-phthalocyanines sensitizer, which was developed to minimize the formation of aggregates, the coadsorbent (chenodeoxycholic acid, CHENO) was reported to dramatically enhance the photocurrent without lowering the photovoltage.[94] The similarity of the normalized transient absorption traces indicated that CHENO did not affect the electron injection dynamics of the Ru-phthalocyanines sensitized TiO$_2$, and therefore the electron injection quantum yield. Further photophysical measurements showed that the slower recombination of dye cations with the TiO$_2$ electrons and faster regeneration of dye cations by the electrolyte were responsible for the enhanced photocurrent.

In addition to photocurrent, cografting of coadsorbents with sensitizers also benefits photovoltage of DSCs.[91,92,96−99] This effect can be attributed to a negative shift of the conduction band edge and/or the suppression of recombination of the injected electrons with the redox electrolyte. Neale et al.[98] systematically investigated the basic physical processes by which CHENO affected V_{oc} and found that adding CHENO shifted the TiO$_2$ CB to negative potentials by ~80 mV. In their research, the usage of adsorbent also increased the rate of recombination by a factor of 5, indicating that the net enhancement of photovoltage of ~40 mV was the result of both band edge movement and recombination. While the reduced recombination is often attributed to the shielding of recombination centers on TiO$_2$,[96,97] the coassembly of sensitizers and coadsorbents are also proposed to form compact monolayer on TiO$_2$, preventing oxidized species (I$_3^-$) from approaching TiO$_2$ surface.[92,99] The organic molecule, 3,4,5-tris(dodecyloxy)benzoic acid (DOA, which features three hydrocarbon chains, were adsorbed together with the Z907 dye to form a monolayer in a solid-state DSC. Coadsorption of DOA permits preparation of a denser interlayer between hole-transporting material (HTM) layer and the TiO$_2$ surface, thus effectively preventing charge recombination between photo-induced electrons and HTM. The photocurrent of the device is

increased by two times due to the suppressed electron recombination at the TiO$_2$/HTM interface.

2.4. Interaction of Electrolytes with TiO$_2$

The electrolyte is a key component in DSCs. It functions as the HTM and regenerates dye molecules at the photoelectrode. As the electrolyte interacts with both TiO$_2$ nanomaterials and sensitizers, the ions, additives as well as the solvent in the electrolyte dramatically influence the thermodynamic and kinetic properties at the TiO$_2$/dye/electrolyte interfaces.

O'Regan and Grätzel[8] first reported the cation-dependent photoelectrochemical behavior for DSCs. They found that the IPCE at 520 nm can be raised from 68% to 84% upon replacing the tetrapropylammonium iodide electrolyte with the lithium iodide one. Meyer and co-workers[100] studied the impact of cations on the excited-state deactivation of surface adsorbed ruthenium polypyridyl complexes and convincingly demonstrated that the presence of lithium cation (Li$^+$) increased the quantum yield for interfacial electron injection. Further studies based on different sensitizers and electrolytes have achieved similar results and the electron injection dynamics is proven to be strongly dependent upon the nature and concentrations of cations in the electrolyte.[61,101−106] The influence of cations on electron injection dynamics is generally attributed to their interaction with TiO$_2$, and therefore the influence on the TiO$_2$ surface states. The commonly used Li$^+$ ion is known to be potential determining for metal oxide electrodes and the specific adsorption of Li$^+$ on TiO$_2$ leads to positive shift of the conduction band edge (deeper in the energy scale, with respect to electron in vacuum).[61,101,102,105] Although the existence of electronic interaction between dye molecules and Li$^+$ ions may result in reduced excited-state redox potential of the sensitizer,[101,103] the remarkable positive shift of the titania conduction band edge tends to impel favorable energy alignment at the TiO$_2$/dye interface, thus increasing the thermodynamic driving force for electron injection. Further to the enhanced photocurrent due to more efficient electron injection, another prevailing observed phenomenon is the decline of photovoltage upon introducing Li$^+$ ions. This effect is generally attributed to the Li$^+$-induced positive shift of the CB, and the photovoltage deterioration is found to be closely related to the Li$^+$ ion concentration in the electrolyte.[104,106,107] Recently, Wang and co-workers[103] investigated the influence of cations on the electrical characteristics of DSCs and derived a detail profile of the distribution of surface states in mesoporous titania film (Figure 11). Based on quantitative modeling of
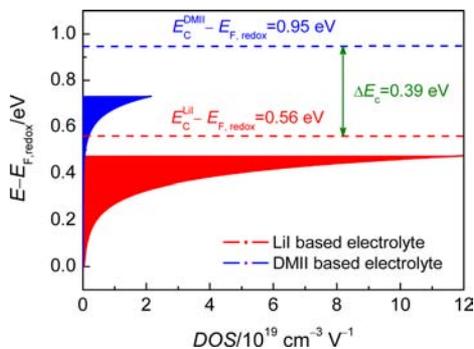
electrical impedance spectroscopy (EIS) results, the Li$^+$ ion was calculated to evoke a downward shift of the conduction band edge by 390 meV as compared with dimethylimidazolium, providing strong evidence for the proposed band edge movement modulated photovoltage shrinkage upon addition of Li$^+$ ions. Besides, the specific adsorption of cations also influences both the interception of photoinjected electrons by I$_3^-$ and the electron transport, thus affecting the charge collection across the TiO$_2$ film.[103,105−110]

4-*tert*-Butylpyridine (TBP), which was initially applied in DSCs by Grätzel et al. in 1993,[111] is a typical additive in highly efficient electrolyte. The presence of TBP in electrolyte induces significant improvement in V_{oc} primarily through uplifting of the titania conduction band edge. Moreover, the adsorption of TBP on TiO$_2$, which is believed to blocking the approach of triiodide to the TiO$_2$ surface and/or removing adsorbed iodine from the surface, can also reduce the electron recombination across the TiO$_2$/electrolyte interface, thus positively influencing the photovoltage of the device.[112−114] Hagfeldt and co-workers[113] investigated the effect of TBP in the DSCs and found that the photovoltage enhancement upon addition of TBP could be attributed to the shift of the TiO$_2$ band edge toward negative potentials (responsible for 60% of the voltage increase) and to an increase of the electron lifetime (responsible for 40% of the voltage increase). They concluded that the action of TBP was both at the semiconductor/electrolyte interface, where it affected the surface charge, and in the electrolyte, where it formed a complex with iodine. In fact, the precise effect of TBP on photovoltaic parameter is not immutable and it is closely related with the properties of the sensitizer and the TiO$_2$/dye/electrolyte interfaces. Recently, the influence of TBP upon the interfacial energetics and kinetics in organic DSCs was investigated based on two push−pull organic dyes C218 and D205.[115] It was revealed that an increment of TBP in electrolyte brought forth comparable elevations of titania conduction band edge for DSCs with C218 and D205. Interestingly, TBP at a higher concentration, while significantly retarded triiodide interception of photoinjected electrons for the C218-based cell, had induced significantly accelerated recombination reaction at a given free electron density for the D205-based cell. This abnormal observation was suggested to be caused by the bracing of the low-lying D205 molecules or by the increased thermodynamic driving force for electron recombination.

Compared with the relatively large number of studies focusing on the importance of TBP in cell performance, the microscopic interaction between TBP and TiO$_2$ is less elucidated. Shi et al.[116] suggested, on the basis of in situ Raman spectroscopy, that some incompletely coordinated titanium atoms can bind TBP molecules by forming Ti ← N bonds. By employing a periodic DFT method with full geometry optimization, Kusama et al.[80] investigated the adsorption of TBP on the TiO$_2$ anatase (101), (100), and (001) surfaces and found that the adsorption of TBP on any surface negatively shifted the TiO$_2$ Fermi level (Figure 12). However, further XPS study gave different results,[117] and indicated that the density of oxygen vacancies on anatase (100) surface did not change upon TBP adsorption. They concluded that the adsorption of TBP on anatase (100) surface did not have any significant effect on the surface band bending and the major role of TBP was to protect the TiO$_2$ surface from adsorption of ionic components in the electrolyte. Although giving clues for better understanding of the interaction between

Figure 11. Distribution of density of states of cells with LiI and DMII based electrolytes. Reprinted with permission from ref 103. Copyright 2010 Royal Society of Chemistry.
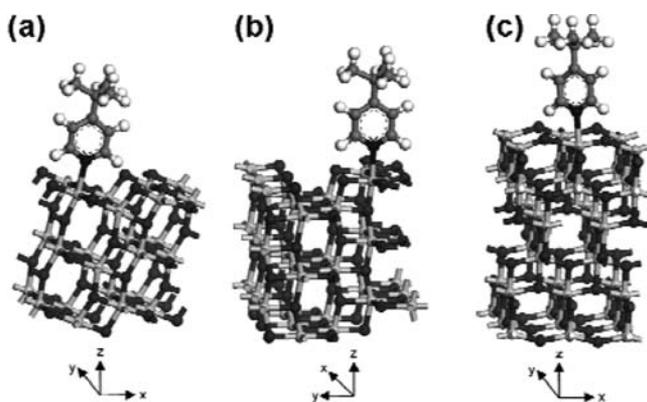
Figure 12. Geometry-optimized structures of TBP adsorbed on a TiO$_2$ anatase (a) (101), (b) (100), and (c) (001) surface. Reprinted with permission from ref 80. Copyright 2008 American Chemical Society.

TBP and TiO$_2$, this result only represents an ideal situation. As the nanostructured TiO$_2$ in DSCs is not made from (100) oriented crystallites, further work is still needed to clarify the realistic situation in DSCs.

Apart from the pronounced effects of ions and additives in the electrolytes, the organic solvents in the electrolytes also have great influence on the photophysical properties of the DSCs. A number of researches employing different solvents revealed that the solvents with large donor number enhanced the photovoltage while reducing the photocurrent of the device.[118−121] The increase of the solvent's donor number is proposed to cause extended coverage of the semiconductor surface by solvent molecules, leading to a negative shift of the TiO$_2$ conduction band edge. Besides the solvent's donor number, the conduction band edge of the TiO$_2$ can also be affected by the dipole moment of the solvent. Hao and co-workers[122] reported the significant solvent dipole moment modulated conduction band edge displacement of the TiO$_2$ electrodes and this effect was responsible for the observed variable driving force for electron injection and the interfacial charge recombination.

Although the highest PCE of 12.3% has been achieved with DSCs based on a porphyrin sensitizer, the utilization of a highly volatile organic solvent presents a momentous challenge in consideration of a robust electrolyte encapsulation for future large-scale DSC application. Ionic liquids (ILs) have been actively pursued as an attractive solution to the evaporation of organic solvent in traditional electrolyte. However, the relatively low fluidity has largely limited the mass transport of redox species and thus the cell performance. As the viscosity of ILs is strongly correlated to the interaction between the cationic and anionic components, mixing high-viscosity iodide ILs with low-viscosity ILs with noniodide anions has been proved to be an effective approach to constructing relatively high-fluidity ionic liquid electrolytes and, as a consequence, to reduce transport limitation problem in the device. The ionic liquid 1-ethyl-3-methylimidazolium dicyanamide (EMIDCA), which features relatively low viscosity, has been utilized in junction with iodide melts to fabricate an over 8% efficiency DSC.[105] A number of researches showed that the dicyanamide anion can passivate the surface states of TiO$_2$, inducing higher photovoltage and lower photocurrent.[123−126] Quantum calculations revealed that the CN nitrogen atom carried more negative charge than the central nitrogen (Figure 13a), thus was more favorable for adsorption on titania.[124] As shown in Figure
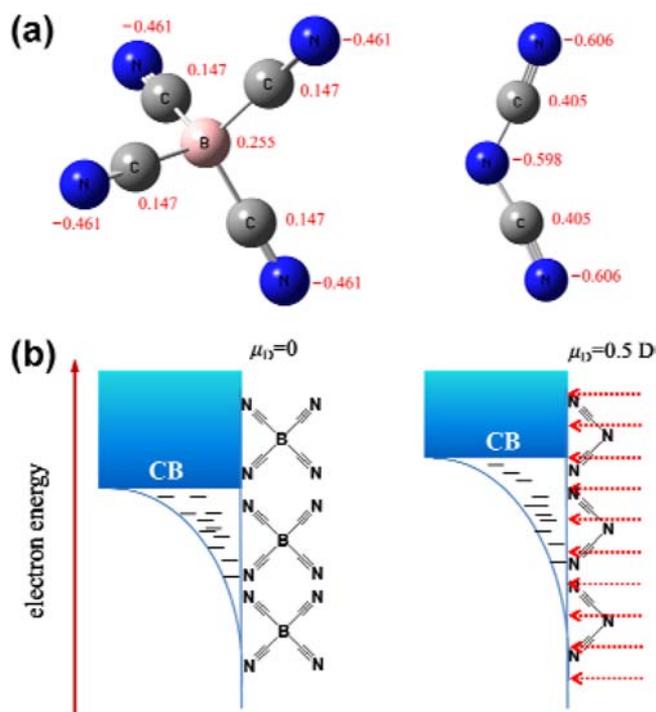
Figure 13. (a) Mulliken charge distributions of TCB (left) and DCA (right) calculated at B3LYP level. Reprinted with permission from ref 124. Copyright 2010 Royal Society of Chemistry. (b) Schematic presentation of the dipole effect on the conduction band edge. Reprinted with permission from ref 125. Copyright 2011 American Chemical Society.

13b, the adsorption of dicyanamide anion on TiO$_2$ surface forms a dipole pointing from electrolyte toward titania, prompting conduction band edge elevation as compared with tetracyanoborate anion.[125] Recently, the attenuated total reflection infrared spectroscopy (ATR-IR) has been applied to investigate the interactions of anions with TiO$_2$.[126] Compared to 1-ethyl-3-methylimidazolium tetracyanoborate (EMITCB) IL, there is a significant blue shift of the CN stretching frequency for the EMIDCA in the presence of TiO$_2$ NPs (Figure 14a,b), implying that EMIDCA interacts more strongly with TiO$_2$ NPs. Femtosecond transient absorption measurements indicates relatively higher electron injection efficiency in the case of EMITCB environment (Figure 14c) and this phenomenon is consistent with previous results.[124,125]

Grätzel and co-workers[127,128] reported the application of cobalt(III) complexes as p-type dopants for spiro-MeOTAD. These cobalt(III) complexes were shown to be beneficial for controlling the charge transport properties of spiro-MeOTAD. Moreover, the properties of the cobalt(III) dopants can be easily adjusted by the modification of the organic ligands and/or the counterion.[128] The solid-state DSC with organic D-π-A molecule Y123 as the sensitizer and tris(2-(1H-pyrazol-1-yl)pyridine)cobalt(III) doped spiro-MeOTAD as the HTM exhibited a record PCE of 7.2% under standard test conditions. Besides cobalt(III) complexes, recent research shown that protic ionic liquids, used as a source of H$^+$, were also effective dopants for small molecule organic semiconductors.[129] The protic ionic liquids promote single electron oxidation, thus increasing the hole concentration and reducing the charge transport resistance in the hole transporting layer.
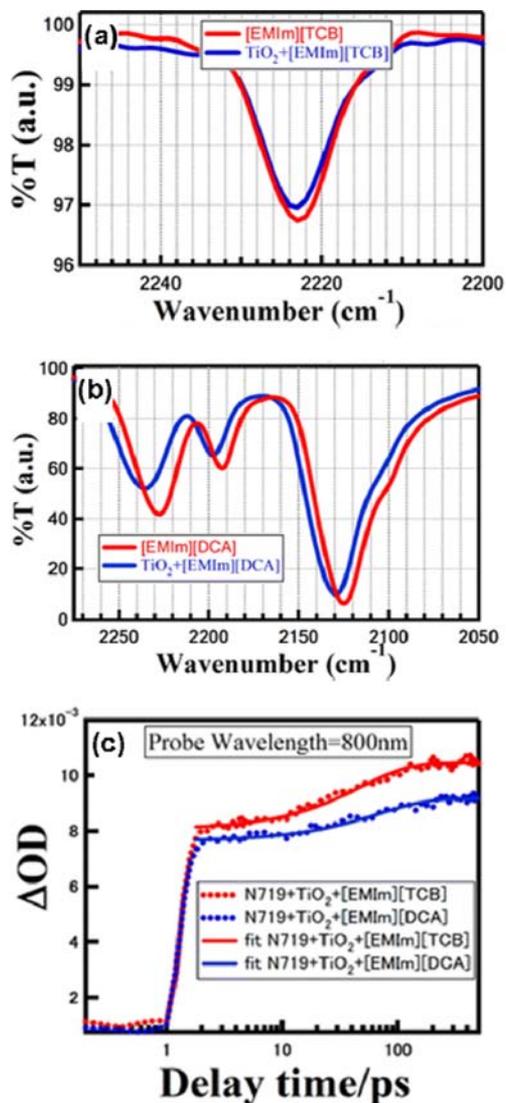
Figure 14. ν(CN) stretching frequencies of (a) EMITCB and (b) EMIDCA ILs with and without TiO$_2$ film. (c) Femtosecond time profile of N719/TiO$_2$ in different IL environments with excitation wavelength of 532 nm and probe wavelength of 800 nm. Reprinted with permission from ref 126. Copyright 2012 American Chemical Society.

2.5. Electrons Transport and Recombination in TiO$_2$ Electrodes

The operation of DSCs consists in electron transfer from a sensitizer to the TiO$_2$ electron conductor network, followed by transport of electrons to the collector of conducting substrate, avoiding recombination along the way. The accumulation of electrons in TiO$_2$ is the origin of photovoltage, and the flow of electrons results in the photocurrent. Therefore, there has been enormous interest in a detailed understanding of the electronic steps in the metal oxide semiconductor, which control the observed transport and recombination features.[130,131] Nanocrystalline TiO$_2$ used in DSCs normally consists of anatase particles of the order of 20 nm size sintered on top of conducting glass to form a rigid framework with high internal surface area, as shown in Figure 15a. The voltage V is defined by the expression

$$qV = E_{Fn}(x = 0) - E_{redox} \qquad (2)$$
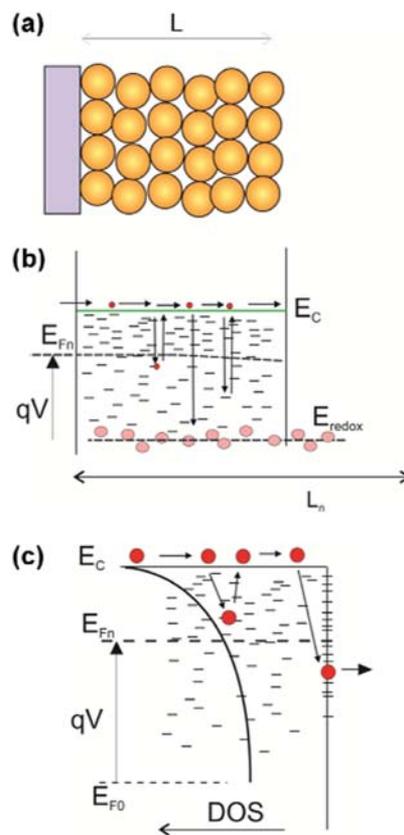
Figure 15. (a) Mesoporous structure of thickness L that forms the electron transport materials in a DSC. It is formed by interconnected particles that allow the transport of electrons via extended states, as indicated in the energy diagram. (b) The potential V at the substrate fixes the electron Fermi level at the edge of the nanostructured semiconductor, with respect to the Fermi level of the hole conductor. The localized states in the bandgap trap and release the diffusing electrons. Injected electrons at the contact have a probability to diffuse and recombine by charge transfer to the holes species, so that the effective penetration in the layer is governed by the diffusion length L_n. It is shown a case in which the diffusion length is longer than film thickness. (c) Electronic energy disorder is well described by an exponential density of states that decreases from the edge of the CB to the center of the gap. The surface states have a strong influence in electron transfer to the acceptor species, that constitute recombination in a DSC.

where q is elementary charge, E_{Fn} is the Fermi level of electrons in the metal oxide, and E_{redox} is the redox potential in the electrolyte, or hole Fermi level in the case of solid HTMs.

The TiO$_2$ phase formed by well-connected anatase NPs can be considered as a homogeneous medium in which electrons undergo a number of processes, indicated in Figure 15b. A main process is the transport of electrons in the extended states of the CB (or mobility edge), where the concentration of free electrons n_c is defined as

$$n_c = n_{c0}e^{qV/k_B T} \qquad (3)$$

Here $k_B T$ is thermal energy and n_{c0} is an equilibrium concentration in the effective density of states of the conduction band N_c. In a steady state situation, the traps remain at equilibrium occupation and the main effect governing transport is the displacement of electrons in the CB. The conductivity σ_n is a main parameter of the solar cell, as in practice it works in steady state conditions. σ_n determines a

series resistance that should be removed if it is too large with respect to other resistances in the device. The expression of the electron conductivity associated to free carrier transport is[132]

$$\sigma_n = \frac{q^2 D_0}{k_B T} n_c \qquad (4)$$

Here D_0 is the free electron diffusion coefficient. Therefore the conductivity dependence on voltage shows a simple exponential dependence on voltage with a slope $(k_B T)^{-1}$ due to Boltzmann distribution function of electrons in the CB. This result has been observed in high quality measurements using the transport resistance of impedance spectroscopy;[133−135] however, it should be noticed that under illumination other effects play a role and some quantities are displaced form the ideal dependence.[136]

Since early work,[137] it was recognized that localized states have a large influence in kinetic processes in DSCs. TiO_2 NPs show a large number of localized states in the bandgap, with total number N_L, and number density n_L. These localized states are able to capture electrons, and later eject them back to the transport level. Traps below E_{Fn} are almost fully occupied, hence inactive for trapping events, while traps above the Fermi level are nearly empty. Therefore, the probability of electron capture is strongly determined by the position of E_{Fn}. A localized state at energy E_t releases electrons at a rate $\tau_t^{-1} = \beta_n N_c e^{(E_t - E_c)/k_B T}$, where β_n is the time constant for electron capture, which is independent of trap depth. Since τ_t increases exponentially with the depth of the state in the bandgap, the slowest trap is the deepest unoccupied trap. This fact is the cause that many quantities in DSC measurement are observed to depend exponentially on the Fermi level, as will be further justified later. The effect of traps is dominant whenever a transient effect is induced, in which the position of the Fermi level is modified, with the correspondent need for traps release. In contrast to DC conductivity, several kinetic coefficients of a DSC are strongly influenced by traps, and an understanding of such effects is critically important for a useful interpretation of the experimental results.[138−141]

Traps, especially surface states, also become a dominant aspect of the recombination of electrons in a DSC, that is a charge transfer to the electrolyte or hole conductor, as shown in Figure 15c. These phenomena have been widely studied using small perturbation techniques such as impedance spectroscopy,[135,142−144] intensity modulated photocurrent and photovoltage spectroscopies,[145−149] electron lifetime by time transient decays,[150,151] and also by stochastic numerical simulation.[152−158]

The specific density of localized states (DOS) in the bandgap of TiO_2, $g(E)$, that is outlined in Figure 15b,c, can be established by capacitance techniques that provide the chemical capacitance, that is defined as follows[159]

$$c_\mu = q^2 \frac{dn}{dE_{Fn}} \qquad (5)$$

It corresponds to a capacitance per unit volume. Using the approximation of the zero-temperature limit of the Fermi function, i.e., a step function at $E = E_{Fn}$ separating occupied from unoccupied states, it can be shown that the capacitance of localized states takes the form[139]

$$c_\mu^L = q^2 g(E_{Fn}) \qquad (6)$$

Thus c_μ provides a direct reading of the DOS at the Fermi level.

The capacitive behavior of nanoparticulate TiO_2 films has been widely studied.[160,161] The main feature is an exponential bandtail that enters the gap of the semiconductor, with effective DOS

$$g(E) = \frac{N_L}{k_B T_0} \exp[(E - E_c)/k_B T_0] \qquad (7)$$

Here T_0 is a parameter with temperature units that determines the depth of the distribution, that is alternatively expressed as a coefficient $\alpha = T/T_0$. Representative examples of the chemical capacitance of a range of DSCs are shown in Figure 16.[144] It is
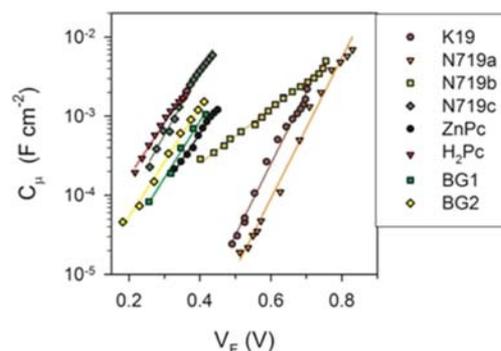
Figure 16. Chemical capacitance and recombination resistance of a collection of DSCs with different dyes and electrolytes as described in represented vs the potential VF in which series resistance contribution has been removed. Reprinted with permission from ref 144. Copyright 2011 Royal Society of Chemistry.

observed that the exponential shape is well obeyed. A noteworthy feature is the horizontal displacement of the exponential DOS along the voltage axis. This feature is due to the displacement of the CB level E_c with respect to redox energy level E_{redox}, caused by surface conditions at the semiconductor/electrolyte interface. These features can be determined and taken into account by combined measurement of capacitance, transport resistance R_{tr}, and recombination resistance R_{rec} in impedance spectroscopy.[162]

The origin of the exponential DOS in anatase TiO_2 has not yet been conclusively established. The DOS resembles that of standard disordered amorphous semiconductors,[163,164] and it is usually attributed to structural disorder. It should be pointed out that electrons in TiO_2 show strong polaronic features. The self-trapping effect causes a strong Stokes shift between light absorption and emission that is well observed at low temperatures. While excitation by a photon is a vertical transition that takes place above the anatase bandgap value of 3.2 eV, photoluminescence occurs from the self-trapped state and has a maximum at 2.3 eV.[165,166] The difference is associated with the stabilization of the electron−lattice system in the excited state. Self-trapped excitons in TiO_2 also produce the Urbach tails observed in absorption measurements.[167] Quantum mechanical calculations[168] indicate that the electron becomes self-trapped at a Ti lattice site (Ti^{4+}), which then becomes formally Ti^{3+}, with an energy gain (trapping energy) associated with the polaronic distortion $\Delta E_{trap} = 0.23$ eV, while the self-trapping energy of a hole is 0.74 eV. Recent DFT calculations suggest that disorder is not really a necessary requirement to explain the DOS features of small anatase NPs, which can be also caused by under-coordinated 4-fold

coordinated surface Ti atoms mainly lying at the (100) edges found at the intersections between (101) surfaces.[169]

In principle it appears extremely complex to calculate the relevant kinetic coefficients such as electron diffusion coefficient D_n, and electron lifetime τ_n, in the presence of many and energy-distributed localized states that are indicated in Figure 15. However the model is greatly simplified by a condition that actually removes the kinetic equation for the traps.[170] If the trapping kinetics is fast (with respect to time scale of the transient measurement) we may assume that the traps follow the equilibrium relation with the free carriers

$$\frac{\partial n_L}{\partial t} = \frac{\partial n_L}{\partial n_c}\frac{\partial n_c}{\partial t} \tag{8}$$

This assumption is termed the quasistatic approximation and it was introduced to account for the properties of measured time constants in DSCs.[138,156,170] Since eq 8 is well obeyed by ordinary DSCs, the following results can be demonstrated.[141,156] The chemical diffusion coefficient of the electrons has the form

$$D_n = \left(\frac{\partial n_L}{\partial n_c}\right)^{-1} D_0 \tag{9}$$

A calculation of the trapping factor $\partial n_L/\partial n_c$ provides the following result

$$D_n = \alpha^{-1}\frac{N_c}{N_L}\exp\left[(1-\alpha)\frac{E_{Fn}-E_c}{k_BT}\right]D_0 \tag{10}$$

A representative set of measurements of DSCs with different types of hole conductors is shown in Figure 17a. The horizontal axis shows the electron conductivity, which removes the CB shift for the different types of DSCs. It is observed that D_n shows a nearly universal behavior that follows well eq 10.

The description of the electron lifetime requires additional steps. It is necessary to first define the free carrier lifetime τ_f[156,171] in terms of the recombination rate U_n

$$\tau_f = \left(\frac{\partial U_n}{\partial n_c}\right)^{-1}_{\bar{n}_c} \tag{11}$$

that corresponds to the surface charge transfer events indicated in Figure 15c. In addition, the measured lifetime is also influenced by prior trapping and release events, as also shown in Figure 15c. The electron lifetime is defined with respect to total carrier density

$$\tau_n = \left(\frac{\partial U_n}{\partial n}\right)^{-1}_{\bar{n}} \tag{12}$$

In the model of Figure 15c the lifetime takes the form[171]

$$\tau_n = \left(\frac{\partial n_L}{\partial n_c}\right)\tau_f \tag{13}$$

that includes the trapping factor. A phenomenological model that gives good results in many cases is the following:[135,172]

$$U_n = k_{rec}(n_c^\beta - n_{c0}^\beta) \tag{14}$$

This last model can be explained by combining the transference through an exponential distribution of traps, with the Marcus model for electron transfer.[55,135,141,171,173] It follows
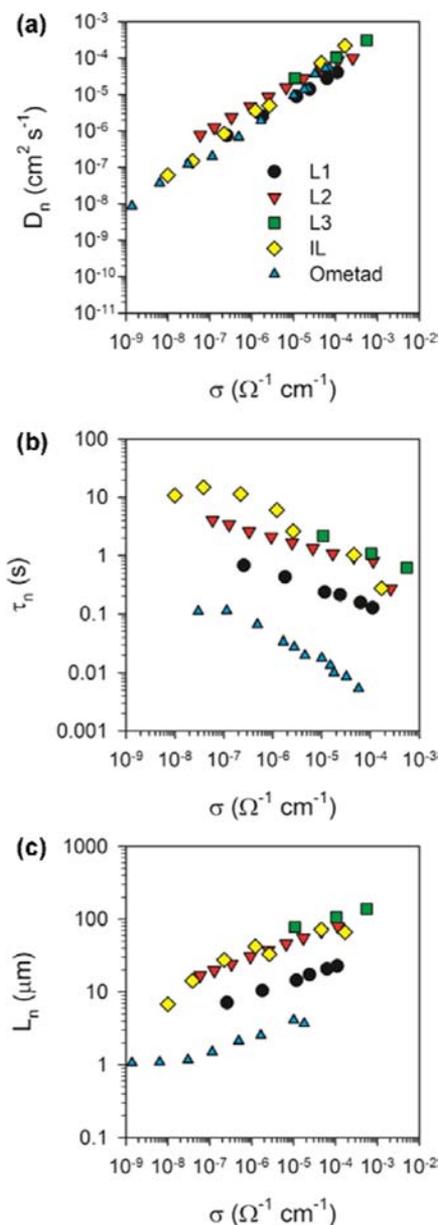
Figure 17. Representation of several magnitudes for diffusion-recombination in DSCs, as a function of electron conductivity, (a) diffusion coefficient, (b) lifetime, and (c) diffusion length, of electrons in the nanocrystalline TiO$_2$ for several DSCs, measured in dark conditions, with different holes transport material: L for liquid electrolyte, IL for ionic liquid electrolyte, and Ometad for solid hole conductor. Efficiencies of the different samples are 4% for Ometad, 5% for L1, 7% for IL, 10% for L2, and 11% for L3. Reprinted with permission from ref 179. Copyright 2009 American Chemical Society.

from eq 14 that the free carrier lifetime depends on the voltage as follows

$$\tau_f = \frac{n_{c0}^{1-\beta}}{\beta k_{rec}}\exp\left[(1-\beta)\frac{qV}{k_BT}\right] \tag{15}$$

thus the lifetime has the expression[171]

$$\tau_n = \frac{T}{T_0}\frac{n_{L0}}{n_{c0}^\beta \beta k_{rec}}\exp\left[(\alpha-\beta)\frac{qV}{k_BT}\right] \tag{16}$$

The results of measurements of τ_n are shown in Figure 17b. It should be noticed that τ_n decreases upon increasing voltage, but this dependence is an effect of the trapping factor $\partial n_L / \partial n_c$, that introduces the dependence $(\alpha - 1)V$ in the exponent. In fact the free carrier lifetime τ_f increases with voltage as shown in eq 15.

In the operation of the solar cell, the transport of photogenerated electrons competes with recombination events and determines the collection efficiency of the solar cell.[174,175] The diffusion length L_n can be broadly defined as the average distance that injected carriers travel from $x = 0$ before disappearing from the diffusing medium, as suggested in Figure 15b. If L_n is longer than the film thickness L, then most of the carriers photoinjected along the TiO_2 have a large chance to be collected at the substrate, and the collection efficiency will be nearly unity. The relationship of the diffusion length to the film thickness can be determined by the ratio of the recombination resistance to the transport resistance as follows:[142]

$$\frac{R_{rec}}{R_{tr}} = \left(\frac{L_n}{L}\right)^2 \tag{17}$$

In the diffusion-recombination model the diffusion length is given by

$$L_n = \sqrt{D_n \tau_n} \tag{18}$$

This standard result has been shown to be valid for nonlinear recombination combined with multiple trapping transport, provided that carrier density is nearly uniform.[176] In multiple trapping model the trapping factors in eqs 9 and 13 compensate in the diffusion length.[138] This feature, the disappearance of the trapping factors, is a characteristic of steady state quantities as remarked above for the electron conductivity. Nevertheless, it has been recognized that the electron diffusion length in a DSC is dependent on the Fermi level.[172] If the free carrier lifetime shows some dependence with the potential, then the diffusion length varies with voltage, according to

$$L_n = \sqrt{D_0 \tau_f} \tag{19}$$

Using the free carrier lifetime of the nonlinear β-recombination model, eq 15, it is found that the diffusion length increases with the voltage, and this feature, is often observed in experimental results, as shown in Figure 17c.[138,139,171,177−179]

2.6. Nanostructured TiO_2 Electrodes for DSCs

The nanocrystalline morphology of the TiO_2 film is critical for the efficient operation of DSCs. The major breakthrough for DSCs in 1991 was realized by using the mesoporous TiO_2 electrode with a high internal surface area to support the monolayer of a sensitizer,[8] which immensely improved the light harvesting capability as well as the photocurrent of the device. In DSCs, anatase is considered as the preferred structure because it features a larger bandgap and higher conduction band edge energy as compared with rutile. The higher conduction band edge energy of anatase is expected to induce higher E_{Fn} and thus V_{oc} in DSCs at the same conduction band electron concentration. Moreover, a comparative study of rutile- and anatase-based DSCs reveals that the short-circuit photocurrent of the rutile-based cell is about 30% lower than that of the anatase-based cell.[180] The low photocurrent of the rutile film is ascribed to a reduced amount of adsorbed dye, which is caused by a smaller surface area per unit volume

compared with that of the anatase film. The detailed synthesis procedure for TiO_2 film to realize DSCs with PCE over 10% was published by Grätzel's group.[181] For state-of-the-art DSCs, the employed mesoporous TiO_2 films are comprised of double functional layers including a light-absorbing layer composed of 20 nm sized anatase particles and a light-scattering overlayer composed of 200−400 nm sized anatase particles. This bilayer structure increases the light scattering effect and facilitates the light harvesting of DSCs. Besides the bilayer architecture, multilayered TiO_2 nanostructured films are also reported by several groups.[182−186] These multilayered films are proved to be beneficial to the light harvesting and/or the charge collection in the device. Recently, Diau's group[184] reported the fabrication of multilayered TiO_2 films with additional layers of nanorods inserted between the transparent and the scattering layers as shown in Figure 18. The corresponding DSC based on Z907 sensitizer exhibited significantly enhanced light-harvesting and electron transport capability, achieving an improved PCE of ∼10%.
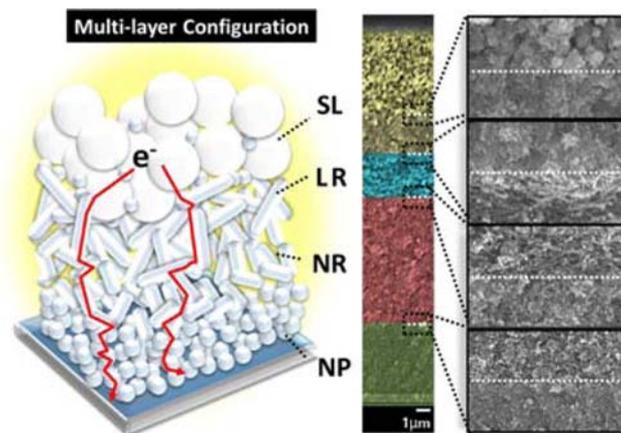
Figure 18. Schematic demonstration of the structural design for the TiO_2 multilayer film. NP, SL, NR and LR refer to nanoparticles, scattering layer and TiO_2 nanorods of ∼150 and ∼500 nm, respectively. Reprinted with permission from ref 184. Copyright 2013 American Chemical Society.

Although these kinds of nanoparticle films have been regarded as a paradigm of porous photoelectrode for use in DSCs, a variety of nanostructures has been tested thus far. These studies are motivated by the expectation that 3D packed particle network of TiO_2 which are normally used for DSCs provides a tortuous pathway for electron transport, thus increasing the possibility of charge recombination and deteriorating the charge collection efficiency of the device. As one-dimensional (1D) nanostructures are expected to provide direct pathways for charge transport and improve the charge collection efficiency of the DSCs, the research has been largely promoted toward photoanodes constructed from ordered 1D nanostructures such as, nanotubes (NTs),[187−195] nanorods (NRs),[196−200] nanowires[201−205] etc.

NTs are thought to be superior to other 1D nanostructures as their hollow structure can provide larger surface area than that of nanowires or NRs. In most cases, the self-organized TiO_2 NT layers are formed by anodic oxidation of a Ti-metal sheet in ethylene glycol electrolytes in presence of fluoride ions. However, the obtained TiO_2 NT arrays are not always highly ordered because the tube upper parts may collapse and form

bundles or needle-like structures due to the chemical etching effect in the fluoride electrolyte.[206,207] These intertube contacts lengthen electron transport pathway from the expected one dimension to a combination of one and three dimensions, thus adversely affecting the charge transport in NT films. Recently, the synthesis of bundle-free NT films has been presented by Frank and co-workers by employing a combinative technique of cleaning with ethanol and drying in supercritical CO_2.[191] In usual condition of cleaning with water and then drying in air, there are evident NT bundles, microcracks, and an overlayer which covers the ends of NT channels (Figure 19a). The
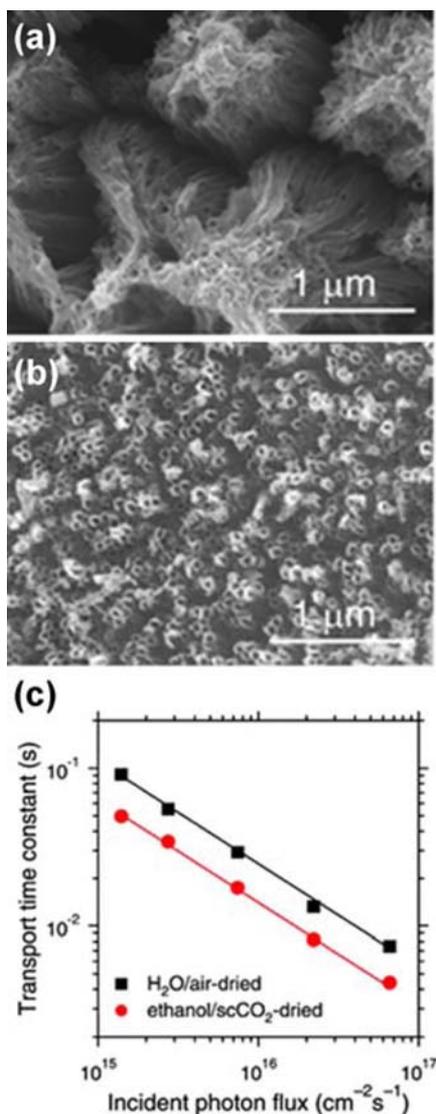
Figure 19. SEM images of NT films that were cleaned with (a) water and then air-dried (b) ethanol and then scCO₂-dried. (c) Corresponding transport time constants for DSCs incorporating different NT films. Reprinted with permission from ref 191. Copyright 2007 American Chemical Society.

application of ethanol and drying in supercritical CO_2 induces decreased surface tension, and consequently eliminates the NT bundling and microcrack formation (Figure 19b). As shown in Figure 19c, the electron transport in the bundle-free NT film is two times faster than in its conventional NT counterpart. This is because the supercritical CO_2 drying process reduces the formation of clusters of bundled NTs, thus promoting 1D

transport, which shortens the transport pathway, lessens the exposure of electrons to traps, and enables overall faster transport. Besides, the bundle-free NTs are also able to provide an enlarged internal surface area accessible to dye molecules, leading to dramatically increased J_{sc} for the device. By employing a hybrid anodic method, with initial potentiostatic anodization followed by galvanostatic anodization, Diau's group successfully synthezised long titania NT arrays in a much shorter anodization period.[193] The DSCs based on these NT films showed systematically improved cell performance depending on tube length, exhibiting the highest PCE of 7.6% at a tube length of ∼30 μm.

As TiO_2 NT arrays are commonly grown on opaque titanium foils or sheets,[189,208] the derived devices typically adopt a back-side illumination geometry. However, this configuration is a less than optimal approach for achieving high efficiency because the incident light could be dramatically attenuated due to the light reflecting effect of the counter electrode and light absorbing effect of the electrolyte.[209] Besides, in back-side illumination configuration, most photoelectrons are generated near the outermost regions of the NT film. These electrons have to travel longer distance before being collected at the fluorine-doped tin oxide-coated (FTO) glass substrate, thus inducing higher carrier loss due to electron recombination with oxidizing species in the electrolyte.[210] To overcome these drawbacks, attempts have been taken to prepare the titania NT on FTO glass substrate and fabricate cells with front-illumination configuration.[188,192,211−214] One feasible option to realizing the front-side illumination geometry is to directly grow titania NT on FTO glass substrate.[213,214] In this case, transparent TiO_2 NT/FTO glass is prepared via anodic oxidation of titanium thin film that is previously sputtered onto FTO conductive glass. Another method for fabrication of transparent NTs on FTO glass involves detaching self-standing TiO_2 NT membranes from Ti subtracts and then fixing them on FTO glass by a bonding interlayer.[188,194,211,212] This methodology is simple and low-cost, and devices prepared with this method have reached the highest efficiency of 7.6%.[188]

Besides those 1D TiO_2 electrodes, 3D nanostructures have exhibited significant potential to obtain efficient devices. The 3D nanostructured photoelectrodes not only provide enlarged surface area to improve the light trapping effect, but also show excellent capability in achieving highly effective charge transport and collection. Diau and co-workers[215] reported the synthesis of octahedron-like anatase TiO_2 single crystals with particle sizes in the range of 30−400 nm by employing a simple two-step sol/hydrothermal method, in which the first step was the preparation of a suitable titanium tetraisopropoxide (TTIP)/triethanolamine (TEOA)/diethylamine (DEA) sol at a basic condition and the second step involved a hydrothermal treatment at varied temperature and duration. In this approach, the TEOA was used as a chelating agent to retard the hydrolysis and the base DEA played bifunctional roles as both a catalyst and a controller of shape for the crystal growth. Measurement of N719-sensitized solar cell with octahedron-like anatase TiO_2 single crystals of ∼30 nm as active layer and ∼300 nm as scattering layer revealed a PCE of 10.2%, which was superior to that of 9.6% for the NP-based reference device. The improved performace was attributed to the more rapid electron transport and negative TiO_2 CB edge. Recently, mesoporous single crystals (MSC) anatase TiO_2 was synthesized through a method of crystal seeding in a sacrificial guiding template.[216] A silica template with an external volume of ∼1% of the overall

O

dx.doi.org/10.1021/cr400606n | Chem. Rev. XXXX, XXX, XXX−XXX

reaction volume was first seeded by pretreatment in a solution of $TiCl_4$ and then removed by selective etching in aqueous NaOH to recover the mesoporous TiO_2 crystal product, obtaining a near unity yield of clearly faceted single crystals of anatase TiO_2 as shown in Figure 20. The MSC TiO_2 film
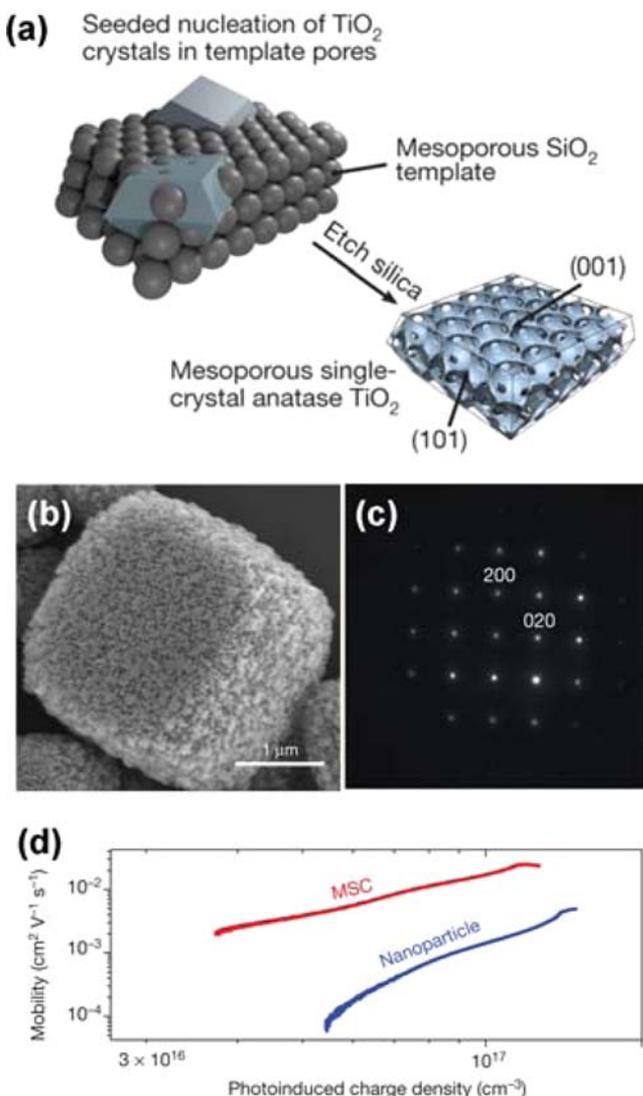
Figure 20. (a) Schematic of MSC nucleation and growth within a mesoporous template. (b) Fully mesoporous TiO_2 grown by seeded nucleation in the bulk of the silica template. (c) Electron diffraction Laue pattern collected from a complete mesoporous crystal assigned to anatase TiO_2 with [001] beam incidence. (d) Mobility dependence on photoinduced charge density for MSC and NP films measured via transient mobility spectroscopy. Reprinted with permission from ref 216. Copyright 2013 Nature Publishing Group.

features specific free surface similar to equivalent-sized NPs, providing highly accessible surfaces for dye adsorption as well as effective light adsorption. Besides, the conductivity and electron mobility of MSCs are significantly higher than that of conventional NP films. And more importantly, the MSC films can be prepared in a relative low temperature (below 150 °C), thus decreasing fabrication cost and making the use of flexible substrates possible. Applying this low-temperature MSC TiO_2 films in solid-state DSCs yielded a PCE of 3%, which was vastly

greater than that of the best low-temperature all-solid-state device.

As in solid-state DSCs, the charge recombination rate can be 2 orders of magnitude faster and electron diffusion length is about 1 order of magnitude lower than that in liquid electrolyte-based DSCs.[147,179,217,218] The relatively low electron collection efficiency combined with incomplete filling of the mesoporous TiO_2 films with HTM limits the photoanode thickness to less than 3 μm, which is not the optimized thickness to achieve effective light absorption with the currently available sensitizers. Tétreault et al.[219] presented a novel solid-state DSC based on a 3D fibrous network of anatase self-assembled from fused single-crystal NRs. As shown in Figure 21, the nanowires first self-assemble in two dimensions parallel
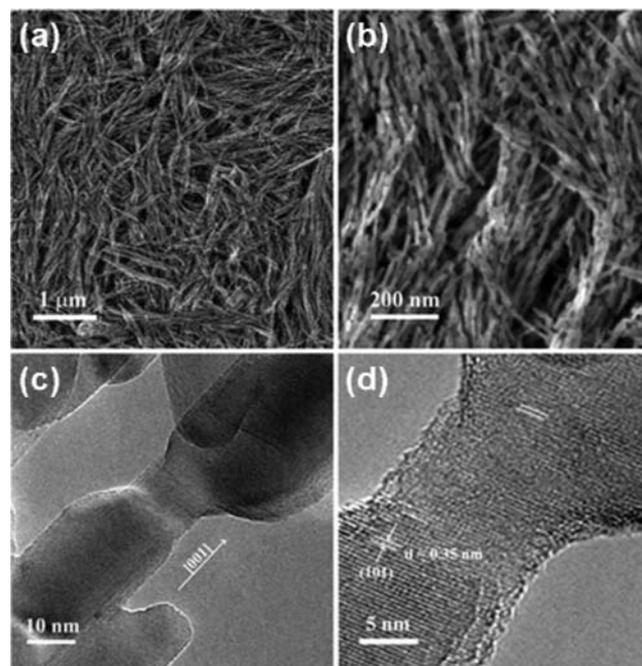
Figure 21. (a) HRTEM image of the 3D fibrous network of single-crystalline anatase nanowires. (b) Oriented self-assembly of the NRs into the 3D fibrous network. (c) HRTEM image showing the continuous [001] crystal orientation across two NRs. (d) Continuous (101) crystal plane and spacing across the junction. Reprinted with permission from ref 219. Copyright 2010 American Chemical Society.

to the FTO grass substrate and then undergo a transformation into chain-like assembly of truncated anatase NRs during the subsequent thermal decomposition process. Compared to conventional films based on anatase NPs, the 3D network of NRs exhibits a wide pore size distribution composed of large mesopores (10−50 nm) and macropores (50−120 nm), resulting in 25% reduction of its surface area as compared with traditional NP-based electrode. However, the relatively low dye loading in the 3D network film is partly compensated by significant light scattering effect and the large anisotropy of the nanowires lead to low packing density, allowing for efficient infiltration of the HTM into this 3D network films. The DSC based on the 3D network of NRs presents a significantly higher conductivity, shorter transport time, and longer electron lifetime over a wide range of applied potential as compared to its NP counterpart, resulting in improved collection efficiency. The relatively high roughness factor, significant light scattering combined with facilitated electron collection

lead to a relatively high PCE of 4.9% for solid-state DSCs. The 3D hierarchical nanostructured TiO_2 films are also widely investigated as photoanodes for DSCs in recent years.[220−226] These 3D hierarchical photoelectrodes promote light scattering and the dye loading of the electrodes simultaneously, to enhance the light harvesting capability of the device. Moreover, the charge transport and collection capability of the resulting cells are thought to be improved upon utilizing these 3D hierarchical photoelectrodes.

In DSCs, an important approach to boosting efficiency is to increase the path length of light by enhancing light scattering in TiO_2 films. While the small size of TiO_2 NPs makes conventional nanocrystalline TiO_2 films almost transparent, mixing light scattered large particles or covering a scattering layer onto the nanocrystalline film has been perceived as an effective strategy to improve light absorption. The inverted TiO_2 photonic crystals (PCs), which consist of self-assembled monodispersed spherical particles, has exhibited significant potential to obtain efficient light harvesting within a specific wavelength based on their intrinsic periodic structure. Moreover, large porosity structures of the inverted TiO_2 PCs have enabled good infiltration for high-viscosity electrolytes. To realize the PC-coupled DSCs that feature enhanced photocurrent over a large spectral region, a double layered photoanode integrates a high surface mesoporous underlayer TiO_2 with an optically active TiO_2 PC overlayer is fabricated as illustrated in Figure 22.[227] The significantly improved IPCE of
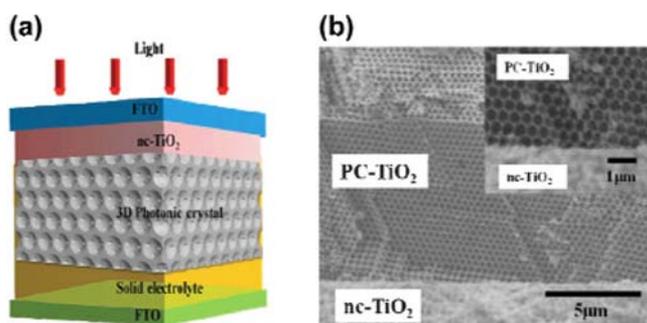
Figure 22. (a) Schematic of the DSC based on double layer photoanode. (b) SEM cross section image of FTO/nanocrystals-TiO_2/PC-TiO_2 electrode. Reprinted with permission from ref 227. Copyright 2012 Royal Society of Chemistry.

PC DSC indicates that the PC top layer is electrically connected and contributes to light harvesting over the entire spectrum. Further increasing the thickness of PC-TiO_2 top layer from 14 to 20 μm led to a boosted efficiency of 8.2% and this enhancement can be explained by effective electrolyte infiltration and improved absorption in a specific spectral region owing to the PC effect.

Recently, a simple, fast, and universal nanopatterning methodology has been developed by Kim et al. for boosting the light harvesting efficiency of DSCs.[228] A TiO_2 layer of ~10 μm prepared with an acidic paste was first casted on the FTO glass substrate and then covered with the second thin layer made from neutral TiO_2 paste. The elastomeric polydimethylsiloxane nanostamp was then manually placed on the neutral paste-coated photoelectrode with proper pressure to obtain the nanopatterned photoanode. In this procedure, the application of neutral paste is crucial, because the patterned photoelectrode prepared with a neutral TiO_2 paste has a hydrophilic nature,

which is more appropriate for successful dye adsorption. As shown in Figure 23, the periodic line patterns deposited on the surface of photoanode can boost the optical path length across a broad wavelength range of incident light by reflecting the light back to the photoelectrode, thus leading to more effective light absorption. Further comparison of the reflection behavior indicates effective light trapping from the 400 to 1000 nm wavelength range for the nanopatterned sample, providing strong evidence for the improved light harvesting ability of this newly developed electrode. The application of nanopatterns in solid-state DSCs has resulted in approximately 40% and 33% enhancement of J_{sc} and PCE, respectively, achieving a high efficiency of 7.03%.

One important strategy for improving electron collection is the utilization of metal oxides with high electron mobility, such as ZnO[229−232] and SnO_2[233] as porous semiconductor materials for DSC photoanode. Despite enhanced electron transport, the reported device efficiencies based on these materials are much lower than that of TiO_2 mainly because of the severe recombination when the high mobility material is in direct contact with the sensitizer and/or the electrolyte. Consequently, the development of core-sell structured photoanodes with both high electron mobilities and reduced recombination rates has emerged as a promising approach to enhancing the performance of DSCs. A novel bottom-up 3D host−passivation−guest (H−P−G) photoanode was recently reported for achieving highly efficient electron transport and charge extraction.[234] This H−P−G structure employs high electron mobility materials, such as aluminum-doped ZnO (Al/ZnO) or SnO_2 as hosts to facilitate the electron transport in photoanode. As shown in Figure 24, the dispersion of polystyrene spheres is first doctor bladed on a FTO glass substrate to attain a large-area highly light scattering disordered template and then heated and infiltrated with 90 nm of Al/ZnO, SnO_2, or TiO_2 by atomic layer deposition. The high-mobility oxide backbone is then coated with a dense layer of TiO_2 (passivation layer) to hinder the electron recombination between electrons in the oxide backbone and I_3^- in the electrolyte. TiO_2 nanocrystals, which are called guest, are further infiltrated the macroporous inverse transparent conductive oxide backbone in order to increase the surface area for dye loading. As shown in Figure 25, this 3D open structure exhibits effective pore connectively and enables conformal coating of dense TiO_2 on the 3D host. $J−V$ characterization of DSC revealed that the electrodes with SnO_2 and Al/ZnO as host exhibited higher J_{sc} and V_{oc} as compared with the TiO_2 host counterpart. This phenomenon is regarded as the consequence of the relatively high electron mobility in the Al/ZnO and SnO_2 hosts. Moreover, an improvement in photovoltage of up to 110 mV was obtained for the Al/ZnO host photoanode, indicating the successful suppression of charge recombination with the H−P−G structure.

3. APPLICATION IN POLYMER-INORGANIC HYBRID SOLAR CELLS

3.1. Fundamentals of Polymer-Inorganic Hybrid Solar Cells

Recent research on polymer-inorganic hybrid solar cells has generated a promising approach for cost-effective and large-scale solar energy conversion. This kind of solar cell combines the advantages of inorganic semiconductors, such as high electron mobility and stability, with the processing flexibility offered by conjugated polymers. In these devices, light is
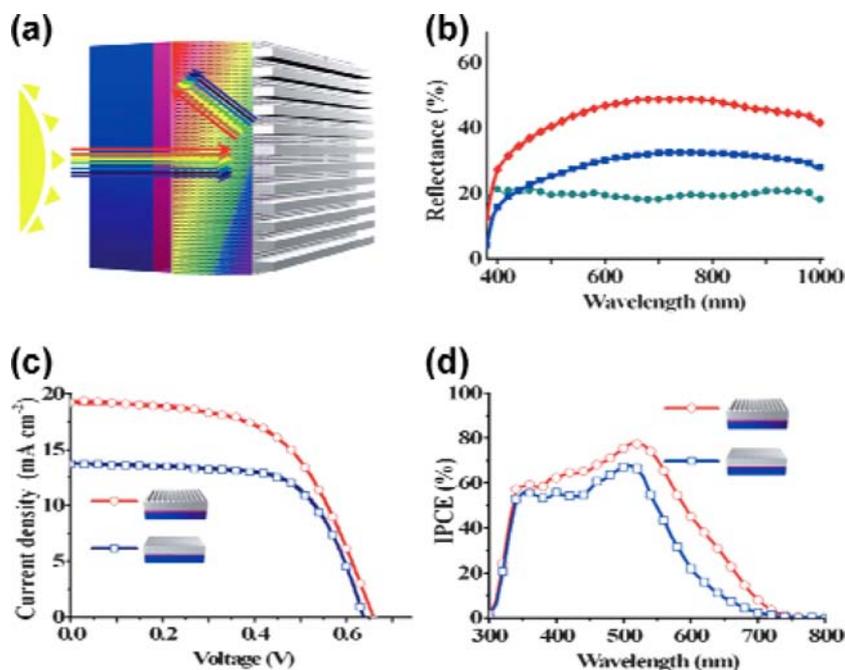
Figure 23. (a) Schematic representation of the light trapping on the nanopatterned TiO$_2$ layer. (b) The reflection behaviors of the compact, flat, and nanopatterned TiO2 layers. (c) $J-V$ curves and (d) IPCE spectra of DSCs with and without a nanopattern on mesoporous TiO$_2$ photoelectrodes. Reprinted with permission from ref 228. Copyright 2012 Wiley-VCH.
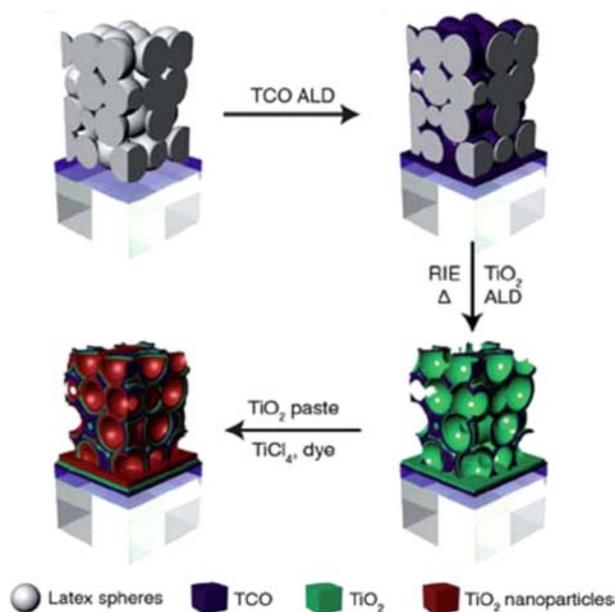
Figure 24. Schematic representation of the synthesis method for a 3D host–guest photoanode of DSC. Reprinted with permission from ref 234. Copyright 2011 American Chemical Society.

Figure 25. (a) SEM cross sectional view of a disordered TiO$_2$ passivated 3D Al/ZnO backbone. (b) Top-view of the 3D Al/ZnO after top surface removal by reactive ion etching and template removal by annealing. (c) High-magnification micrograph of the TiO$_2$ covered 3D Al/ZnO host. (d) High-magnification micrograph of the 3D Al/ZnO coated with thin film of dense TiO$_2$. (e) Complete photoanode after infiltration and calcination of the TiO$_2$ NP paste. Reprinted with permission from ref 234. Copyright 2011 American Chemical Society.

exciton diffusion length. By constructing bulk or dispersed heterojunction cells, the donor and acceptor are separated at nanoscale and the exciton can reach the interface before undergoing deactivation.

In this section, we mainly address recent advances of bulk and dispersed structures and provide progress in morphology control and interface engineering. For more reviews of polymer-inorganic hybrid devices see refs 237–241.

3.2. Devices Based on Nanoporous TiO$_2$

The nanoporous TiO$_2$ layers, which have been commonly used in DSCs, are combined with conjugated polymers to fabricate bulk heterojunction solar cells in the past decade.[242–248] The first study reported the bulk heterojunction devices based on TiO$_2$ films by sintering isotropic, colloidal TiO$_2$ NPs into a connected thin film.[242] Further study proposed mesoporous titania films with pore size less than 10 nm to fabricate

absorbed by the polymer and creates excitons. The generated excitons dissociate into separate charges in the vicinity of the hybrid interface and then inject free holes and electrons into the polymer and the inorganic semiconductor. Following charge separation, the electrons and holes travel through the direct or percolating pathway and finally are extracted by the relevant electrodes to generate photocurrent. As the diffusion length of excitons in many polymer films is typically less than 10 nm,[235,236] high photocurrent quantum efficiency requires a high probability of exciton generated within the distance of

nanoporous TiO$_2$ hybrid solar cells in conjunction with conjugated polymer poly-3-hexylthiophene (P3HT).[243] The small pore size results in sufficient exciton dissociation and the interconnected TiO$_2$ particles provide continuous pathways for electrons transport, yielding a remarkable efficiency of 1.5%.

In nanostructured polymer-inorganic hybrid solar cells, the surface engineering of the TiO$_2$ nanocrystal film is an important approach for improving the device performance. Modification of the TiO$_2$ surface with organic molecules has been reported to induce dipole at the polymer/TiO$_2$ interface.[246,249,250] Consequently, the energy offset at the polymer/TiO$_2$ interface and thus the V_{oc} can be tuned by employing interfacial molecules with various dipoles. Besides influencing the energy alignment at the donor/acceptor interface, the interfacial molecules can also modify the physical and chemical properties of the interface, thus blocking or mediating forward charge transfer or reducing back charge recombination.[246,247,250] In bilayer devices, the improvement of device performance upon interfacial molecule modification can be mainly attributed to the optimized polymer/TiO$_2$ interface, because the absorption of monolayer molecules is negligible. However, in nanostructured polymer-inorganic hybrid solar cells, dye molecules used for interface modification can also act as light harvester, contributing to light absorption and charge generation. In 2009, Ramakrishna and co-workers[244] reported a highly efficient hybrid device based on mesoporous TiO$_2$ films, in which the metal-free organic dye (D102) and the ruthenium dye (N719) were used to modify the TiO$_2$ NP surface. In their work, the surface treatment of dye-modified TiO$_2$ films by using lithium bis(trifluoromethylsulfonyl)imide (Li(CF$_3$SO$_2$)$_2$N) and TBP prior to the deposition of the P3HT layer resulted in a nearly 60-fold improvement of device efficiency for D102-based devices, achieving a high efficiency of 2.63% under AM 1.5 full sunlight. In contrast, almost no enhancement was obtained with the treatment for N719-based devices. The effect of TBP and lithium salt treatment on device performance is strongly dependent upon the nature of the dye, and this effect is attributed to the variation of the energy level of the sensitizers as illustrated in Figure 26b. As the N719 sensitizer possesses a lower LUMO level than that of P3HT, the electron transport is facilitated from the LUMO of P3HT to the CB of TiO$_2$. Therefore, the N719 molecule at the hybrid interface acts as an energy funnel to improve the electron injection efficiency and this procedure is referred to as the "electron-mediating" mechanism. In this case, almost no variation of energy level and thus no improvement are obtained by Li salt and TBP treatment. For D102 modifier, the surface treatment leads to obvious downward movement of both HOMO and LUMO energy levels, inducing both "dye regenerating" and "electron-mediating" mechanisms in the device. As shown in Figure 26c, the device based on D102 with Li salt and TBP treatment exhibits the highest IPCE value of ∼40% at around 480 nm. The surface modification effect of nanoporous TiO$_2$ with a class of conjugated cyanoacrylic acids (WL-1 to WL-4) were systematically studied by Yu et al.[246] The utilization of cyanoacrylic acid as a terminal anchoring group increases the electron affinity in regions close to titania surface, posing a positive effect on J_{sc}. Moreover, the generated molecular dipole directing away from the titania surface induces the increment of V_{oc}. The LUMO of interfacial molecules can be tuned by lengthening the conjugation length or adopting a donor–acceptor structure, which may significantly affect the dissoci-
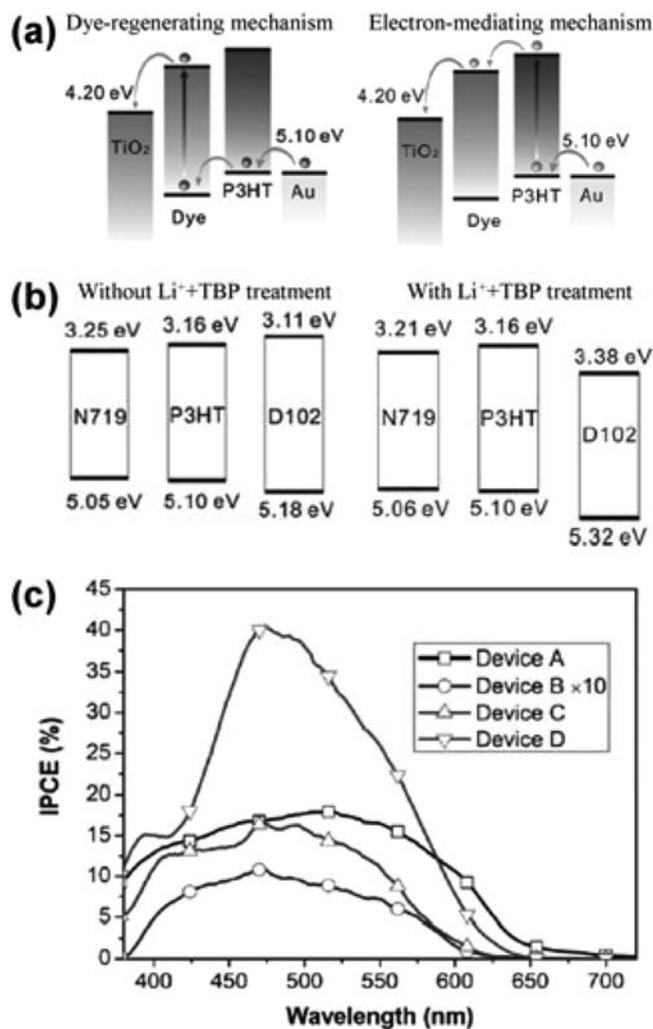
Figure 26. (a) "Dye-regenerating" and "electron-mediating" mechanisms for the dye-modified P3HT-TiO$_2$ hybrid solar cells. (b) HOMO and LUMO energy levels of N719 and D102 on TiO$_2$ films in different conditions. (c) The corresponding IPCE of different devices. Devices A and C are based on N719 dye and devices B and D are based on D102 dye. Devices A and B are fabricated without Li salt and TBP treatment, while the dye modified TiO$_2$ films in devices C and D are treated by Li salt and TBP prior to P3HT deposition. Reprinted with permission from ref 244. Copyright 2009 Wiley-VCH.

ation efficiency of P3HT excitons. An impressive efficiency of 2.87% was achieved based on the WL4-modified cell.

In the above-mentioned research, the main role of the interfacial modification interlayer is to control the energy offset at the polymer/TiO$_2$ interface and influences the charge separation as well as recombination process in hybrid solar cells. However, it remains a great challenge to clearly track the effects of intermolecular processes at the mesoscopic level. Canesi et al.[247] reported a step-change improvement in the device efficiency through engineering of the hybrid interface by 4-mercaptopyridine (4-MP). The presence of 4-MP interlayer facilitates the exciton splitting and hampers the electron back transfer, leading to a significant improvement of the device performance. Besides, the migration of polymer on the TiO$_2$/4-MP substrate is easier since the local charges are smaller and the corresponding electrostatic energy landscape is smoother in the presence of 4-MP. The relatively diffusibility mobility of polymer on the TiO$_2$/4-MP substrate not only leads to

S

dx.doi.org/10.1021/cr400606n | Chem. Rev. XXXX, XXX, XXX–XXX

relatively large polymer/substrate interface area but also affects its final morphology. When 4-MP is used to functionalize the TiO$_2$ surface, the substrate results atomically flat, with much smaller atomic partial charges in the external thiol groups. Therefore, the backbone of P3HT is planar on the surface and the alkyl chains are aligned along the thiol rows as shown in Figure 27. The induced morphological order at the interface consequently leads to a strong improvement in charge generation and a decrease in recombination losses.
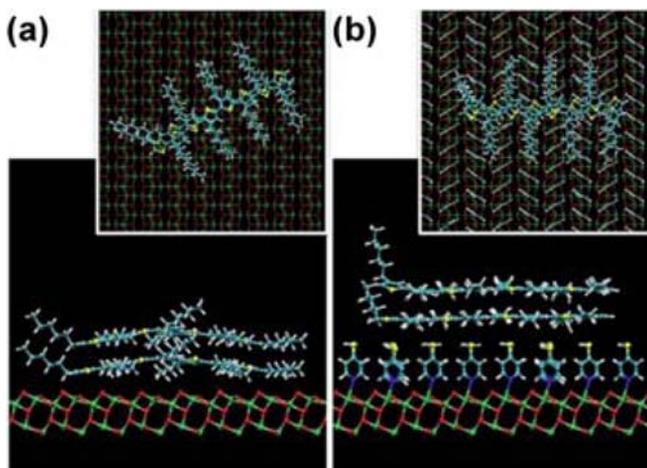
Figure 27. Side and top views of (a) TiO$_2$/P3HT interface and (b) the TiO$_2$/P3HT interface modified with 4-MP by model potential molecular dynamics simulations at room temperature. Reprinted with permission from ref 247. Copyright 2012 Royal Society of Chemistry.

3.3. Devices Based on Polymer-TiO$_2$ Blends

By blending TiO$_2$ NPs with conjugated polymers, the hybrid active layer can be processed from solution in a single step. Contrary to the incomplete infiltration of porous TiO$_2$ layers by conjugated polymers, this procedure guarantees an improved TiO$_2$-polymer compatibility at the interface. In bulk heterojunction solar cells, obtaining optimized morphology with large donor/acceptor interface area for efficient charge separation and bicontinuous percolating pathway for effective charge transport is important.

Typically, nanocrystals are synthesized chemically from solution using specific surfactants, such as trioctylphosphine oxide (TOPO)[251] or oleic acid (OA)[252] in order to disperse the hydrophilic NPs in common apolar solvents used to dissolve the conjugated polymers. However, the presence of an insulating ligand at the particle surface may hamper the charge separation at the donor/acceptor interface and reduce electron hopping rates between particles. Replacing the organic ligand at the nanocrystals surface is recognized as a sensible strategy to overcome this problem.[251−254] Bouclé et al.[251] reported the enhancement of device performance through partial replacement of the insulating TOPO ligands on the TiO$_2$ NR surface with the ruthenium dye Z907. The charge separation yield at the P3HT/TiO$_2$ interface is improved, and this effect is associated with the 3-fold increase of the device PCE under simulated solar illumination. However, the charge trapping within or between the NRs limits charge transport, resulting in poor photocurrent as well as low efficiency (0.07%) after the ligand exchange.

Chen's group[252,253] also demonstrated the enhancement of device performance by using interfacial modifications on the TiO$_2$ NR surface, which improved compatibility between the polymer and TiO$_2$ NRs, facilitated charge separation and suppressed back recombination at the interfaces of P3HT-TiO$_2$ NR hybrids. The original OA ligand on the surface of the TiO$_2$ NR is removed with three different kinds of ligand molecules of anthracene-9-carboxylic acid (ACA), tetracarboxy phthalocyanine copper(II) (CuPc-dye), and cis-bis(4,4-dicarboxy-2,2-bipyridine)dithiocyanato ruthenium(II) (N3-dye) as shown in Figure 28a. After the interfacial engineering between P3HT and TiO$_2$ NRs, both the J_{sc} and V_{oc} are improved, achieving the highest efficiency of 2.2% by replacing OA with the N3-dye molecule (Figure 28b). The attachment of effective interfacial molecules on the surface of TiO$_2$ NRs can improve the compatibility between the polymer and TiO$_2$ NRs, facilitating charge separation in the device. In addition, the back recombination at the interfaces of P3HT-TiO$_2$ NR hybrids is also suppressed as revealed by the transient V_{oc} decay measurements (Figure 28c). The enhanced charge separation efficiency and reduced interfacial recombination are related to the significant improvement in J_{sc}. Moreover, the reduced charge recombination rate may lead to increased electron and hole concentrations at interfaces, increasing the difference between the quasi-Fermi levels of electrons and holes, accounting for the observed increase in V_{oc} upon interface modifications. First-principles calculations indicated that the variation in the recombination rate at the polymer/TiO$_2$ NR interfaces modified with different interfacial molecules was likely to stem from the variation of stereohindrance effect associated with different molecular structures. Although removing the insulating ligands on nanocrystals surface with effective interfacial molecules has been proved to be an attractive approach to achieving high performance, the consequent aggregation of nanocrystals tends to hinder further efficiency improvement.

Besides properties of organic/inorganic interface, the morphological organization of the donor−acceptor blends is another parameter affecting the photocarrier dynamics of the active layers and thus the photovoltaic performance. The control of blend morphology is recognized as an important approach to improving the self-organization and phase separation. Kwong et al.[255] found that good solvent for P3HT with lower vapor pressure such as xylene led to better mixing of TiO$_2$ and P3HT. The resulting morphology featured large number of small domains, yielding large interface and improved exciton dissociation.

A simple approach was recently developed by using mixed solvent to control the morphology of P3HT-TiO$_2$ NR hybrid bulk heterojunction solar cells.[256] The transmission electron microscopy (TEM) image (Figure 29) indicates that TiO$_2$ NRs tends to aggregate into domains in the presence of chloroform solvent. By using mixed solvent consisting of pyridine, dichloromethane, and chloroform, optimized nanoscale morphology with relatively uniform dispersion of TiO$_2$ NR in the hybrid film was obtained. The presence of pyridine in the solvent induces the aggregation of P3HT into nanostructured network and facilitates the dispersion of NRs in the hybrid solution, leading to the formation of morphology with well-distributed TiO$_2$ NRs embedded in highly crystalline polymer domains. This bicontinuous phase-separated morphology can significantly improve the charge separation, transport, and
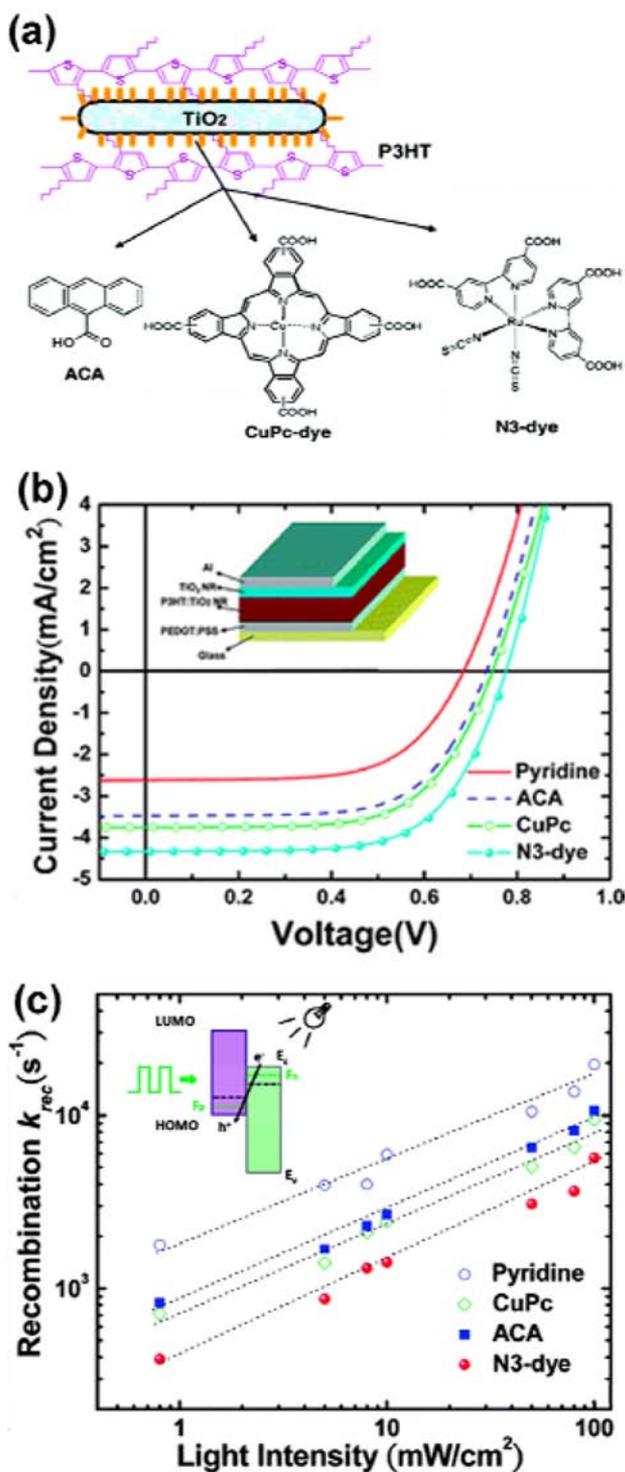
Figure 28. (a) Schematic representations of P3HT-TiO$_2$ NR hybrid after interface modification and chemical structures of different interfacial molecules of ACA, CuPc-dye, and N3-dye. (b) *J*–*V* curves of the P3HT-TiO$_2$ NR hybrid solar cells with different interface ligands. (c) The corresponding charge recombination rate constant of these devices. Reprinted with permission from ref 253. Copyright 2009 American Chemical Society.
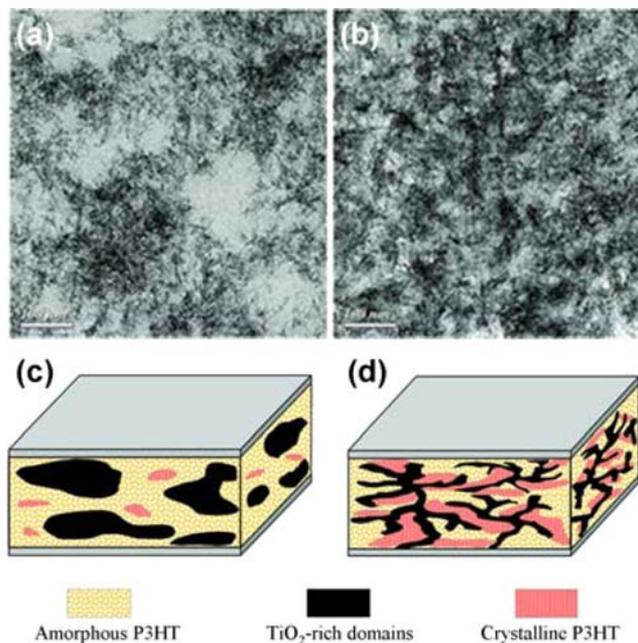
Figure 29. TEM image of P3HT-TiO$_2$ hybrid films spun from (a) chloroform and (b) mixed solvents containing pyridine. Schematic representations of the films spun from (c) chloroform and (d) mixed solvent. Reprinted with permission from ref 256. Copyright 2010 American Chemical Society.

with the nanocrystal shapes.[257−259] The 3D morphological organization of TiO$_2$ nanocrystals in P3HT was analyzed by using electron tomography based on scanning transmission electron microscopy using high-angle annular dark-field (STEM-HAADF) electron imaging.[257] As shown in Figure 30, the TiO$_2$ NPs are more homogeneously dispersed in P3HT, while TiO$_2$ NRs are found to induce significant phase separation with distinct TiO$_2$ NR rich clusters separated by P3HT domains. The 3D bulk heterojunction morphologies clearly indicate that the anisotropic TiO$_2$ NRs can largely decrease the number of junctions of a connective network, thus reducing the probability of interparticle hopping. Besides, the elongated TiO$_2$ NRs with preferred orientations angled toward the plane of the film are more likely to form a connective network between two electrodes as compared to the isotropic TiO$_2$ NPs. Despite more efficient exciton dissociation in the P3HT-TiO$_2$ NP hybrid due to relatively high intermixing, the presence of anisotropic TiO$_2$ NRs enables the establishment of a favorable 3D morphology, leading to relatively low recombination rate as well as more efficient and balanced transport of carriers in the device. The nanocrystal dimensionality also has significant impacts on the nanoscale morphology of polymers in P3HT-TiO$_2$ nanocrystal bulk heterojunctions.[258,259] As compared to P3HT-TiO$_2$ NP hybrids, the elongated and anisotropic TiO$_2$ NRs with preferred orientations angled toward the plane of the film can promote the formation of increased vertical-stacking of P3HT crystallites, providing a more effective hole transport perpendicular to the substrate. Besides, the TiO$_2$ NRs are found to effectively promote the polymer crystallinity while minimizing the number of electron hopping events required for transporting electrons, thereby facilitating electron/hole transport in the devices. Figure 31 displays the simulated 3D morphologies of P3HT-TiO$_2$ NP and NR blends prepared at a blending ratio of 1:1. Relatively to NPs, the NRs provide a better balance between

recombination kinetics, inducing significant enhanced photo-current and photovoltage.

In polymer−inorganic hybrid solar cells, nanoscale phase distribution of the donor−acceptor blends are also correlated
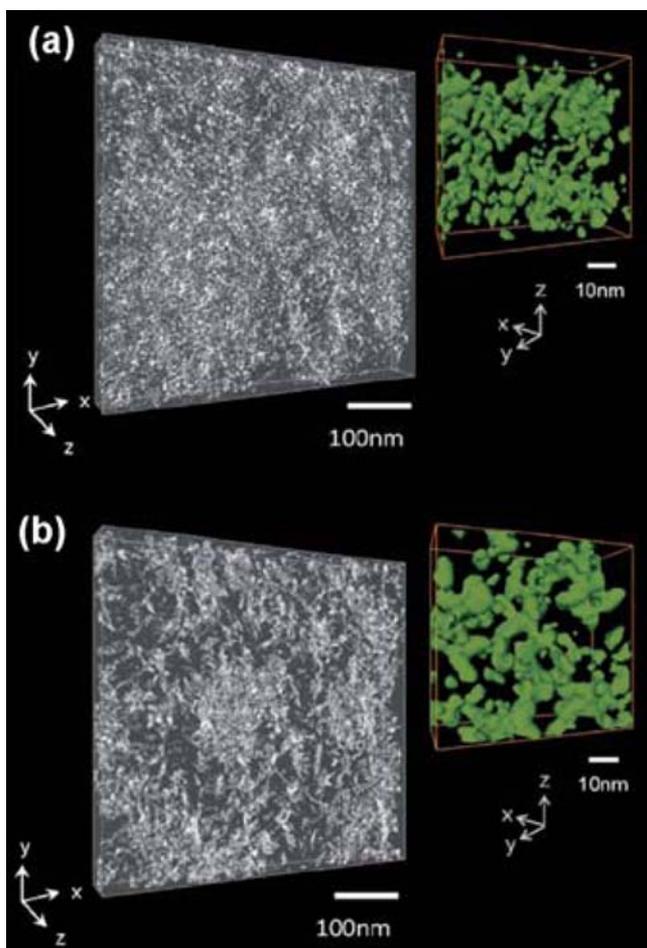
Figure 30. STEM-HAADF tomography images of (a) P3HT-TiO$_2$ NPs and (b) P3HT-TiO$_2$ NRs hybrid films respectively. The insets also show the 3D distribution of TiO$_2$ NPs or NRs along the thickness direction. Reprinted with permission from ref 257. Copyright 2011 American Chemical Society.

electron transport and exciton dissociation by promoting polymer crystallinity and minimizing the number of inter-nanocrystal junctions, while maintaining a reasonably high specific interface area for efficient exciton dissociation. These studies provide the possibility of the nanoscale morphology control of polymer−inorganic nanocrystal bulk heterojunction blends via tuning the nanocrystal shapes.

3.4. Devices Based on Nanorods and Nanotubes

During the past years, the application of 1D TiO$_2$ nanostructures has generated remarkable scientific interest.[260−262] In these devices, the conjugated polymers are infiltrated into the free space of the ordered nanostructures to form the hybrid active layers. The device architectures feature ordered assemblies and provide direct pathways for charge transport.

The first example of such devices is composed of vertical aligned TiO$_2$ NRs prepared by sol−gel process in an anodized alumina template with P3HT as the hole-conducting polymer.[260] The corresponding device shows efficiency of 0.512%, about 4-fold improvement over planar control device. Recently, Wu's group[261,262] reported hybrid solar cells consisting of the rutile TiO$_2$ NR arrays as shown in Figure 32a,b. They demonstrated that the incorporation of D149 or Z907 molecular interlayers can provide an appropriate band alignment at the P3HT/TiO$_2$ interface, thus improving the light trapping in the device. In addition to act as the photocurrent contributor, the dye molecules can also boost the compatibility and thus assisting the charge separation at the hybrid interface. The attachment of dye molecules imparts an effective recombination barrier at the P3HT/TiO$_2$ NRs interface, which can significantly enhance the electron lifetime in the TiO$_2$ NRs. 3D rutile TiO$_2$ nanodendrite arrays developed from TiO$_2$ NR arrays are further utilized to fabricated device in conjunction with P3HT.[239] As illustrated in Figure 32c,d, the nanodendrite array structure not only provides direct and ordered electron transport pathways as the 1D TiO$_2$ NR array does but also makes much larger surface area available for
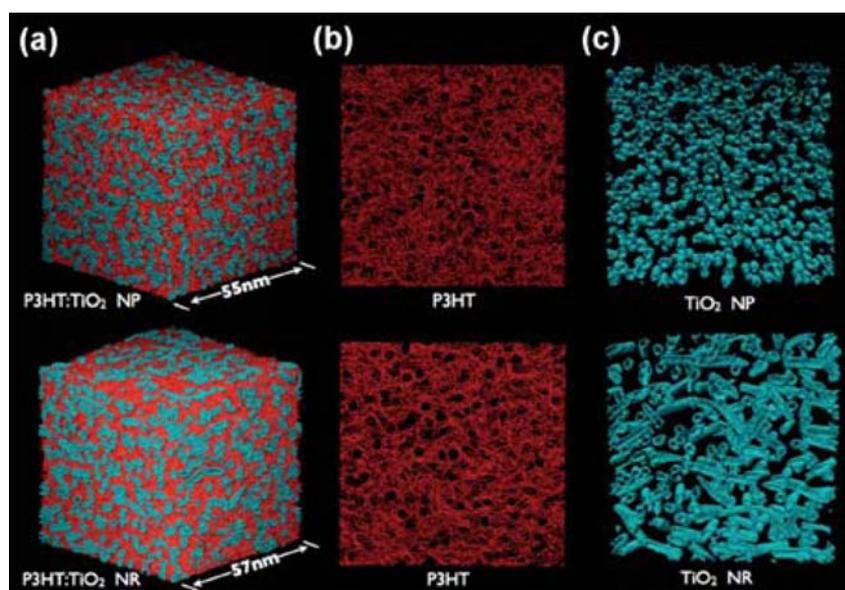
Figure 31. Coarse-grained molecular dynamics (CGMD) simulated 3D morphologies of P$_3$HT-TiO$_2$ NPs (upper panel) and NRs (lower panel) blends; P3HT chains and nanocrystals are colored red and blue, respectively. Reprinted with permission from ref 259. Copyright 2012 Royal Society of Chemistry.
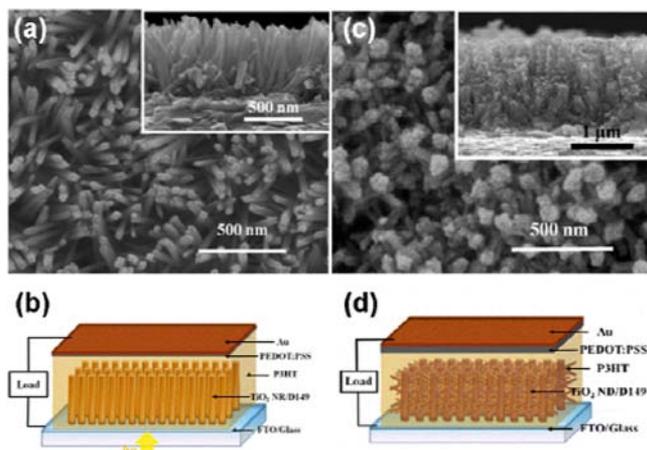
Figure 32. Top view and cross-sectional view (inset) SEM images of (a) the TiO_2 NR array and (c) the TiO_2 nanodendrite array. Schematic of (b) the D149-modified TiO_2 NR array-P3HT and (d) the D149-modified TiO_2 nanodendrite array-P3HT hybrid solar cells. Panels a and b are reprinted with permission from ref 261. Copyright 2012 American Chemical Society. Panels c and d are reprinted with permission from ref 262. Copyright 2012 American Chemical Society.

charge separation. Benefiting from the enlarged interface area, a considerably enhanced charge separation was observed and a notable efficiency of 3.12% was achieved for the D149 modified-TiO_2 nanodendrite array-P3HT hybrid solar cell as compared to the 2.63% of its NR counterpart.

Although both sensitizer and polymer may contribute to the photocurrent generation in this kind of device, the sensitizer is advised to have a minimum spectral overlap with that of the P3HT to guarantee effective transmission of the high energy photons. Grimes and co-workers[263] demonstrated a hybrid device structure comprised of TiO_2 NT arrays, which were sensitized with unsymmetrical squaraine dye (SQ-1) and uniformly infiltrated with P3HT as shown in Figure 33. The vertically oriented TiO_2 NT arrays with pore size of 20−35 nm provide large surface area for efficient charge generation and facilitate the P3HT infiltration within the tubes. In this configuration, the SQ-1 dye is used to absorb in the red and near-IR portion of solar photons while P3HT is employed for harvesting the higher energy photons. The complementary absorption bands of these two materials make them appropriate for an extended spectrum solar cell. Consequently, the device exhibited a significant enhancement of performance, achieving an efficiency of 3.8% in AM 1.5 full sunlight.

Although the ordered heterojunction provides a direct path facilitating electron transport to the collecting electrode, the poor mobility in the polymer and the resulting recombination of holes with electrons may also hinder further improvement of device performance. A strategy toward achieving high efficiency of nanostructured hybrid solar cell is to incorporate both ordered heterojunction architectures and bulk heterojunctions by forming a double heterojunction device to provide two interfaces for charge transfer. Grimes et al.[264,265] reported a double heterojunction polymer solar cells, in which a blend of P3HT and [6,6]-phenyl-C71-butyric acid methyl ester (PCBM) was infiltrated into the transparent NT array films. In this configuration, both the P3HT/TiO_2 and P3HT/PCBM interfaces provide heterojunctions for charge separation and the resulting device shows a PCE of 4.1% under AM 1.5 full sunlight.
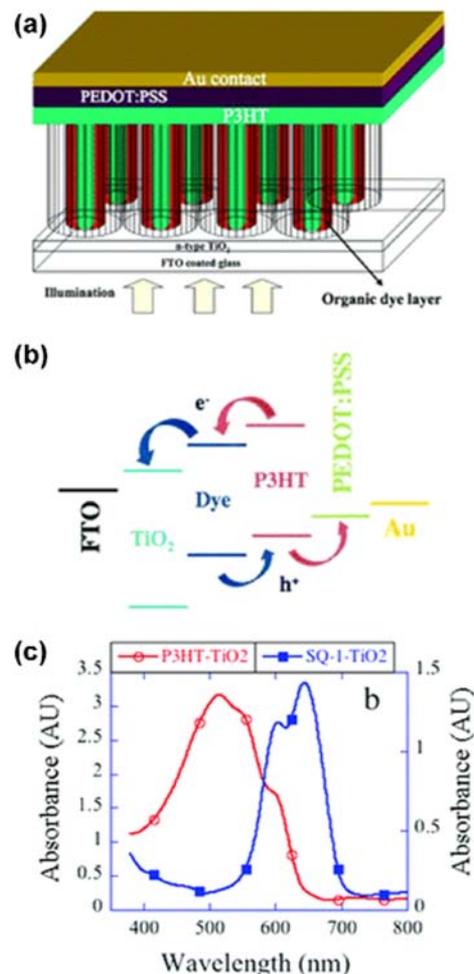
Figure 33. (a) Depiction of the nanostructured P3HT/SQ-1 dye/TiO_2 NT array hybrid solar cell. (b) Representation of energy level positions and charge transfer processes of the corresponding device. (c) Optical absorption spectra of the P3HT/TiO2 and SQ-1 dye/TiO_2 hybrid. Reprinted with permission from ref 263. Copyright 2009 American Chemical Society.

4. APPLICATION IN QUANTUM DOT-SENSITIZED SOLAR CELLS (QDSCS)

4.1. Fundamentals of QDSCs

In recent years, sensitization of metal oxide layers with quantum dots (QDs), such as CdS,[266,267] CdSe,[268−273] PbS,[274−279] Bi_2S_3,[280,281] and InP,[282] has drawn significant attention for promising photovoltaic devices. As compared with sensitizers widely employed in DSCs, the band gap of QDs can be tuned through control of the nanoparticle size, allowing one to adjust both visible response and the energetics at the interfaces of the QD with the surrounding media. Moreover, the relatively high extinction coefficients of QDs can improve the light harvesting ability of the photoanode and increase the overall efficiency of the device. The formation of multiple excitons upon the absorption of a single photon in QDs increases the thermodynamic efficiency limit of the device, making QDSCs extraordinarily attractive alternative for photo-voltaic applications.[283−287]

The operation mechanism of QDSCs is similar to that of DSCs, considering QDs in some cases as a simple alternative dye.[271,283,287−290] But surface states in QDs, not present in molecular dyes, introduce a significant difference between both

light absorbers. The difference has to be taken into account as surface states can affect the injection and recombination processes.[288,291,292] While the application of QDs as light harvester dates back to the 1990s,[280,282,293,294] it has only been in recent years when QDSCs have attracted intensive attention. Chemical bath deposition (CBD)[295] and succesive ionic layer absorption and reaction (SILAR) methods[296] are commonly used by the QDSC community for the direct deposition of QDs onto TiO$_2$ surface. The in situ synthesis of QDs on TiO$_2$ surface leads to efficient charge injection from the QD into the TiO$_2$ material. Meanwhile, these methods ensure a high QD loading of photoanodes and consequently high photocurrents, although the obtained QDs may feature a broad size distribution and low crystalline quality.[297] Presynthesized monodisperse QDs, on the other hand, are usually connected through linker molecules to the nanostructured TiO$_2$ or deposited directly without linker molecules onto the TiO$_2$ surface. However, the electron injection from the QDs to the TiO$_2$ is generally less efficient compared to directly deposited QDs. In addition, the high QD loading is difficult to attain with colloidal QDs[297] that need bifunctional molecular linkers[298,299] or especially designed direct adsorption methods.[300] Nevertheless, very recently Zhang and co-workers[272,301,302] developed a sensitization method with colloidal QDs, consisting in a capping ligand exchange followed by electrode sensitization that produced photoanodes with a high colloidal QD loading. This process has allowed the recent preparation of highly efficient devices with 6.36% PCE based on CdSe$_x$Te$_{1-x}$ alloyed QDs.[302] Further development employing core−shell QDs that utilize the charge transfer (exciplex) state has considerably improved the light absorption of QDs to longer wavelength.[303] The resulting CdTe/CdSe QD based regenerative sandwich solar cells produced the highest efficiency of this kind of solar cells, achieving 6.76% (J_{sc} = 19.59 mA cm^{-2}, V_{oc} = 606 mV, FF = 0.569) under AM 1.5 full sunlight.

4.2. Surface Treatments in QDSCs

Although the employment of QDs as light harvesters has offered the potential to prepare solar cells with excellent performance, the obtained efficiencies of QDSCs still lag behind those of DSCs. One reason for the rather moderate conversion efficiency of QDSCs is the existence of surface traps on the QDs, which act as recombination centers and increase trap mediated recombination in the device.[291,304] Besides, the charge recombination between the electrons in the TiO$_2$ and the HTMs also constitutes an important electron loss path. As a relatively large fraction of the TiO$_2$ surface is in direct contact with the HTM in QDSCs, the probability of the recombination between separated electrons and holes is higher than in DSCs.[305] A common route for passivating surface states and reducing internal charge recombination in QDSCs involves the application of a thin layer coating of wide band gap materials.[293] Besides, as most QDs suffer from photodegradation in corrosive electrolytes, passivation of the QDs surface with inorganic coatings can also enable the use of the I$^-$/I$_3^-$ containing electrolyte.[306,307] The inorganic coatings can be deposited in a conformal and continuous fashion onto TiO$_2$ electrodes, and it is shown that the semiconductor coating can improve not only the stability but also the efficiency of QDSCs.[273,306−312]

Shen and co-workers[309] demonstrated that the surface modification of QDs by ZnS coating enormously improved the performance of the CdSe QDSCs. As the surface states of CdSe are passivated by the formation of ZnS layer on its surface, the surface trapping of photoexcited electrons and holes in the QDs is effectively suppressed. Upon ZnS modification, the photoexcited electrons are injected more efficiently from CdSe QDs to the TiO$_2$ CB. Since the ZnS features a larger band gap than CdSe, the ZnS coating can further create a potential barrier at the CdSe/electrolyte interface. As a result, the electron recombination from the CdSe QDs to the electrolyte is inhibited by application of ZnS surface coatings over CdSe QDs. The QDSCs with ZnS modified photoanode exhibited significantly improved J_{sc}, V_{oc}, and PCE, obtaining an optimum efficiency of 2.02% under the AM 1.5 full sunlight.

In addition to ZnS, the passivation of CdS QDSCs with a thin layer of TiO$_2$ also greatly improves the performance and photostability of the solar cells.[307] The TiO$_2$ coating passivates the CdS QD surface by decreasing the trap density and prevents its direct contact with the redox electrolyte. As the conduction band edge of the amorphous TiO$_2$ shell is located closer to the vacuum level compared to its nanocrystalline counterpart, the TiO$_2$ coating can be considered as a potential barrier at the nanocrystalline TiO$_2$/electrolyte interface for electron transfer from the nanocrystalline TiO$_2$ core into the electrolyte. Therefore, all five possible recombination paths in the uncoated system are blocked through the amorphous TiO$_2$ coating as shown in Figure 34. The relatively higher conduction band edge of the amorphous TiO$_2$ shell also induces a barrier at the CdS/electrolyte interface, thus hindering the electron injection from the excited CdS QDs into electrolyte. In addition, the amorphous TiO$_2$ coating protects the CdS QDs from the attack of the corrosive I$^-$/I$_3^-$ redox couple, allowing the use of highly efficient iodide-based electrolyte in QDSCs.
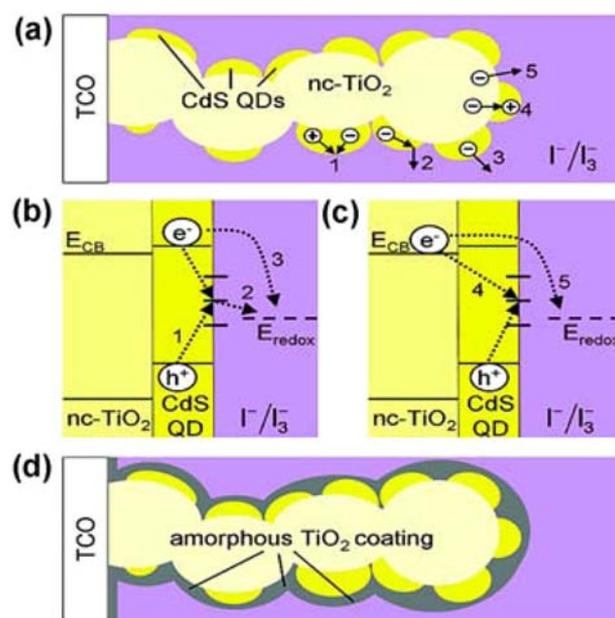
Figure 34. (a) Schematic drawing of the uncoated CdS sensitized TiO$_2$ electrode showing five different recombination paths. (b) Recombination paths of an exited electron in the CdS QD. (c) Recombination of electrons from the TiO$_2$ with a hole in a CdS surface state or in the electrolyte. (d) Schematic drawing of the CdS sensitized mesoporous TiO$_2$ electrode with amorphous TiO$_2$ coating. Reprinted with permission from ref 307. Copyright 2009 American Chemical Society.

The obtained device with TiO_2 protective shell and the I^-/I_3^- electrolyte exhibited a significant improvement of all cell parameters, obtaining a PCE of 1.24%. In addition, this TiO_2 coating is recently used also as an anchoring base for a second sensitizer to construct the new bisensitizer layer cell.[313] The new configuration allows both the electron injection from the outer absorber and fast hole extraction from the inner sensitizing layer, leading to a 250% increase in efficiency compared to a QD monolayer cell.

Although the coating of wide band gap materials over photoanode can passivate the surface states and suppress the charge recombination in the device, a thick passivation layer may also hinder the hole tunneling and result in poor charge transfer. Therefore, effective control of the TiO_2 layer thickness is crucial for further device performance optimization. Atomic layer deposition (ALD) technique, which can ultrafinely control the coating thickness, was recently employed to prepare an ultrathin protection layer of TiO_2 on the surface of CdS QDSCs.[306] It was found that the ALD-TiO_2 layer slowed down charge recombination and protected the QDs from the photocorrosion of the I^-/I_3^- electrolyte. Systematic investigation of QDSCs with different TiO_2 coating thicknesses indicated that ~2 nm ALD-TiO_2 layer can best promote solar cell efficiency by balancing the protection effect and the charge transfer efficiency. The correspondent CdS QDSC obtained a power efficiency of 1.41% and stability of 20 min under full sun illumination.

In QDSCs, the recombination processes occur in parallel at the TiO_2/QDs/electrolyte triple junction constitute one of the major limitations for further photovoltaic improvement. While the electron recombination from the TiO_2 or QDs to the electrolyte are commonly inhibited by application of surface coatings over QDs, few researches address the recombination at the TiO_2/QDs interface. Recently, the charge recombination at the TiO_2/QDs/electrolyte triple junction was investigated by isolating the different interfaces of the photoanode with respect to the electrolyte (Figure 35a).[311] As shown in Figure 35b, the J_{sc} exhibits moderate enhancement when intermediate MgO coating is applied on the mesoporous films prior to CdSe deposition or when the MgO coating is used after CdSe QD deposition. For CdSe QDSCs employing both intermediate and upper coatings, the J_{sc} significantly increased from 9.3 to 12.4 mA cm^{-2}, while the photovoltage remained nearly unchanged. The electron lifetimes derived from transient photovoltage measurements showed that the solar cell with both coatings exhibited the longest electron lifetime while the devices with the upper or intermediate coatings featured moderate electron lifetime (Figure 35c). The measured electron lifetime is in excellent agreement with the photocurrents of different cells, indicating that the high photocurrents obtained for the coated electrodes originated from suppressed charge recombination. Moreover, the greatly enhanced photocurrent and the prolonged electron lifetime of QDSCs with both coatings reveal that the recombination occurs at the TiO_2/QDs interface is as important as the other interfaces in the TiO_2/QDs/electrolyte triple junction. By using double layer MgO coating prior and after CdSe QDs deposition, the charge recombination is largely suppressed and more than 20% improvement in cell efficiency is achieved.

Besides increasing recombination resistance by surface modification with inorganic coatings, the band alignment at the TiO_2/QDs/electrolyte interfaces and the corresponding charge transfer processes can also be optimized through
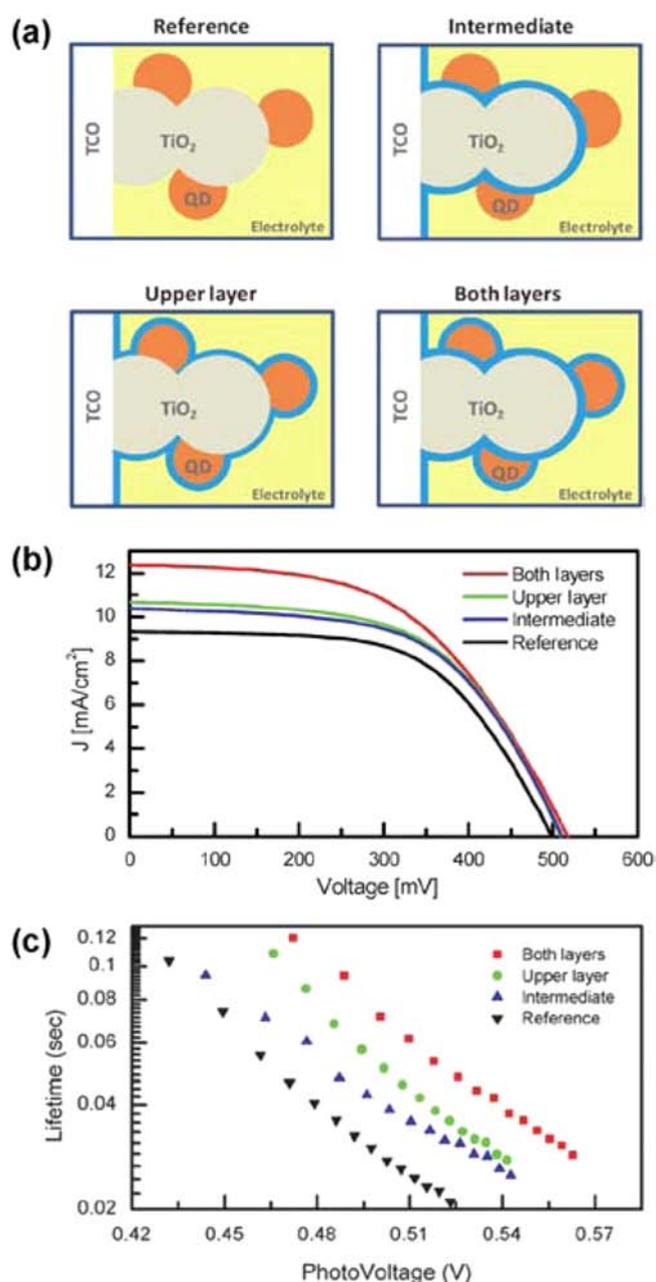
Figure 35. (a) Schematic drawing of QDSCs showing the four different types of photoanode. Corresponding (b) $J-V$ characteristics and (c) transport time constants for QDSCs incorporating different photoanodes. Reprinted with permission from ref 311. Copyright 2013 Royal Society of Chemistry.

introducing specific additives to the electrolyte or HTM. It was demonstrated that the self-assembly monolayer of an appropriate molecule onto the TiO_2 surface can induce a local dipole field and thereby tailoring an energy alignment displacement at the TiO_2/QD/electrolyte (or HTM) interfaces.[308,314,315] The modification of CdS QD surface by using benzenethiol derivatives with a negative dipole upward shifts the energy level of the QDs, while a positive dipole causes a downward movement of the QD energy level.[314] In addition, molecular dipole treatment constitutes an additional energy barrier for recombination, thus hindering the leakage of electrons in the device.[308,315] Through appropriate surface modification of CdSe sensitized electrodes with conformal ZnS

Y

dx.doi.org/10.1021/cr400606n | Chem. Rev. XXXX, XXX, XXX−XXX

coating and 4-methoxybenzenethiol molecule, both the electron injection and recombination processes can be optimized, achieving ∼600% enhancement of the efficiency for CdSe QDSSCs.[308]

4.3. Nanostructured TiO$_2$ Electrodes for QDSCs

In conventional TiO$_2$ NP-based QDSCs, electrons have to travel through a 3D network of NPs and the undesirable loss of electrons at grain boundaries impedes effective electron collection to the electrode. To address this problem, 1D nanostructured TiO$_2$ has been exploited to increase the electron mobility and charge collection efficiency.[266,267,269,316-318] Comparisons between photoelectrochemical behavior of NT array and NP-based QDSCs reveal that the NT array photoanode exhibits relatively high IPCE owing to both the increased efficiency of charge separation and the facilitated electron transport through TiO$_2$ NTs.[269] The electronic coupling between QDs and TiO$_2$ NT was investigated by using hybrid DFT approach.[319] It was found that the adsorbate states were introduced in the band gap of the TiO$_2$ NT upon adsorption of CdS QDs on the TiO$_2$ NT surface and the electron was transferred from the sulfur atoms of the CdS QDs to the CB of the TiO$_2$ upon adsorption of visible light. The photoexcited electrons could transport along the cylindrical ultrathin wall of the TiO$_2$ NT through titanium d$_{x^2-y^2}$ and d$_{z^2}$ orbits, and the TiO$_2$ NT offers a 1D directional pathway for electron transport across the substrate. Besides TiO$_2$ NT arrays, the TiO$_2$ fibers has also been investigated for the QDSC applications.[320-323] TiO$_2$ fibers can be produced in a easy way,[320] and with the appropriated surface treatments have shown an enormous potential for the development of high performance QDSCs, especially for the high V_{oc} obtained with this structures.[321]

Mesoporous inverse opal (IO) TiO$_2$ has been proposed as a novel approach to improving the performance of QDSCs, due to the fact that its large interconnected pores facilitate the infiltration of both light harvesters and hole transporting material throughout the TiO$_2$ film. This structure can also enhance the absorbance of QDs to achieve efficient light harvesting due to the slowing of group velocity of photon at the wavelength near the photonic band gap.[324-327] Diguna et al.[324,325] reported the application of TiO$_2$ IO in QDSCs and the conversion efficiency was significantly improved with surface modification of ZnS and fluoride ions.

5. APPLICATION IN INORGANIC SOLID-STATE SOLAR CELLS

The concept of inorganic solid-state solar cells is similar to the solid-state DSCs, in which the TiO$_2$ extracts photoexcited electrons generated in the absorber layer while the sensitizers are replaced by an extremely thin layer of semiconductor such as CuInS$_2$,[328-335] CdTe,[336-338] or Sb$_2$S$_3$.[339-344] The inorganic solid-state solar cells have the advantage of enhanced light harvesting and are desirable to obviate leakage, sealing, and degradation concerns in conventional DSCs.

The inorganic solid-state solar cells based on interpenetrating networks of TiO$_2$ and CuInS$_2$ (CIS) is a relatively recent inorganic-based design in this field.[328-335] Compared to a planar device, this configuration significantly shortens the average carrier diffusion length, thus improving the collection efficiency and providing device with a higher tolerance to the presence of impurities. In the TiO$_2$−CIS inorganic solid-state solar cells, an In$_2$S$_3$ buffer layer is typically required between the

TiO$_2$ and CIS layers to control the interfacial properties.[329,335] As the CBs of In$_2$S$_3$ and CIS are close together and have an offset of about 1 eV when compared to the conduction band energy of anatase TiO$_2$, the photogenerated electrons can be easily transferred across the CIS/In$_2$S$_3$ interface to the TiO$_2$. Moreover, the recombination of conduction band electrons of TiO$_2$ with valence band holes in CIS can be limited due to the expanded spatial distance of CIS and TiO$_2$ (Figure 36). As the
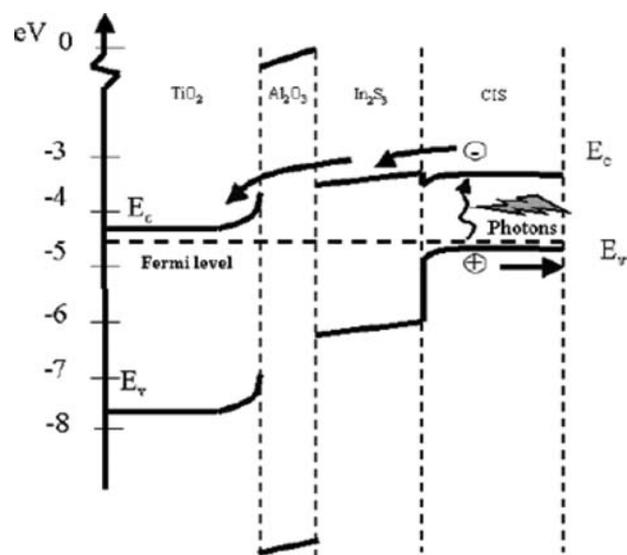
Figure 36. Energy-band diagram of a TCO/TiO$_2$/Al$_2$O$_3$/In$_2$S$_3$/CIS solar cell. Reprinted with permission from ref 329. Copyright 2004 Wiley-VCH.

deposition of sulfide absorber layers on TiO$_2$ leads to surface states in the forbidden gap of TiO$_2$, a thin buffer layer of Al$_2$O$_3$ is further used to passivate the surface and improved the photovoltaic performance of the device.

In addition to the interfacial properties, the TiO$_2$ film nanostructure, particularly the TiO$_2$ particle size and layer thickness also have great influence on the photovoltaic performance.[332,333] The device efficiency was enhanced dramatically with increasing particle size, from 0.2% for the 9 nm TiO$_2$ nanoparticles to 2.8% for the 300 nm counterpart.[332] It was shown that larger TiO$_2$ particles led to better photovoltaic performance due to decreased charge transport resistance. Furthermore, the larger TiO$_2$ particles may also lead to enhanced photon absorption and decreased carrier-migration distance owing to enhanced light trapping and better infiltration of the CIS overlayer into the TiO$_2$ matrix, thus secondarily improving the device performance.

Besides CIS, another sensitizer material that attracts huge interest is Sb$_2$S$_3$. There are several examples of inorganic solid-state solar cells based on nanostructured TiO$_2$ sensitized with Sb$_2$S$_3$ employing different HTMs such as CuSCN,[339-341] conducting polymers,[342,343] and organic blend.[344] Sb$_2$S$_3$-based cells prepared with nanostructured TiO$_2$ was compared with analogous device with flat configuration.[343] It was found that decreasing the effective surface area toward the limit of flat samples increased the V_{oc} while providing a significant photocurrent. This V_{oc} enhancement is attributed to the reduction of the recombination rate. However, the reduction of the surface area impedes the screening and results in increased hole-transport resistance, thus adversely affecting the cell fill factor. Therefore, an optimized TiO$_2$ structure has to balance the

Z

dx.doi.org/10.1021/cr400606n | *Chem. Rev.* XXXX, XXX, XXX−XXX

between the reduced recombination with the need of effective surface area for increasing the light absorption and screening effect.

6. APPLICATION IN PEROVSKITE SOLAR CELLS

Some lead iodide perovskites, which feature direct band gap, large absorption coefficient, and high carrier mobility, have attracted attention as a new class of light harvesters in heterojunction solar cells.[345−355] The optical and electronic properties of perovskites can be tuned to a great extent by controlling the distance and the electronic coupling between the inorganic sheets according to the structure of the organic component employed. In just a few years, this newly developed device has made a series of remarkable progresses and achieved an unprecedented PCE of 15.4% under AM 1.5 full sunlight.[356]

Miyasaka et al.[357] have pioneered the photovoltaic function of $CH_3NH_3PbI_3$ and $CH_3NH_3PbBr_3$ perovskites self-organized on TiO_2 as n-type semiconductors and obtained an efficiency of 3.8% in combination with iodide-based electrolyte. Further optimization of the $CH_3NH_3PbI_3$ solution concentration and postannealing temperature yields optimized PCE of 6.54%, which is almost two times higher than that of a conventional N719-based cell.[358] Unfortunately, a rapid degradation of performance is observed due to the dissolution of the perovskite in iodide-containing liquid electrolyte. As the $(CH_3NH_3)PbI_3$ perovskite features higher absorption coefficient than conventional sensitizers in DSCs, it is sensible to use perovskite in solid-state cell where much thinner TiO_2 layer is employed than in liquid junction devices.

A solid-state solar cell employing $(CH_3NH_3)PbI_3$ as light harvester and spiro-MeOTAD as hole-conductor has been reported by Park's and Grätzel's groups,[359] where a PCE of 9.7% was achieved based on a very thin TiO_2 film ($\sim$0.5 μm). The valence band energy and conduction band energy of $(CH_3NH_3)PbI_3$ were estimated to be −5.43 and −3.93 eV below vacuum, guaranteeing well aligned band positions for charge separation (Figure 37b). Further femtosecond transient
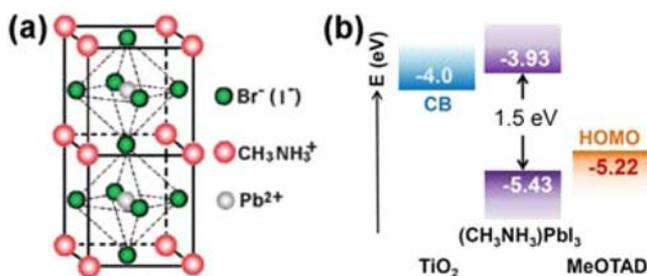
Figure 37. (a) Structure of $CH_3NH_3PbX_3$ (X = I, Br) perovskites. Reprinted with permission from ref 351. Copyright 2013 Royal Society of Chemistry. (b) Schematic energy level diagram of TiO_2/$CH_3NH_3PbI_3$/spiro-MeOTAD junction. Reprinted with permission from ref 359. Copyright 2012 Nature Publishing Group.

absorption studies demonstrated that the excited state of the $(CH_3NH_3)PbI_3$ perovskite can be reductively quenched by spiro-MeOTAD, confirming the charge separation to proceed via hole injection from the excited $(CH_3NH_3)PbI_3$ into the spiro-MeOTAD followed by electron transfer to the mesoscopic TiO_2 film.

In 2013, Snaith et al.[360] reported the application of $CH_3NH_3PbI_2Cl$ as a light harvester for mesocopic Al_2O_3 films and obtained 10.9% PCE with spiro-MeOTAD as

HTM. While similar hole transfer from lead iodide perovskite to spiro-MeOTAD is observed for this system, the photoexcited electrons are not injected into Al_2O_3 due to the mismatch in energy level between the CB of Al_2O_3 and lead iodide perovskite. In this case, the Al_2O_3 acts only as a "scaffold" and the perovskite layer functions not only as light harvester but also as n-type component, transporting electrons out of the device (Figure 38). Small-perturbation transient photocurrent decay measurements revealed shorter electron transport lifetime through the perovskite phase than through the TiO_2, indicating that the perovskite exhibited superior electron transport property than TiO_2. A noteworthy feature of the Al_2O_3-based devices is their superior V_{oc} over that of TiO_2-based devices. It is assumed that for mesoporous TiO_2 the electrons are trapped mainly in TiO_2 surface states and the electron quasi-Fermi level locates far from the CB while for Al_2O_3-based devices, in which the electrons are forced to reside in the perovskite, the electron quasi-Fermi level is lifted for the same charge density. As the V_{oc} is directly related to the splitting of hole and electron quasi-Fermi levels, this upward movement of the electron quasi-Fermi level leads to enhanced photovoltage for Al_2O_3-based device. Although giving an understandable explanation to the interesting phenomenon, this view is not consistent with subsequent results of Bisquert and co-worker.[361] As will be mentioned below, the study of Bisquert et al. indicated that charge accumulated mainly in $CH_3NH_3PbI_3$ perovskite, no matter it was coated on TiO_2 or on an insulator material (ZrO_2). While further work is still needed to clarify the origin of the enhanced photovoltage, the morphology and surface state variations of lead iodide perovskites on different metal oxides may also contribute to the different photovoltaic performance. Snaith et al.[362] further reported efficient perovskite ($CH_3NH_3PbI_{3−x}Cl_x$)-polymer hybrid solar cells with the highest efficiency of 11.7% by using a mesoporous titania film functionalized with the fullerene ($C_{60}SAM$) self-assembled monolayer. While the photoexcitations in both the perovskite and the polymer P3HT undergo very efficient electron transfer to the $C_{60}SAM$, the presence of $C_{60}SAM$ inhibits further electron transfer into the TiO_2 mesostructure due to energy level misalignment and poor electronic coupling. In this case, the electrons are trapped on the $C_{60}SAM$ molecules, through which they can be mediated into the perovskite CB and then transport across the perovskite absorber. Since the existence of sub-bandgap states on TiO_2, the inhibition of electron transfer into the TiO_2 can reduce the chemical capacitance in the device, thus moving the electron quasi-Fermi level closer to the perovskite CB at certain charge density.

Besides light harvesting and electron transportation, the hole-transport ability of perovskite is also revealed in several publications.[363,364] A layered sandwich-type architecture based on a bicontinuous 3D nanocomposite of mesoporous TiO_2 in combination with $CH_3NH_3PbI_3$ perovskite and polytriarylamine (PTAA) was introduced by Grätzel et al.[364] As the high-molecular-weight polymer PTAA cannot easily infiltrate into mesoporous TiO_2 as the small molecular HTMs, the device based on PTAA forms a pillared structure (Figure 39). In this architecture, the $CH_3NH_3PbI_3$ perovskite acts both as light harvester and hole conductor. The small $CH_3NH_3PbI_3$ crystalline domains, which densely forms on top of the mesoporous TiO_2 and the bicontinuous structure of the TiO_2/$CH_3NH_3PbI_3$ nanocomposite ensure effective extraction of the charge carriers, while the large interfacial area between
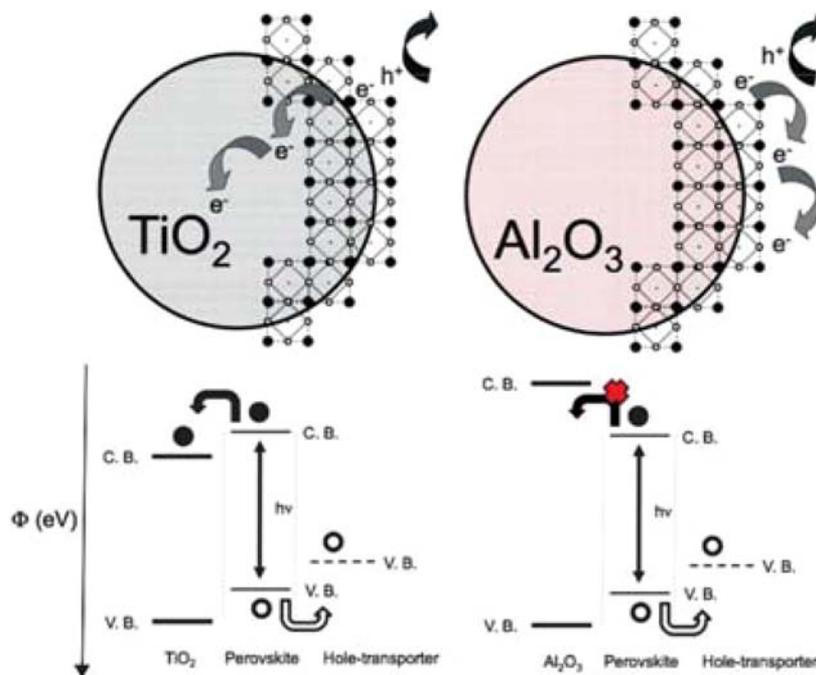
Figure 38. Schematic illustrating the charge transfer and charge transport in a perovskite thin-absorber solar cells based on TiO_2 and Al_2O_3. Reprinted with permission from ref 360. Copyright 2012 AAAS.

the $CH_3NH_3PbI_3$ and PTAA assists in hole extraction to the gold electrode. The application of PTAA is recognized as a key factor for obtaining excellent performance and the corresponding device yields a PCE of 12.0% under AM 1.5 full sunlight.

Generally, the $CH_3NH_3PbX_3$ (X = Br, I) perovskites are deposited onto mesoporous metal oxide films by simultaneously dissolving PbX_2 and CH_3NH_3X in a common solvent. However, the uncontrolled precipitation of the perovskite produces large morphological variations, resulting in a widespread of photovoltaic performance in the resulting devices. Recently, a sequential deposition method for the formation of $CH_3NH_3PbI_3$ within the porous TiO_2 film has been reported by Grätzel's group.[365] In their research, the PbI_2 was first introduced from solution into a nanoporous TiO_2 film and subsequently transformed into the perovskite by exposing it to a solution of CH_3NH_3I. Based on this technique, an unprecedented PCE of 15% has been achieved and the reproducibility of device performance is greatly improved. As the diffusion lengths in $CH_3NH_3PbI_{3-x}Cl_x$ were determined to be greater than 1 μm, which was an order of magnitude greater than the absorption depth, the nanostructuring is not necessary to achieve high efficiencies with these specific perovskite thin-absorber solar cells.[366] Based on the simplest planar configuration incorporating vapor-deposited $CH_3NH_3PbI_{3-x}Cl_x$ perovskite as the absorbing layer, a high efficiency of 15.4% was achieved under the AM 1.5 full sunlight.[356] Zhang et al.[367] successfully developed a strategy for incorporating core−shell $Au@SiO_2$ nanoparticles into organometal halide perovskite solar cells to reduce the exciton binding energy of perovskite absorber, and hence enhancing the generation of free charge carriers. Moreover, the cobalt(III) complex (FK209) was introduced as a p-dopant to improve the charge transport properties of spiro-MeOTAD.[368] Due to the reduced carrier recombination and decreased Fermi level of HTM upon the addition of FK209 and the synergistic effect between the cobalt(III) complex and LiTFSI in conjunction with spiro-

OMeTAD, the performance of the fabricated solar cell was effectively improved, achiving a PCE of 10.4% under standard solar conditions.

Although the working principle of perovskite thin-absorber solar cells is still not well understood, the tentative researches imply that this kind of cell do not work as conventional photovoltaic devices.[355,360,363,364] Bisquert and co-workers[361] investigated the mechanism of carrier accumulation in perovskite thin-absorber solar cells by means of EIS. By measuring the capacitance extracted from EIS measurements for both nanostructured TiO_2 and ZrO_2 electrodes, significant higher capacitances were observed for samples with perovskite, despite the large difference from the electrical point view between TiO_2 and ZrO_2. This phenomenon indicates that the charge accumulation mainly occurs in light-absorbing materials, $CH_3NH_3PbI_3$ perovskite in nanostructured devices. In this respect, the distribution of surface states on perovskite may have significant impact on the photovoltage of the device, although there is not a clear recognition of photovoltage origins in these devices until now. Besides, whether the charge recombination is intensified by the accumulation of electrons in perovskite materials and the intrinsic principles for its high efficiency remain an open question to be answered in the future.

7. CONCLUDING REMARKS

Over the past decades, titanium dioxide nanomaterials have been intensively studied for their application in solar to electricity conversion because of their compatibility with modern technologies. The continuous breakthroughs in the synthesis and modifications of titanium dioxide nanomaterials have brought novel properties and applications in the photovoltaic filed with improved performance. Besides, newly developed devices based on a novel concept have largely expanded the application range of titanium dioxide and also raised new requirements for titanium dioxide properties. In this
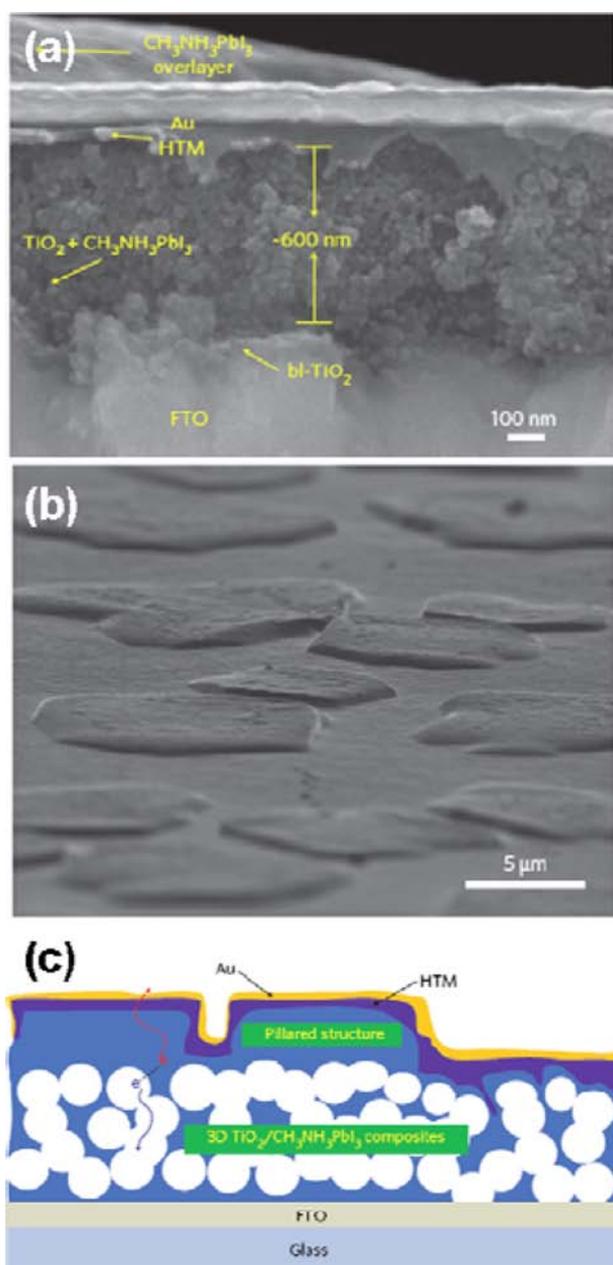
Figure 39. (a) SEM cross-sectional image, (b) SEM surface image, and (c) architectural schematic of the inorganic−organic hybrid heterojunction solar cell consisting of $CH_3NH_3PbI_3$-coated mesoporous TiO_2 film as well as PTAA hole conductor. Reprinted with permission from ref 364. Copyright 2013 Nature Publishing Group.

review, the major advances of applying titanium dioxide nanomaterials to photovoltaics have been discussed, including the dye-sensitized solar cells, polymer-inorganic hybrid solar cells, quantum dot-sensitized solar cells, inorganic solid-state solar cells, and perovskite solar cells. These steady progresses have demonstrated that TiO_2 nanomaterials play an important role in the search for efficient and low cost photovoltaic technologies. In these photovoltaic devices, the charge transfer process is intimately associated with the properties of titanium dioxide nanomaterials as well as the titanium dioxide interface. While the unique physical and chemical properties of titanium dioxide nanomaterials can be controlled through modulation of nanocrystal structure, size, shape, and organization, the

properties of titanium dioxide interface can be modulated through the interaction between TiO_2 and the surrounding elements, including light harvesters, charge transport materials, additives as well as interfacial modifiers. By rational modulation of the intrinsic and interfacial properties of the TiO_2 nanomaterials, people have made great progress in controlling the light harvesting, energy distribution, charge separation, charge transfer and transport properties in the devices and have greatly boosted the performance of the devices. Besides these fundamental achievements, more effort should be taken to develop large scale preparation technique for high quality, low cost titanium dioxide nanomaterials and transformative technology so as to realize the marketing economically viable solar panels with wide application prospect.

Recently, perovskites have attracted great attention as a new class of light harvesters for mesososcopic solar cells. This newly emerged solar cell has made remarkable progresses and achieved an impressive PCE of 15.4% in just a few years. Although the full device stability over a broad range of conditions remains to be proved, lead iodide perovskites have opened up a new era for developing efficient and low-cost solar cells. It is believed that future research efforts on new materials and key interfaces will make the titania-based solar cells as a new PV energy source.

AUTHOR INFORMATION

Corresponding Author

*E-mail: peng.wang@ciac.jl.cn.

Notes

The authors declare no competing financial interest.

Biographies

Yu Bai obtained her Ph.D. in Chemistry from the Chinese Academy of Sciences in 2011 and is now a professor at Harbin Institute of Technology. Her research interest focuses on interfacial physical chemistries of dye-sensitized solar cells as well as novel inorganic nanostructures and hole-transport materials for energy storage and conversion. She has received the 2009 GUCAS-BHP Billiton award and the 2012 CAS president special award.

Iván Mora-Seró obtained his Ph.D. in Physics from the Universitat de València in 2004. Currently, he is an associate professor at the Department of Applied Physics, Universitat Jaume I de Castelló, and is leading the quantum dot and semiconductor research line of the photovoltaic and optoelectronic devices group. His recent research has largely focused on new concepts for photovoltaic conversion based on nanoscaled devices and semiconductor materials following two main lines: quantum dot solar cells, with especial attention to sensitized devices, and lead halide perovskite solar cells.

Filippo De Angelis is a senior research scientist and deputy director at the CNR Institute of Molecular Sciences and Technology, in Perugia, Italy. He is the founder and coleader of the Computational Laboratory for Hybrid/Organic Photovoltaics. He is an expert in the development and application of quantum chemical methods to the study of the structural, electronic, and optical properties of complex systems including transition metals. His main research interest is in the field of hybrid/organic photovoltaics, employing DFT, ab initio molecular dynamics, and TDDFT methods to investigate the electronic structure of materials and interfaces. He is the 2007 recipient of the Raffaello Nasini Gold Medal of the Inorganic Chemistry Division of the Italian Chemical Society.

Juan Bisquert is a professor of Applied Physics at Universitat Jaume I de Castelló. His main topics of interest are dye and quantum dot-sensitized solar cells, organic solar cells, and solar fuel production. He has developed the application of measurement techniques and physical modeling that relate the device operation with the elementary steps that take place at the nanoscale dimension: charge transfer, carrier transport, chemical reaction, etc., especially in the field of impedance spectroscopy, as well as general device models. He is currently a senior editor of the *Journal of Physical Chemistry* and a member of the Editorial Boards of *Energy and Environmental Science* and *ChemElectroChem*.

Peng Wang obtained his Ph.D. in 2001 from Changchun Institute of Applied Chemsitry, Chinese Academy of Sciences. He then worked as a postdoctoral fellow at Swiss Federal Institute of Technology, University of Cambridge, and University of California, Santa Barbara. He is now a professor of chemistry at Changchun Institute of Applied Chemistry, Chinese Academy of Sciences. His research interest centers on material innovation, device engineering, and in-depth understanding of the charge and energy transfer processes for efficient photovoltaic devices. He has received several awards, including the 2009 CAS-Bayer Young Scientist Award, the 2012 CSS-RSC Young Chemist Award, and the 2013 Young Scientist Award of CAS.

REFERENCES

(1) Carp, O.; Huisman, C. L.; Reller, A. *Prog. Solid State Chem.* **2004**, 32, 33.

(2) Dambournet, D.; Belharouak, I.; Amine, K. *Chem. Mater.* **2010**, *22*, 1173.

(3) Simons, P. Y.; Dachille, F. *Acta Crystallogr.* **1967**, *23*, 334.

(4) Latroche, M.; Brohan, L.; Marchand, R.; Tournoux, M. *J. Solid State Chem.* **1989**, *81*, 78.

(5) Diebold, U. *Surf. Sci. Rep.* **2003**, *48*, 53.

(6) Kavan, L.; Grätzel, M.; Gilbert, S. E.; Klemenz, C.; Scheel, H. J. *J. Am. Chem. Soc.* **1996**, *118*, 6716.

(7) Gerischer, H.; Michel-Beyerle, M. E.; Rebentrost, F.; Tributsch, H. *Electrochim. Acta* **1968**, *13*, 1509.

(8) O'Regan, B.; Grätzel, M. *Nature* **1991**, *353*, 737.

(9) Yella, A.; Lee, H.-W.; Tsao, H. N.; Yi, C.; Chandiran, A. K.; Nazeeruddin, M. K.; Diau, E. W.-G.; Yeh, C.-Y.; Zakeeruddin, S. M.; Grätzel, M. *Science* **2011**, *334*, 629.

(10) Grätzel, M. *Acc. Chem. Res.* **2009**, *42*, 1788.

(11) Hagfeldt, A.; Boschloo, G.; Sun, L.; Kloo, L.; Pettersson, H. *Chem. Rev.* **2010**, *110*, 6595.

(12) Jung, H. S.; Lee, J.-K. *J. Phys. Chem. Lett.* **2013**, *4*, 1682.

(13) Bahers, T. L.; Pauporte, T.; Laine, P. P.; Labat, F.; Adamo, C.; Ciofini, I. *J. Phys. Chem. Lett.* **2013**, *4*, 1044.

(14) Moser, J. E. *Dye-Sensitized Solar Cells*; EPFL Press: Lausanne, 2010; p 403.

(15) Wiberg, J.; Marinado, T.; Hagberg, D. P.; Sun, L.; Hagfeldt, A.; Albinsson, B. *J. Phys. Chem. C* **2009**, *113*, 3881.

(16) Pastore, M.; De Angelis, F. *Phys. Chem. Chem. Phys.* **2012**, *14*, 920.

(17) Grätzel, M. *J. Photochem. Photobiol. A* **2004**, *164*, 3.

(18) Odobel, F.; Blart, E.; Lagrée, M.; Villieras, M.; Boujtita, H.; Murr, N. E.; Caramori, S.; Bignozzi, C. A. *J. Mater. Chem.* **2003**, *13*, 502.

(19) Abbotto, A.; Manfredi, N.; Marinzi, C.; De Angelis, F.; Mosconi, E.; Yum, J.; Xianxi, Z.; Nazeeruddin, M. K.; Grätzel, M. *Energy Environ. Sci.* **2009**, *2*, 1094.

(20) Nara, M.; Torii, H.; Tasumi, M. *J. Phys. Chem.* **1996**, *100*, 19812.

(21) Deacon, G. B.; Phillips, R. J. *Coord. Chem. Rev.* **1980**, *33*, 227.

(22) Anselmi, C.; Mosconi, E.; Pastore, M.; Ronca, E.; De Angelis, F. *Phys. Chem. Chem. Phys.* **2012**, *14*, 15963.

(23) Shklover, V.; Nazeeruddin, M.-K.; Zakeeruddin, S. M.; Barbé, C.; Kay, A.; Haibach, T.; Steurer, W.; Hermann, R.; Nissen, H.-U.; Grätzel, M. *Chem. Mater.* **1997**, *9*, 430.

(24) De Angelis, F.; Fantacci, S.; Selloni, A.; Nazeeruddin, M. K.; Grätzel, M. *J. Am. Chem. Soc.* **2007**, *129*, 14156.

(25) Persson, P.; Lundqvist, M. J. *J. Phys. Chem. B* **2005**, *109*, 11918.

(26) De Angelis, F.; Fantacci, S.; Selloni, A.; Nazeeruddin, M. K.; Grätzel, M. *J. Phys. Chem. C* **2010**, *14*, 6054.

(27) Schiffmann, F.; VandeVondele, J.; Hutter, J.; Wirz, R.; Urakawa, A.; Baiker, A. *J. Phys. Chem. C* **2010**, *114*, 8398.

(28) Labat, F.; Ciofini, I.; Adamo, C. *J. Mater. Chem.* **2012**, *22*, 12205.

(29) Martsinovich, N.; Ambrosio, F.; Troisi, A. *Phys. Chem. Chem. Phys.* **2012**, *14*, 16668.

(30) Johansson, E. M. J.; Edvinsson, T.; Odelius, M.; Hagberg, D. P.; Sun, L.; Hagfeldt, A.; Siegbahn, H.; Rensmo, H. *J. Phys. Chem. C* **2007**, *111*, 8580.

(31) Marinado, T.; Hagberg, D. P.; Hedlund, M.; Edvinsson, T.; Johansson, E. M. J.; Boschloo, G.; Rensmo, H.; Brinck, T.; Sun, L.; Hagfeldt, A. *Phys. Chem. Chem. Phys.* **2009**, *11*, 133.

(32) Hahlin, M.; Johansson, E. M. J.; Plogmaker, S.; Odelius, M.; Hagberg, D. P.; Sun, L.; Siegbahn, H.; Rensmo, H. *Phys. Chem. Chem. Phys.* **2010**, *12*, 1507.

(33) Karlsson, K. M.; Jiang, X.; Eriksson, S. K.; Gabrielsson, E.; Rensmo, H.; Hagfeldt, A.; Sun, L. *Chem.—Eur. J.* **2011**, *17*, 6415.

(34) Wang, M.; Plogmaker, S.; Humphry-Baker, R.; Pechy, P.; Rensmo, H.; Zakeeruddin, S. M.; Grätzel, M. *ChemSusChem* **2012**, *5*, 181.

(35) Griffith, M. J.; James, M.; Triani, G.; Wagner, P.; Wallace, G. G.; Officer, D. L. *Langmuir* **2011**, *27*, 12944.

(36) Lee, K. E.; Gomez, M. A.; Regier, T.; Hu, Y.; Demopoulos, G. P. *J. Phys. Chem. C* **2011**, *115*, 5692.

(37) Cao, Y.; Cai, N.; Wang, Y.; Li, R.; Yuan, Y.; Wang, P. *Phys. Chem. Chem. Phys.* **2012**, *14*, 8282.

(38) Cai, N.; Li, R.; Wang, Y.; Zhang, M.; Wang, P. *Energy Environ. Sci.* **2013**, *6*, 139.

(39) Zhang, J.; Yao, Z.; Cai, Y.; Yang, L.; Xu, M.; Li, R.; Zhang, M.; Dong, X.; Wang, P. *Energy Environ. Sci.* **2013**, *6*, 1604.

(40) Ellis-Gibbings, L.; Johansson, V.; Walsh, R. B.; Kloo, L.; Quinton, J. S.; Andersson, G. G. *Langmuir* **2012**, *28*, 9431.

(41) Nilsing, M.; Persson, P.; Ojamäe, L. *Chem. Phys. Lett.* **2005**, *415*, 375.

(42) Pal, S. K.; Sundstrom, V.; Galoppini, E.; Persson, P. *Dalton Trans.* **2009**, 10021.

(43) Persson, P.; Lundqvist, M. J.; Ernstorfer, R.; Goddard, W. A.; Willig, F. *J. Chem. Theory Comput.* **2006**, *2*, 441.

(44) Lundqvist, M. J.; Nilsing, M.; Lunell, S.; Åkermark, B.; Persson, P. *J. Phys. Chem. B* **2006**, *110*, 20513.

(45) Li, J.; Wang, H.; Persson, P.; Thoss, M. *J. Chem. Phys.* **2012**, *137*, 22A529.

(46) Ambrosio, F.; Martsinovich, N.; Troisi, A. *J. Phys. Chem. C* **2012**, *116*, 2622.

(47) Maggio, E.; Martsinovich, N.; Troisi, A. *J. Phys. Chem. C* **2012**, *116*, 7638.

(48) Martsinovich, N.; Troisi, A. *J. Phys. Chem. C* **2011**, *115*, 11781.

(49) Jones, D. R.; Troisi, A. *Phys. Chem. Chem. Phys.* **2010**, *12*, 4625.

(50) Maggio, E.; Martsinovich, N.; Troisi, A. *J. Chem. Phys.* **2012**, *137*, 22A508.

(51) Maggio, E.; Martsinovich, N.; Troisi, A. *Angew. Chem., Int. Ed.* **2013**, *52*, 973.

(52) Ambrosio, F.; Martsinovich, N.; Troisi, A. *J. Phys. Chem. Lett.* **2012**, *3*, 1531.

(53) Szarko, J. M.; Neubauer, A.; Bartelt, A.; Socaciu-Siebert, L.; Birkner, F.; Schwarzburg, K.; Hannappel, T.; Eichberger, R. *J. Phys. Chem. C* **2008**, *112*, 10542.

(54) Moser, J. E.; Grätzel, M. *Chem. Phys.* **1993**, *176*, 493.

(55) Bisquert, J.; Zaban, A.; Salvador, P. *J. Phys. Chem. B* **2002**, *106*, 8774.

(56) O'Regan, B.; Moser, J.; Anderson, M.; Grätzel, M. *J. Phys. Chem.* **1990**, *94*, 8720.

(57) Haque, S. A.; Tachibana, Y.; Willis, R. L.; Moser, J. E.; Grätzel, M.; Klug, D. R.; Durrant, J. R. *J. Phys. Chem. B* **2000**, *104*, 538.

(58) Haque, S. A.; Tachibana, Y.; Klug, D. R.; Durrant, J. R. *J. Phys. Chem. B* **1998**, *102*, 1745.

(59) Haque, S. A.; Handa, S.; Peter, K.; Palomares, E.; Thelakkat, M.; Durrant, J. R. *Angew. Chem., Int. Ed.* **2005**, *44*, 5740.

(60) Prezhdo, O. V.; Duncan, W. R.; Prezhdo, V. V. *Acc. Chem. Res.* **2008**, *41*, 339.

(61) Haque, S. A.; Palomares, E.; Cho, B. M.; Green, A. N. M.; Hirata, N.; Klug, D. R.; Durrant, J. R. *J. Am. Chem. Soc.* **2005**, *127*, 3456.

(62) De Angelis, F.; Vitillaro, G.; Kavan, L.; Nazeeruddin, M. K.; Grätzel, M. *J. Phys. Chem. C* **2012**, *116*, 18124.

(63) Cai, N.; Zhang, J.; Xu, M.; Zhang, M.; Wang, P. *Adv. Funct. Mater.* **2013**, *23*, 3539.

(64) Zhang, M.; Wang, Y.; Xu, M.; Ma, W.; Li, R.; Wang, P. *Energy Environ. Sci.* **2013**, *6*, 2944.

(65) Barea, E. M.; Bisquert, J. *Langmuir* **2013**, *29*, 8773.

(66) Zhang, M.; Zhang, J.; Fan, Y.; Yang, L.; Wang, Y.; Li, R.; Wang, P. *Energy Environ. Sci.* **2013**, *6*, 2939.

(67) Sayama, K.; Tsukagoshi, S.; Mori, T.; Hara, K.; Ohga, Y.; Shinpou, A.; Abe, Y.; Suga, S.; Arakawa, H. *Sol. Energy Mater. Sol. Cells* **2003**, *80*, 47.

(68) Tian, H.; Yang, X.; Chen, R.; Zhang, R.; Hagfeldt, A.; Sun, L. *J. Phys. Chem. C* **2008**, *112*, 11023.

(69) Imahori, H.; Hayashi, S.; Oguro, A.; Eu, S.; Umeyama, T.; Matano, Y. *J. Phys. Chem. C* **2009**, *113*, 18406.

(70) Rothenberger, G.; Fitzmaurice, D.; Grätzel, M. *J. Phys. Chem.* **1992**, *96*, 5983.

(71) O'Regan, B.; Grätzel, M.; Fitzmaurice, D. *J. Phys. Chem.* **1991**, *95*, 10525.

(72) Boschloo, G.; Fitzmaurice, D. *J. Phys. Chem. B* **1999**, *103*, 7860.

(73) Redmond, G.; Fitzmaurice, D. *J. Phys. Chem.* **1993**, *97*, 1426.

(74) Enright, B.; Redmond, G.; Fitzmaurice, D. *J. Phys. Chem.* **1994**, *98*, 6195.

(75) Westermark, K.; Henningsson, A.; Rensmo, H.; Södergren, S.; Siegbahn, H.; Hagfeldt, A. *Chem. Phys.* **2002**, *285*, 157.

(76) Yan, S. G.; Hupp, J. T. *J. Phys. Chem.* **1996**, *100*, 6867.

(77) De Angelis, F.; Fantacci, S.; Selloni, A.; Grätzel, M.; Nazeeruddin, M. K. *Nano Lett.* **2007**, *7*, 3189.

(78) Tachibana, Y.; Haque, S. A.; Mercer, I. P.; Moser, J. E.; Klug, D. R.; Durrant, J. R. *J. Phys. Chem. B* **2001**, *105*, 7424.

(79) Rühle, S.; Greenshtein, M.; Chen, S.-G.; Merson, A.; Pizem, H.; Sukenik, C. S.; Cahen, D.; Zaban, A. *J. Phys. Chem. B* **2005**, *109*, 18907.

(80) Kusama, H.; Orita, H.; Sugihara, H. *Langmuir* **2008**, *24*, 4411.

(81) Chen, P.; Yum, J. H.; De Angelis, F.; Mosconi, E.; Fantacci, S.; Moon, S.-J.; Baker, R. H.; Ko, J.; Nazeeruddin, M. K.; Grätzel, M. *Nano Lett.* **2009**, *9*, 2487.

(82) Miyashita, M.; Sunahara, K.; Nishikawa, K.; Uemura, Y.; Koumura, N.; Hara, K.; Mori, A.; Abe, T.; Suzuki, E.; Mori, S. *J. Am. Chem. Soc.* **2008**, *130*, 17874.

(83) Ronca, E.; Pastore, M.; Belpassi, L.; Tarantelli, F.; De Angelis, F. *Energy Environ. Sci.* **2013**, *6*, 183.

(84) De Angelis, F.; Fantacci, S.; Mosconi, E.; Nazeeruddin, M. K.; Grätzel, M. *J. Phys. Chem. C* **2011**, *115*, 8825.

(85) Khazraji, A. C.; Hotchandani, S.; Das, S.; Kamat, P. V. *J. Phys. Chem. B* **1999**, *103*, 4693.

(86) Sayama, K.; Tsukagoshi, S.; Hara, K.; Ohga, Y.; Shinpou, A.; Abe, Y.; Suga, S.; Arakawa, H. *J. Phys. Chem. B* **2002**, *106*, 1363.

(87) Lu, H.-P.; Tsai, C.-Y.; Yen, W.-N.; Hsieh, C.-P.; Lee, C.-W.; Yeh, C.-Y.; Diau, E. W.-G. *J. Phys. Chem. C* **2009**, *113*, 20990.

(88) El-Zohry, A.; Orthaber, A.; Zietz, B. *J. Phys. Chem. C* **2012**, *116*, 26144.

(89) Wang, P.; Zakeeruddin, S. M.; Humphry-Baker, R.; Moser, J. E.; Grätzel, M. *Adv. Mater.* **2003**, *15*, 2101.

(90) Wang, P.; Zakeeruddin, S. M.; Comte, P.; Charvet, R.; Humphry-Baker, R.; Grätzel, M. *J. Phys. Chem. B* **2003**, *107*, 14336.

(91) Zhang, Z.; Zakeeruddin, S. M.; O'Regan, B. C.; Humphry-Baker, R.; Grätzel, M. *J. Phys. Chem. B* **2005**, *109*, 21818.

(92) Wang, Z.-S.; Cui, Y.; Dan-oh, Y.; Kasada, C.; Shinpo, A.; Hara, K. *J. Phys. Chem. C* **2007**, *111*, 7224.

(93) Hara, K.; Dan-oh, Y.; Kasada, C.; Ohga, Y.; Shinpo, A.; Suga, S.; Sayama, K.; Arakawa, H. *Langmuir* **2004**, *20*, 4205.

(94) Morandeira, A.; López-Duarte, I.; O'Regan, B.; Martínez-Díaz, M. V.; Forneli, A.; Palomares, E.; Torres, T.; Durrant, J. R. *J. Mater. Chem.* **2009**, *19*, 5016.

(95) de Miguel, G.; Marchena, M.; Ziółek, M.; Pandey, S. S.; Hayase, S.; Douhal, A. *J. Phys. Chem. C* **2012**, *116*, 12137.

(96) Yum, J. H.; Moon, S. J.; Humphry-Baker, R.; Walter, P.; Geiger, T.; Nüesch, F.; Grätzel, M.; Nazeeruddin, M. K. *Nanotechnology* **2008**, *19*, 424005.

(97) Zhang, Z.; Evans, N.; Zakeeruddin, S. M.; Humphry-Baker, R.; Grätzel, M. *J. Phys. Chem. C* **2007**, *111*, 398.

(98) Neale, N. R.; Kopidakis, N.; van de Lagemaat, J.; Grätzel, M.; Frank, A. J. *J. Phys. Chem. B* **2005**, *109*, 23183.

(99) Kwon, Y. S.; Song, I. Y.; Lim, J.; Park, S.-H.; Siva, A.; Park, Y.-C.; Jang, H. M.; Park, T. *RSC Adv.* **2012**, *2*, 3467.

(100) Kelly, C. A.; Farzad, F.; Thompson, D. W.; Stipkala, J. M.; Meyer, G. J. *Langmuir* **1999**, *15*, 7047.

(101) Furube, A.; Katoh, R.; Hara, K.; Sato, T.; Murata, S.; Arakawa, H.; Tachiya, M. *J. Phys. Chem. B* **2005**, *109*, 16406.

(102) Koops, S. E.; O'Regan, B. C.; Barnes, P. R. F.; Durrant, J. R. *J. Am. Chem. Soc.* **2009**, *131*, 4808.

(103) Li, R.; Liu, D.; Zhou, D.; Shi, Y.; Wang, Y.; Wang, P. *Energy Environ. Sci.* **2010**, *3*, 1765.

(104) Yu, Q.; Wang, Y.; Yi, Z.; Zu, N.; Zhang, J.; Zhang, M.; Wang, P. *ACS Nano* **2010**, *4*, 6032.

(105) Bai, Y.; Zhang, J.; Wang, Y.; Zhang, M.; Wang, P. *Langmuir* **2011**, *27*, 4749.

(106) Shi, Y.; Wang, Y.; Zhang, M.; Dong, X. *Phys. Chem. Chem. Phys.* **2011**, *13*, 14590.

(107) Jennings, J. R.; Wang, Q. *J. Phys. Chem. C* **2010**, *114*, 1715.

(108) Kopidakis, N.; Benkstein, K. D.; van de Lagemaat, J.; Frank, A. J. *J. Phys. Chem. B* **2003**, *107*, 11307.

(109) Nakade, S.; Kanzaki, T.; Kubo, W.; Kitamura, T.; Wada, Y.; Yanagida, S. *J. Phys. Chem. B* **2005**, *109*, 53480.

(110) Wang, H.; Peter, L. M. *J. Phys. Chem. C* **2012**, *116*, 10468.

(111) Nazeeruddin, M. K.; Kay, A.; Rodicio, I.; Humphry-Baker, R.; Müller, E.; Liska, P.; Vlachopoulos, N.; Grätzel, M. *J. Am. Chem. Soc.* **1993**, *115*, 6382.

(112) Dürr, M.; Yasuda, A.; Nelles, G. *Appl. Phys. Lett.* **2006**, *89*, 061110.

(113) Boschloo, G.; Häggman, L.; Hagfeldt, A. *J. Phys. Chem. B* **2006**, *110*, 13144.

(114) Li, R.; Liu, J.; Cai, N.; Zhang, M.; Wang, P. *J. Phys. Chem. B* **2010**, *114*, 4461.

(115) Long, H.; Zhou, D.; Zhang, M.; Peng, C.; Uchida, S.; Wang, P. *J. Phys. Chem. C* **2011**, *115*, 14408.

(116) Shi, C.; Dai, S.; Wang, K.; Pan, X.; Kong, F.; Hu, L. *Vib. Spectrosc.* **2005**, *39*, 99.

(117) Göthelid, M.; Yu, S.; Ahmadi, S.; Sun, C.; Zuleta, M. *Int. J. Photoenergy* **2011**, *2011*, 401356.

(118) Fukui, A.; Komiya, R.; Yamanaka, R.; Islam, A.; Han, L. *Sol. Energy Mater. Sol. Cells* **2006**, *90*, 649.

(119) Wu, J.; Lan, Z.; Lin, J.; Huang, M.; Li, P. *J. Power Sources* **2007**, *173*, 585.

(120) Lee, K.-M.; Suryanarayanan, V.; Ho, K.-C. *J. Power Sources* **2009**, *188*, 635.

(121) Stergiopoulos, T.; Kontos, A. G.; Likodimos, V.; Perganti, D.; Falaras, P. *J. Phys. Chem. C* **2011**, *115*, 10236.

(122) Hao, F.; Jiao, X.; Liab, J.; Lin, H. *Nanoscale* **2013**, *5*, 726.

(123) Cai, N.; Zhang, J.; Zhou, D.; Yi, Z.; Guo, J.; Wang, P. *J. Phys. Chem. C* **2009**, *113*, 4215.

(124) Zhang, M.; Zhang, J.; Bai, Y.; Wang, Y.; Su, M.; Wang, P. *Phys. Chem. Chem. Phys.* **2011**, *13*, 3788.

(125) Zhou, D.; Bai, Y.; Zhang, J.; Cai, N.; Su, M.; Wang, Y.; Zhang, M.; Wang, P. *J. Phys. Chem. C* **2011**, *115*, 816.

(126) Mahanta, S.; Furube, A.; Matsuzaki, H.; Murakami, T. N.; Matsumoto, H. *J. Phys. Chem. C* **2012**, *116*, 20213.

(127) Burschka, J.; Dualeh, A.; Kessler, F.; Baranoff, E.; Cevey-Ha, N.; Yi, C.; Nazeeruddin, M. K.; Grätzel, M. *J. Am. Chem. Soc.* **2011**, *133*, 18042.

(128) Burschka, J.; Kessler, F.; Nazeeruddin, M. K.; Grätzel, M. *Chem. Mater.* **2013**, *25*, 2986.

(129) Abate, A.; Hollman, D. J.; Teuscher, J.; Pathak, S.; Avolio, R.; D'Errico, G.; Vitiello, G.; Fantacci, S.; Snaith, H. J. *J. Am. Chem. Soc.* **2013**, *135*, 13538.

(130) Li, L.-L.; Chang, Y.-C.; Wu, H.-P.; Diau, E. W.-G. *Int. Rev. Phys. Chem.* **2012**, *31*, 420.

(131) Bisquert, J. *Phys. Chem. Chem. Phys.* **2008**, *10*, 49.

(132) Bisquert, J. *Phys. Chem. Chem. Phys.* **2008**, *10*, 3175.

(133) Abayev, I.; Zaban, A.; Fabregat-Santiago, F.; Bisquert. *Phys. Status Solidi A* **2003**, *196*, R4.

(134) Wang, Q.; Ito, S.; Grätzel, M.; Fabregat-Santiago, F.; Mora-Seró, I.; Bisquert, J.; Bessho, T.; Imai, H. *J. Phys. Chem. B* **2006**, *110*, 19406.

(135) Jennings, J. R.; Liu, Y.; Safari-Alamuti, F.; Wang, Q. *J. Phys. Chem. C* **2012**, *116*, 1556.

(136) Raga, S. R.; Fabregat-Santiago, F. *Phys. Chem. Chem. Phys.* **2013**, *15*, 2328.

(137) Schwarzburg, K.; Willig, F. *Appl. Phys. Lett.* **1991**, *58*, 2520.

(138) Bisquert, J.; Vikhrenko, V. S. *J. Phys. Chem. B* **2004**, *108*, 2313.

(139) Bisquert, J. *Phys. Chem. Chem. Phys.* **2008**, *10*, 49.

(140) Anta, J. A.; Mora-Seró, I.; Dittrich, T.; Bisquert, J. *Phys. Chem. Chem. Phys.* **2008**, *10*, 4478.

(141) Bisquert, J.; Marcus, R. A. *Top. Curr. Chem.* **2013**, DOI: 10.1007/128_2013_471.

(142) Bisquert, J. *J. Phys. Chem. B* **2002**, *106*, 325.

AF

dx.doi.org/10.1021/cr400606n | *Chem. Rev.* XXXX, XXX, XXX–XXX

(143) Fabregat-Santiago, F.; Bisquert, J.; Garcia-Belmonte, G.; Boschloo, G.; Hagfeldt, A. *Sol. Energy Mater. Sol. Cells* **2005**, *87*, 117.

(144) Fabregat-Santiago, F.; Garcia-Belmonte, G.; Mora-Seró, I.; Bisquert, J. *Phys. Chem. Chem. Phys.* **2011**, *13*, 9083.

(145) Dloczik, L.; Ileperuma, O.; Lauerman, I.; Peter, L. M.; Ponomarev, E. A.; Redmond, G.; Shaw, N. J.; Uhlendorf, I. *J. Phys. Chem. B* **1997**, *101*, 10281.

(146) Peter, L. M.; Ponomarev, E. A.; Franco, G.; Shaw, N. J. *Electrochim. Acta* **1999**, *45*, 549.

(147) Jennings, J. R.; Peter, L. M. *J. Phys. Chem. C* **2007**, *111*, 16100.

(148) Wang, H.; Peter, L. M. *J. Phys. Chem. C* **2009**, *113*, 18125.

(149) Villanueva-Cab, J.; Wang, H.; Oskam, G.; Peter, L. M. *J. Phys. Chem. Lett.* **2010**, *1*, 748.

(150) Zaban, A.; Greenshtein, M.; Bisquert, J. *ChemPhysChem* **2003**, *4*, 859.

(151) Bisquert, J.; Zaban, A.; Greenshtein, M.; Mora-Seró, I. *J. Am. Chem. Soc.* **2004**, *126*, 13550.

(152) Anta, J. A.; Idigoras, J.; Guillen, E.; Villanueva-Cab, J.; Mandujano-Ramirez, H. J.; Oskam, G.; Pelleja, L.; Palomares, E. *Phys. Chem. Chem. Phys.* **2012**, *14*, 10285.

(153) Gonzalez-Vazquez, J. P.; Anta, J. A.; Bisquert, J. *J. Phys. Chem. C* **2010**, *114*, 8552.

(154) González-Vázquez, J. P.; Anta, J. A.; Bisquert, J. *Phys. Chem. Chem. Phys.* **2009**, *11*, 10359.

(155) Anta, J. A. *Energy Environ. Sci.* **2009**, *2*, 387.

(156) Ansari-Rad, M.; Anta, J. A.; Bisquert, J. *J. Phys. Chem. C* **2013**, *117*, 16275.

(157) Ansari-Rad, M.; Abdi, Y.; Arzi, E. *J. Appl. Phys.* **2012**, *112*, 074319.

(158) Ansari-Rad, M.; Abdi, Y.; Arzi, E. *J. Phys. Chem. C* **2012**, *116*, 10867.

(159) Bisquert, J. *Phys. Chem. Chem. Phys.* **2003**, *5*, 5360.

(160) Bisquert, J.; Fabregat-Santiago, F.; Mora-Seró, I.; Garcia-Belmonte, G.; Barea, E. M.; Palomares, E. *Inorg. Chim. Acta* **2008**, *361*, 684.

(161) Berger, T.; Monllor-Satoca, D.; Jankulovska, M.; Lana-Villarreal, T.; Gomez, R. *ChemPhysChem* **2012**, *13*, 2824.

(162) Raga, S. R.; Barea, E. M.; Fabregat-Santiago, F. *J. Phys. Chem. Lett.* **2012**, *3*, 1629.

(163) Shaw, J. G.; Hack, M. *J. Appl. Phys.* **1988**, *64*, 4562.

(164) Schiff, E. A. *J. Phys.: Condens. Matter* **2004**, *16*, S5265.

(165) Sildos, I.; Suisalu, A.; Aarik, J.; Sekiya, T.; Kurita, S. *J. Lumin.* **2000**, *87−89*, 290.

(166) Watanabe, M.; Hayashi, T. *J. Lumin.* **2005**, *112*, 88.

(167) Tang, H.; Levy, F.; Berger, H.; Schmid, P. E. *J. Phys. Rev. B* **1995**, *52*, 7771.

(168) Di Valentin, C.; Selloni, A. *J. Phys. Chem. Lett.* **2011**, *2*, 2223.

(169) Nunzi, F.; Mosconi, E.; Storchi, L.; Ronca, E.; Selloni, A.; Gratzel, M.; De Angelis, F. *Energy Environ. Sci.* **2013**, *6*, 1221.

(170) Bisquert, J. *Phys. Rev. B* **2008**, *77*, 235203.

(171) Bisquert, J.; Fabregat-Santiago, F.; Mora-Seró, I.; Garcia-Belmonte, G.; Giménez, S. *J. Phys. Chem. C* **2009**, *113*, 17278.

(172) Bisquert, J.; Mora-Seró, I. *J. Phys. Chem. Lett.* **2010**, *1*, 450.

(173) Salvador, P.; González-Hidalgo, M.; Zaban, A.; Bisquert, J. *J. Phys. Chem. B* **2005**, *109*, 15915.

(174) Södergren, S.; Hagfeldt, A.; Olsson, J.; Lindquist, S. E. *J. Phys. Chem.* **1994**, *98*, 5552.

(175) Bertoluzzi, L.; Ma, S. *Phys. Chem. Chem. Phys.* **2013**, *15*, 4283.

(176) Bisquert, J.; Mora-Sero, I.; Fabregat-Santiago, F. *ChemElectroChem* **2014**, *1*, 289.

(177) Chen, J.; Li, B.; Zheng, J.; Jia, S.; Zhao, J.; Jing, H.; Zhu, Z. *J. Phys. Chem. C* **2011**, *115*, 7104.

(178) Jennings, J. R.; Li, F.; Wang, Q. *J. Phys. Chem. C* **2010**, *114*, 14665.

(179) Fabregat-Santiago, F.; Bisquert, J.; Cevey, L.; Chen, P.; Wang, M.; Zakeeruddin, S. M.; Grätzel, M. *J. Am. Chem. Soc.* **2009**, *131*, 558.

(180) Park, N.-G.; van de Lagemaat, J.; Frank, A. J. *J. Phys. Chem. B* **2000**, *104*, 8989.

(181) Ito, S.; Murakami, T. N.; Comte, P.; Liska, P.; Grätzel, C.; Nazeeruddin, M. K.; Grätzel, M. *Thin Solid Films* **2008**, *516*, 4613.

(182) Wang, Z. S.; Kawauchi, H.; Kashima, T.; Arakawa, H. *Coordin. Chem. Rev.* **2004**, *248*, 1381.

(183) Chang, Y.-J.; Kong, E.-H.; Park, Y.-C.; Jang, H. M. *J. Mater. Chem. A* **2013**, *1*, 9707.

(184) Wu, H.-P.; Lan, C.-M.; Hu, J.-Y.; Huang, W.-K.; Shiu, J.-W.; Lan, Z.-J.; Tsai, C.-M.; Su, C.-H.; Diau, E. W.-G. *J. Phys. Chem. Lett.* **2013**, *4*, 1570.

(185) Lee, J.-K.; Jeong, B.-H.; Jang, S.-I.; Yeo, Y.-S.; Park, S.-H.; Kim, J.-U.; Kim, Y.-G.; Jang, Y.-W.; Kim, M.-R. *J. Mater. Sci.: Mater. Electron.* **2009**, *20*, S446.

(186) Tian, Z.; Tian, H.; Wang, X.; Yuan, S.; Zhang, J.; Zhang, X.; Yu, T.; Zou, Z. *Appl. Phys. Lett.* **2009**, *94*, 031905.

(187) Macák, J. M.; Tsuchiya, H.; Ghicov, A.; Schmuki, P. *Electrochem. Commun.* **2005**, *7*, 1133.

(188) Park, J. H.; Lee, T.-W.; Kang, M. G. *Chem. Commun.* **2008**, 2867.

(189) Kuang, D.; Brillet, J.; Chen, P.; Takata, M.; Uchida, S.; Miura, H.; Sumioka, K.; Zakeeruddin, S. M.; Grätzel, M. *ACS nano* **2008**, *2*, 1113.

(190) Zhu, K.; Neale, N. R.; Miedaner, A.; Frank, A. J. *Nano Lett.* **2007**, *7*, 69.

(191) Zhu, K.; Vinzant, T. B.; Neale, N. R.; Frank, A. J. *Nano Lett.* **2007**, *7*, 3739.

(192) Varghese, O. K.; Paulose, M.; Grimes, C. A. *Nat. Nanotechnol.* **2009**, *4*, 592.

(193) Li, L.-L.; Tsai, C.-Y.; Wu, H.-P.; Chen, C.-C.; Diau, E. W.-G. *J. Mater. Chem.* **2010**, *20*, 2753.

(194) Li, L.-L.; Chen, Y.-J.; Wu, H.-P.; Wang, N. S.; Diau, E. W.-G. *Energy Environ. Sci.* **2011**, *4*, 3420.

(195) Jen, H.-P.; Lin, M.-H.; Li, L.-L.; Wu, H.-P.; Huang, W.-K.; Cheng, P.-J.; Diau, E. W.-G. *ACS Appl. Mater. Interfaces* **2013**, *5*, 10098.

(196) Jiu, J.; Isoda, S.; Wang, F.; Adachi, M. *J. Phys. Chem. B* **2006**, *110*, 2087.

(197) Kang, S. H.; Choi, S.-H.; Kang, M.-S.; Kim, J.-Y.; Kim, H.-S.; Hyeon, T.; Sung, Y.-E. *Adv. Mater.* **2008**, *20*, 54.

(198) Liu, B.; Aydil, E. S. *J. Am. Chem. Soc.* **2009**, *131*, 3985.

(199) Wang, H.; Liu, M.; Zhang, M.; Wang, P.; Miura, H.; Cheng, Y.; Bella, J. *Phys. Chem. Chem. Phys.* **2011**, *13*, 17359.

(200) Wang, M.; Bai, J.; Le Formal, F.; Moon, S.-J.; Cevey-Ha, L.; Humphry-Baker, R.; Grätzel, C.; Zakeeruddin, S. M.; Grätzel, M. *J. Phys. Chem. C* **2012**, *116*, 3266.

(201) Adachi, M.; Murata, Y.; Takao, J.; Jiu, J.; Sakamoto, M.; Wang, F. *J. Am. Chem. Soc.* **2004**, *126*, 14943.

(202) Enache-Pommer, E.; Boercker, J. E.; Aydil, E. S. *Appl. Phys. Lett.* **2007**, *91*, 123116.

(203) Feng, X.; Shankar, K.; Varghese, O. K.; Paulose, M.; Latempa, T. J.; Grimes, C. A. *Nano Lett.* **2008**, *8*, 3781.

(204) Feng, X.; Zhu, K.; Frank, A. J.; Grimes, C. A.; Mallouk, T. E. *Angew. Chem., Int. Ed.* **2012**, *51*, 2727.

(205) Liao, J.-Y.; Lei, B.-X.; Chen, H.-Y.; Kuang, D.-B.; Su, C.-Y. *Energy Environ. Sci.* **2012**, *5*, 5750.

(206) Ruan, C.; Paulose, M.; Varghese, O. K.; Mor, G. K.; Grimes, C. A. *J. Phys. Chem. B* **2005**, *109*, 15754.

(207) Albu, S. P.; Ghicov, A.; Aldabergenova, S.; Drechsel, P.; LeClere, D.; Thompson, G. E.; Macak, J. M.; Schmuki, P. *Adv. Mater.* **2008**, *20*, 4135.

(208) Roy, P.; Albu, S. P.; Schmuki, P. *Electrochem. Commun.* **2010**, *12*, 949.

(209) Ito, S.; Ha, N.-L. C.; Rothenberger, G.; Liska, P.; Comte, P.; Zakeeruddin, S. M.; Péchy, P.; Nazeeruddin, M. K.; Grätzel, M. *Chem. Commun.* **2006**, 4004.

(210) van de Lagemaat, J.; Frank, A. J. *J. Phys. Chem. B* **2001**, *105*, 11194.

(211) Lamberti, A.; Sacco, A.; Bianco, S.; Manfredi, D.; Cappelluti, F.; Hernandez, S.; Quaglio, M.; Pirri, C. F. *Phys. Chem. Chem. Phys.* **2013**, *15*, 2596.

(212) Lei, B.-X.; Liao, J.-Y.; Zhang, R.; Wang, J.; Su, C.-Y.; Kuang, D.-B. *J. Phys. Chem. C* **2010**, *114*, 15228.

(213) Mor, G. K.; Shankar, K.; Paulose, M.; Varghese, O. K.; Grimes, C. A. *Nano Lett.* **2006**, *6*, 215.

(214) Paulose, M.; Shankar, K.; Varghese, O. K.; Mor, G. K.; Grimes, C. A. *J. Phys. D: Appl. Phys.* **2006**, *39*, 2498.

(215) Shiu, J. W.; Lan, C. M.; Chang, Y. C.; Wu, H. P.; Huang, W. K.; Diau, E. W. G. *ACS Nano* **2012**, *6*, 10862.

(216) Crossland, E. J. W.; Noel, N.; Sivaram, V.; Leijtens, T.; Alexander-Webber, J. A.; Snaith, H. J. *Nature* **2013**, *495*, 215.

(217) Krüger, J.; Plass, R.; Grätzel, M.; Cameron, P. J.; Peter, L. M. *J. Phys. Chem. B* **2003**, *107*, 7536.

(218) Snaith, H.; Grätzel, M. *Adv. Mater.* **2007**, *19*, 3643.

(219) Tétreault, N.; Horváth, E.; Moehl, T.; Brillet, J.; Smajda, R.; Bungener, S.; Cai, N.; Wang, P.; Zakeeruddin, S. M.; Forró, L.; Magrez, A.; Grätzel, M. *ACS Nano* **2010**, *4*, 7644.

(220) Huang, F.; Chen, D.; Zhang, X. L.; Caruso, R. A.; Cheng, Y.-B. *Adv. Funct. Mater.* **2010**, *20*, 1301.

(221) Kim, Y. J.; Lee, M. H.; Kim, H. J.; Lim, G.; Choi, Y. S.; Park, N. G.; Kim, K.; Lee, W. I. *Adv. Mater.* **2009**, *21*, 3668.

(222) Chen, D.; Huang, F.; Cheng, Y.-B.; Caruso, R. A. *Adv. Mater.* **2009**, *21*, 2206.

(223) Sauvage, F.; Chen, D. H.; Comte, P.; Huang, F. Z.; Heiniger, L. P.; Cheng, Y. B.; Caruso, R. A.; Grätzel, M. *ACS Nano* **2010**, *4*, 4420.

(224) Liao, J.-Y.; Lei, B.-X.; Kuang, D.-B.; Su, C.-Y. *Energy Environ. Sci.* **2011**, *4*, 4079.

(225) Chen, Y.; Huang, F.; Chen, D.; Cao, L.; Zhang, X. L.; Caruso, R. A.; Cheng, Y.-B. *ChemSusChem* **2011**, *4*, 1498.

(226) Lan, C.-M.; Liu, S.-E.; Shiu, J.-W.; Hu, J.-Y.; Lin, M.-H.; Diau, E. W.-G. *RSC Adv.* **2013**, *3*, 559.

(227) Hwang, D.-K.; Lee, B.; Kim, D.-H. *RSC Adv* **2013**, *3*, 3017.

(228) Kim, J.; Koh, J. K.; Kim, B.; Kim, J. H.; Kim, E. *Angew. Chem., Int. Ed.* **2012**, *51*, 6864.

(229) Memarian, N.; Concina, I.; Braga, A.; Rozati, S. M.; Vomiero, A.; Quintana, M.; Edvinsson, T.; Hagfeldt, A.; Boschloo, G. *J. Phys. Chem. C* **2007**, *111*, 1035.

(230) Zhang, Q.; Dandeneau, C. S.; Zhou, X.; Cao, G. *Adv. Mater.* **2009**, *21*, 4087.

(231) Memarian, N.; Concina, I.; Braga, A.; Rozati, S. M.; Vomiero, A.; Sberveglieri, G. *Angew. Chem., Int. Ed.* **2011**, *50*, 12321.

(232) Anta, J. A.; Guillén, E.; Tena-Zaera, R. *J. Phys. Chem. C* **2012**, *116*, 11413.

(233) Green, A. N. M.; Palomares, E.; Haque, S. A.; Kroon, J. M.; Durrant, J. R. *J. Phys. Chem. B* **2005**, *109*, 12525.

(234) Tétreault, N.; Arsenault, É.; Heiniger, L.-P.; Soheilnia, N.; Brillet, J.; Moehl, T.; Zakeeruddin, S.; Ozin, G. A.; Grätzel, M. *Nano Lett.* **2011**, *11*, 4579.

(235) Peumans, P.; Yakimov, A.; Forrest, S. R. *J. Appl. Phys.* **2003**, *93*, 3693.

(236) Brabec, C. J.; Cravino, A.; Meissner, D.; Sariciftci, N. S.; Fromherz, T.; Rispens, M. T.; Sanchez, L.; Hummelen, J. C. *Adv. Funct. Mater.* **2001**, *11*, 374.

(237) Bouclé, J.; Ravirajan, P.; Nelson, J. *J. Mater. Chem.* **2007**, *17*, 3141.

(238) Hochbaum, A. I.; Yang, P. *Chem. Rev.* **2010**, *110*, 527.

(239) Xu, T.; Qiao, Q. *Energy Environ. Sci.* **2011**, *4*, 2700.

(240) Zhou, Y.; Eck, M.; Krüger, M. *Energy Environ. Sci* **2010**, *3*, 1851.

(241) Li, S.-S.; Chen, C.-W. *J. Mater. Chem. A* **2013**, *1*, 10574.

(242) Arango, A. C.; Carter, S. A.; Brock, P. J. *Appl. Phys. Lett.* **1999**, *74*, 1698.

(243) Coakley, K. M.; McGehee, M. D. *Appl. Phys. Lett.* **2003**, *83*, 3380.

(244) Zhu, R.; Jiang, C.-Y.; Liu, B.; Ramakrishna, S. *Adv. Mater.* **2009**, *21*, 994.

(245) Abrusci, A.; Ding, I.-K.; Al-Hashimi, M.; Segal-Peretz, T.; McGehee, M. D.; Heeney, M.; Frey, G. L.; Snaith, H. J. *Energy Environ. Sci.* **2011**, *4*, 3051.

(246) Yu, J.; Shen, T.-L.; Weng, W.-H.; Huang, Y.-C.; Huang, C.-I.; Su, W.-F.; Rwei, S.-P.; Ho, K.-C.; Wang, L. *Adv. Energy Mater.* **2012**, *2*, 245.

(247) Canesi, E. V.; Binda, M.; Abate, A.; Guarnera, S.; Moretti, L.; D'Innocenzo, V.; Kumar, R. S. S.; Bertarelli, C.; Abrusci, A.; Snaith, H.; Calloni, A.; Brambilla, A.; Ciccacci, F.; Aghion, S.; Moia, F.; Ferragut, R.; Melis, C.; Malloci, G.; Mattoni, A.; Lanzania, G.; Petrozza, A. *Energy Environ. Sci.* **2012**, *5*, 9068.

(248) Ishii, A.; Miyasaka, T. *Chem. Commun.* **2012**, *48*, 9900.

(249) Liu, Y.; Scully, S. R.; McGehee, M. D.; Liu, J.; Luscombe, C. K.; Fréchet, J. M. J.; Shaheen, S. E.; Ginley, D. S. *J. Phys. Chem. B* **2006**, *110*, 3257.

(250) Goh, C.; Scully, S. R.; McGehee, M. D. *J. Appl. Phys.* **2007**, *101*, 114503.

(251) Bouclé, J.; Chyla, S.; Shaffer, M. S. P.; Durrant, J. R.; Bradley, D. D. C.; Nelson, J. *Adv. Funct. Mater.* **2008**, *18*, 622.

(252) Lin, Y.-Y.; Chu, T.-H.; Chen, C.-W; Su, W.-F. *Appl. Phys. Lett.* **2008**, *92*, 053312.

(253) Lin, Y.-Y; Chu, T.-H.; Li, S.-S.; Chuang, C.-H.; Chang, C.-H.; Su, W.-F.; Chang, C.-P.; Chu, M.-W.; Chen, C.-W. *J. Am. Chem. Soc.* **2009**, *131*, 3644.

(254) Lin, J.-F; Tu, G.-Y.; Ho, C.-C.; Chang, C.-Y.; Yen, W.-C.; Hsu, S.-H.; Chen, Y.-F.; Su, W.-F. *ACS Appl. Mater. Interfaces* **2013**, *5*, 1009.

(255) Kwong, C. Y.; Djurišić, A. B.; Chui, P. C.; Chen, K. W.; Chan, W. K. *Chem. Phys. Lett.* **2004**, *384*, 372.

(256) Chuang, C.-H.; Lin, Y.-Y.; Tseng, Y.-H.; Chu, T.-H.; Lin, C.-C.; Su, W.-F.; Chen, C.-W. *J. Phys. Chem. C* **2010**, *114*, 18717.

(257) Li, S.-S.; Chang, C.-P.; Lin, C.-C.; Lin, Y.-Y.; Chang, C.-H.; Yang, J.-R.; Chu, M.-W.; Chen, C.-W. *J. Am. Chem. Soc.* **2011**, *133*, 11614.

(258) Lin, C.-C.; Ho, P.-H.; Huang, C.-L.; Du, C.-H.; Yu, C.-C.; Chen, H.-L.; Yeh, Y.-C.; Li, S.-S.; Lee, C.-K.; Pao, C.-W.; Chang, C.-P.; Chu, M.-W.; Chen, C.-W. *J. Phys. Chem. C* **2012**, *116*, 25081.

(259) Lee, C.-K.; Pao, C.-W.; Chen, C.-W. *Energy Environ. Sci.* **2013**, *6*, 307.

(260) Kuo, C. Y.; Tang, W. C.; Gau, C.; Guo, T. F.; Jeng, D. Z. *Appl. Phys. Lett.* **2008**, *93*, 033307.

(261) Hsu, S.-C.; Liao, W.-P.; Lin, W.-H.; Wu, J.-J. *J. Phys. Chem. C* **2012**, *116*, 25721.

(262) Liao, W.-P.; Hsu, S.-C.; Lin, W.-H.; Wu, J.-J. *J. Phys. Chem. C* **2012**, *116*, 15938.

(263) Mor, G. K.; Kim, S.; Paulose, M.; Varghese, O. K.; Shankar, K.; Basham, J.; Grimes, C. A. *Nano Lett.* **2009**, *9*, 4250.

(264) Mor, G. K; Shankar, K.; Paulose, M.; Varghese, O. K.; Grimes, C. A. *Appl. Phys. Lett.* **2007**, *91*, 152111.

(265) Shankar, K.; Mor, G. K.; Prakasam, H. E.; Varghese, O. K.; Grimes, C. A. *Langmuir* **2007**, *23*, 12445.

(266) Baker, D. R.; Kamat, P. V. *Adv. Funct. Mater.* **2009**, *19*, 805.

(267) Sun, W.-T.; Yu, Y.; Pan, H.-Y.; Gao, X.-F.; Chen, Q.; Peng, L.-M. *J. Am. Chem. Soc.* **2008**, *130*, 1124.

(268) Robel, I.; Subramanian, V.; Kuno, M.; Kamat, P. V. *J. Am. Chem. Soc.* **2006**, *128*, 2385.

(269) Kongkanand, A.; Tvrdy, K.; Takechi, K.; Kuno, M.; Kamat, P. V. *J. Am. Chem. Soc.* **2008**, *130*, 4007.

(270) Yang, H.; Fan, W.; Vaneski, A.; Susha, A. S.; Teoh, W. Y.; Rogach, A. L. *Adv. Funct. Mater.* **2012**, *22*, 2821.

(271) Gónzalez-Pedro, V.; Xu, X.; Mora-Seró, I.; Bisquert, J. *ACS Nano* **2010**, *4*, 5783.

(272) Zhang, H.; Cheng, K.; Hou, Y. M.; Fang, Z.; Pan, Z. X.; Wu, W. J.; Hua, J. L.; Zhong, X. H. *Chem. Commun.* **2012**, *48*, 11235.

(273) Santra, P. K.; Kamat, P. V. *J. Am. Chem. Soc.* **2012**, *134*, 2508.

(274) Plass, R.; Pelet, S.; Krueger, J.; Grätzel, M.; Bach, U. *J. Phys. Chem. B* **2002**, *106*, 7578.

(275) Lee, H.; Leventis, H. C.; Moon, S.-J.; Peter, C.; Ito, S.; Haque, S. A.; Torres, T.; Nüesch, F.; Geiger, T.; Zakeeruddin, S. M.; Grätzel, M.; Nazeeruddin, M. K. *Adv. Funct. Mater.* **2009**, *19*, 2735.

(276) Hyun, B.-R.; Zhong, Y.-W.; Bartnik, A. C.; Sun, L.; Abruña, H. D.; Wise, F. W.; Goodreau, J. D.; Matthews, J. R.; Leslie, T. M.; Borrelli, N. F. *ACS Nano* **2008**, *2*, 2206.

(277) Braga, A.; Giménez, S.; Concina, I.; Vomiero, A.; Mora-Seró, I. *J. Phys. Chem. Lett.* **2011**, *2*, 454.

(278) Zhou, N.; Chen, G.; Zhang, X.; Cheng, L.; Luo, Y.; Li, D.; Meng, Q. *Electrochem. Commun.* **2012**, *20*, 97.

(279) González-Pedro, V.; Sima, C.; Marzari, G.; Boix, P. P.; Giménez, S.; Shen, Q.; Dittrich, T.; Mora-Seró, I. *Phys. Chem. Chem. Phys.* **2013**, *15*, 13835.

(280) Vogel, R.; Hoyer, P.; Weller, H. *J. Phys. Chem.* **1994**, *98*, 3183.

(281) Peter, L. M.; Wijayantha, K. G. U.; Riley, D. J.; Waggett, J. P. *J. Phys. Chem. B* **2003**, *107*, 8378.

(282) Zaban, A.; Mićić, O. I.; Gregg, B. A.; Nozik, A. J. *Langmuir* **1998**, *14*, 3153.

(283) Rühle, S.; Shalom, M.; Zaban, A. *ChemPhysChem* **2010**, *11*, 2290.

(284) Mora-Seró, I.; Bisquert, J. *J. Phys. Chem. Lett.* **2010**, *1*, 3046.

(285) Hetsch, F.; Xu, X.; Wang, H.; Kershaw, S. V.; Rogach, A. L. *J. Phys. Chem. Lett.* **2011**, *2*, 1879.

(286) Toyoda, T.; Shen, Q. *J. Phys. Chem. Lett.* **2012**, *3*, 1885.

(287) Kamat, P. V. *J. Phys. Chem. C* **2008**, *112*, 18737.

(288) Hod, I.; González-Pedro, V.; Tachan, Z.; Fabregat-Santiago, F.; Mora-Seró, I.; Bisquert, J.; Zaban, A. *J. Phys. Chem. Lett.* **2011**, *2*, 3032.

(289) Jin, H.; Choi, S.; Lee, H. J.; Kim, S. *J. Phys. Chem. Lett.* **2013**, *4*, 2461.

(290) Kamat, P. V. *J. Phys. Chem. Lett.* **2013**, *4*, 908.

(291) Hodes, G. *J. Phys. Chem. C* **2008**, *112*, 17778.

(292) Guijarro, N.; Campiña, J. M.; Shen, Q.; Toyoda, T.; Lana-Villarreal, T.; Gómez, R. *Phys. Chem. Chem. Phys.* **2011**, *13*, 12024.

(293) Vogel, R.; Pohl, K.; Weller, H. *Chem. Phys. Lett.* **1990**, *174*, 241.

(294) Gopidas, K. R.; Bohorquez, M.; Kamat, P. V. *J. Phys. Chem.* **1990**, *94*, 6435.

(295) Niitsoo, O.; Sarkar, S. K.; Pejoux, C.; Rühle, S.; Cahen, D.; Hodes, G. *J. Photochem Photobiol. A* **2006**, *181*, 306.

(296) Lee, H.; Wang, M.; Chen, P.; Gamelin, D. R.; Zakeeruddin, S. M.; Grätzel, M.; Nazeeruddin, M. K. *Nano Lett.* **2009**, *9*, 4221.

(297) Giménez, S.; Xu, X.; Lana-Villarreal, T.; Gómez, R.; Agouram, S.; Muñoz-Sanjosé, V.; Mora-Seró, I. *J. Appl. Phys.* **2010**, *108*, 064310.

(298) Robel, I.; Subramanian, V.; Kuno, M.; Kamat, P. V. *J. Am. Chem. Soc.* **2006**, *128*, 2385.

(299) Watson, D. F. *J. Phys. Chem. Lett.* **2010**, *1*, 2299.

(300) Guijarro, N.; Lana-Villarreal, T.; Mora-Seró, I.; Bisquert, J.; Gómez, R. *J. Phys. Chem. C* **2009**, *113*, 4208.

(301) Pan, Z.; Zhang, H.; Cheng, K.; Hou, Y.; Hua, J.; Zhong, X. *ACS Nano* **2012**, *6*, 3982.

(302) Pan, Z.; Zhao, K.; Wang, J.; Zhang, H.; Feng, Y.; Zhong, X. *ACS Nano* **2013**, *7*, 5215.

(303) Wang, J.; Mora-Sero, I.; Pan, Z.; Zhao, K.; Zhang, H.; Feng, Y.; Yang, G.; Zhong, X.; Bisquert, J. *J. Am. Chem. Soc.* **2013**, *135*, 15913.

(304) Boix, P. P.; Larramona, G.; Jacob, A.; Delatouche, B.; Mora-Seró, I.; Bisquert, J. *J. Phys. Chem. C* **2012**, *116*, 1579.

(305) Mora-Seró, I.; Giménez, S.; Fabregat-Santiago, F.; Gómez, R.; Shen, Q.; Toyoda, T.; Bisquert, J. *Acc. Chem. Res.* **2009**, *42*, 1848.

(306) Yu, K.; Lin, X.; Lu, G.; Wen, Z.; Yuan, C.; Chen, J. *RSC Adv.* **2012**, *2*, 7843.

(307) Shalom, M.; Dor, S.; Rühle, S.; Grinis, L.; Zaban, A. *J. Phys. Chem. C* **2009**, *113*, 3895.

(308) Barea, E. M.; Shalom, M.; Giménez, S.; Hod, I.; Mora-Seró, I.; Zaban, A.; Bisquert, J. *J. Am. Chem. Soc.* **2010**, *132*, 6834.

(309) Shen, Q.; Kobayashi, J.; Diguna, L. J.; Toyoda, T. *J. Appl. Phys.* **2008**, *103*, 084304.

(310) Giménez, S.; Mora-Seró, I.; Macor, L.; Guijarro, N.; Lana-Villarreal, T.; Gómez, R.; Diguna, L. J.; Shen, Q.; Toyoda, T.; Bisquert, J. *Nanotechnology* **2009**, *20*, 295204.

(311) Tachan, Z.; Hod, I.; Shalom, M.; Grinis, L.; Zaban, A. *Phys. Chem. Chem. Phys.* **2013**, *15*, 3841.

(312) Liu, Z.; Miyauchi, M.; Uemura, Y.; Cui, Y.; Hara, K. *Appl. Phys. Lett.* **2010**, *96*, 233107.

(313) Shalom, M.; Albero, J.; Tachan, Z.; Martínez-Ferrero, E.; Zaban, A.; Palomares, E. *J. Phys. Chem. Lett.* **2010**, *1*, 1134.

(314) Shalom, M.; Rühle, S.; Hod, I.; Yahav, S.; Zaban, A. *J. Am. Chem. Soc.* **2009**, *131*, 9876.

(315) Chi, C.-F.; Chen, P.; Lee, Y.-L.; Liu, I.-P.; Chou, S.-C.; Zhang, X.-L.; Bach, U. *J. Mater. Chem.* **2011**, *21*, 17534.

(316) Gao, X.-F.; Li, H.-B.; Sun, W.-T.; Chen, Q.; Tang, F.-Q.; Peng, L.-M. *J. Phys. Chem. C* **2009**, *113*, 7531.

(317) Bang, J. H.; Kamat, P. V. *Adv. Funct. Mater.* **2010**, *20*, 1970.

(318) Chen, L.-Y; Yang, Z.; Chen, C.-Y; Ho, T.-Y; Liu, P.-W.; Chang, H.-T. *Nanoscale* **2011**, *3*, 4940.

(319) Dong, C.; Li, X.; Qi, J. *J. Phys. Chem. C* **2011**, *115*, 20307.

(320) Samadpour, M.; Giménez, S.; Zad, A. I.; Taghavinia, N.; Mora-Seró, I. *Phys. Chem. Chem. Phys.* **2012**, *14*, 522.

(321) Sudhagar, P.; González-Pedro, V.; Mora-Seró, I.; Fabregat-Santiago, F.; Bisquert, J.; Kang, Y. S. *J. Mater. Chem.* **2012**, *22*, 14228.

(322) Ai, G.; Sun, W.; Gao, X.; Zhang, Y.; Peng, L. *J. Mater. Chem.* **2011**, *21*, 8749.

(323) Hensel, J.; Wang, G. M.; Li, Y.; Zhang, J. Z. *Nano Lett.* **2010**, *10*, 478.

(324) Diguna, L. J.; Shen, Q.; Sato, A.; Katayama, K.; Sawada, T.; Toyoda, T. *Mater. Sci. Eng. C* **2007**, *27*, 1514.

(325) Diguna, L. J.; Shen, Q.; Kobayashi, J.; Toyoda, T. *Appl. Phys. Lett.* **2007**, *91*, 023116.

(326) Harakeh, M. E.; Halaoui, L. *J. Phys. Chem. C* **2010**, *114*, 2806.

(327) Samadpour, M.; Giménez, S.; Boix, P. P.; Shen, Q.; Calvo, M. E.; Taghavinia, N.; zad, A. I.; Toyoda, T.; Míguez, H.; Mora-Seró, I. *Electrochim. Acta* **2012**, *75*, 139.

(328) Kaiser, I.; Ernst, K.; Fischer, C.-H.; Könenkamp, R.; Rost, C.; Sieber, I.; Lux-Steiner, M. C. *Sol. Energy Mater. Sol. Cells* **2001**, *67*, 89.

(329) Nanu, M.; Schoonman, J.; Goossens, A. *Adv. Mater.* **2004**, *16*, 453.

(330) Nanu, M.; Schoonman, J.; Goossens, A. *Adv. Funct. Mater.* **2005**, *15*, 95.

(331) Nanu, M.; Schoonman, J.; Goossens, A. *Nano Lett.* **2005**, *5*, 1716.

(332) O'Hayre, R.; Nanu, M.; Schoonman, J.; Goossens, A.; Wang, Q.; Grätzel, M. *Adv. Funct. Mater.* **2006**, *16*, 1566.

(333) O'Hayre, R.; Nanu, M.; Schoonman, J.; Goossens, A. *Nanotechnology* **2007**, *18*, 055702.

(334) Goossens, A.; Hofhuis, J. *Nanotechnology* **2008**, *19*, 424018.

(335) Lenzmann, F.; Nanu, M.; Kijatkina, O.; Belaidi, A. *Thin Solid Films* **2004**, *451*, 639.

(336) Seabold, J. A.; Shankar, K.; Wilke, R. H. T.; Paulose, M.; Varghese, O. K.; Grimes, C. A.; Choi, K.-S. *Chem. Mater.* **2008**, *20*, 5266.

(337) Zou, Y.; Li, D.; Sheng, X.; Wang, L.; Yang, D. *Solar Energy* **2012**, *86*, 1359.

(338) Brus, V. V.; Ilashchuk, M. I.; Kovalyuk, Z. D.; Maryanchuk, P. D. *Semicond. Sci. Technol.* **2012**, *27*, 055008.

(339) Nezu, S.; Larramona, G.; Chon, C.; Jacob, A.; Delatouche, B.; Péré, D.; Moisan, C. *J. Phys. Chem. C* **2010**, *114*, 6854.

(340) Itzhaik, Y.; Niitsoo, O.; Page, M.; Hodes, G. *J. Phys. Chem. C* **2009**, *113*, 4254.

(341) Tsujimoto, K.; Nguyen, D.; Ito, S.; Nishino, H.; Matsuyoshi, H.; Konno, A.; Kumara, G. R. A.; Tennakone, K. *J. Phys. Chem. C* **2012**, *116*, 13465.

(342) Im, S. H.; Lim, C.-S.; Chang, J. A.; Lee, Y. H.; Maiti, N.; Kim, H.-J.; Nazeeruddin, M. K.; Grätzel, M.; Seok, S. I. *Nano Lett.* **2011**, *11*, 4789.

(343) Boix, P. P.; Lee, Y. H.; Fabregat-Santiago, F.; Im, S. H.; Mora-Seró, I.; Bisquert, J.; Seok, S. I. *ACS Nano* **2012**, *6*, 873.

(344) Chang, J. A.; Im, S. H.; Lee, Y. H.; Kim, H.-j.; Lim, C.-S.; Heo, J. H.; Seok, S. I. *Nano Lett.* **2012**, *12*, 1863.

(345) Park, N.-G. *J. Phys. Chem. Lett.* **2013**, *4*, 2423.

(346) Snaith, H. J. *J. Phys. Chem. Lett.* **2013**, *4*, 3623.

(347) Rhee, J. H.; Chung, C.-C.; Diau, E. W.-G. *NPG Asia Mater.* **2013**, *5*, e68.

(348) Mosconi, E.; Amat, A.; Nazeeruddin, M. K.; Grätzel, M.; De Angelis, F. *J. Phys. Chem. C* **2013**, *117*, 13902.

(349) Kumar, M. H.; Yantara, N.; Dharani, S.; Grätzel, M.; Mhaisalkar, S.; Boix, P. P.; Mathews, N. *Chem. Commun.* **2013**, *49*, 11089.

(350) Xing, G.; Mathews, N.; Sun, S.; Lim, S. S.; Lam, Y. M.; Grätzel, M.; Mhaisalkar, S.; Sum, T. C. *Science* **2013**, *342*, 344.

(351) Cai, B.; Xing, Y.; Yang, Z.; Zhang, W.; Qiu, J. *Energy Environ. Sci.* **2013**, *6*, 1480.

(352) Bi, D.; Yang, L.; Boschloo, G.; Hagfeldt, A.; Johansson, E. M. J. *J. Phys. Chem. Lett.* **2013**, *4*, 1532.

(353) Jeng, J.-Y.; Chiang, Y.-F.; Lee, M.-H.; Peng, S.-R.; Guo, T.-F.; Chen, P.; Wen, T.-C. *Adv. Mater.* **2013**, *25*, 3727.

(354) Sun, S.; Salim, T.; Mathews, N.; Duchamp, M.; Boothroyd, C.; Xing, G.; Sum, T. C.; Lam, Y. M. *Energy Environ. Sci.* **2014**, *7*, 399.

(355) Ball, J. M.; Lee, M. M.; Hey, A.; Snaith, H. J. *Energy Environ. Sci.* **2013**, *6*, 1739.

(356) Liu, M.; Johnston, M. B.; Snaith, H. J. *Nature* **2013**, *501*, 395.

(357) Kojima, A.; Teshima, K.; Shirai, Y.; Miyasaka, T. *J. Am. Chem. Soc.* **2009**, *131*, 6050.

(358) Im, J.; Lee, C.; Lee, J.; Park, S.; Park, N. *Nanoscale* **2011**, *3*, 4088.

(359) Kim, H.; Lee, C.; Im, J.; Lee, K.; Moehl, T.; Marchioro, A.; Moon, S.; Humphry-Baker, R.; Yum, J.; Moser, J. E.; Grätzel, M.; Park, N. *Sci. Rep.* **2012**, *2*, 591.

(360) Lee, M. M.; Teuscher, J.; Miyasaka, T.; Murakami, T. N.; Snaith, H. J. *Science* **2012**, *338*, 643.

(361) Kim, H.-S.; Mora-Sero, I.; Gonzalez-Pedro, V.; Fabregat-Santiago, F.; Juarez-Perez, E. J.; Park, N.-G.; Bisquert, J. *Nat. Commun.* **2013**, *4*, 2242.

(362) Abrusci, A.; Stranks, S. D.; Docampo, P.; Yip, H.-L.; Jen, A. K.-Y.; Snaith, H. J. *Nano Lett.* **2013**, *13*, 3124.

(363) Etgar, L.; Gao, P.; Xue, Z.; Peng, Q.; Chandiran, A. K.; Liu, B.; Nazeeruddin, M. K.; Grätzel, M. *J. Am. Chem. Soc.* **2012**, *134*, 17396.

(364) Heo, J. H.; Im, S. H.; Noh, J. H.; Mandal, T. N.; Lim, C.; Chang, J. A.; Lee, Y. H.; Kim, H.; Sarkar, A.; Nazeeruddin, M. K.; Grätzel, M.; Seok, S. I. *Nat. Photon.* **2013**, *7*, 486.

(365) Burschka, J.; Pellet, N.; Moon, S.; Humphry-Baker, R.; Gao, P.; Nazeeruddin, M. K.; Grätzel, M. *Nature* **2013**, *499*, 316.

(366) Stranks, S. D.; Eperon, G. E.; Grancini, G.; Menelaou, C.; Alcocer, M. J. P.; Leijtens, T.; Herz, L. M.; Petrozza, A.; Snaith, H. J. *Science* **2013**, *342*, 341.

(367) Zhang, W.; Saliba, M.; Stranks, S. D.; Sun, Y.; Shi, X.; Wiesner, U.; Snaith, H. J. *Nano Lett.* **2013**, *13*, 4505.

(368) Noh, J. H.; Jeon, N. J.; Choi, Y. C.; Nazeeruddin, M. K.; Grätzel, M.; Seok, S. I. *J. Mater. Chem. A* **2013**, *1*, 11842.